# Dissertation

submitted to the

Combined Faculty of Natural Sciences and Mathematics
of Heidelberg University, Germany

for the degree of

Doctor of Natural Sciences


Put forward by

**Annika Tebben**

born in Cloppenburg, Germany



Oral examination: 22.10.2021

# Rydberg Electromagnetically Induced Transparency

—

**A vanishing linear response, resonances, and a stationary Rydberg polariton**

**Referees:** **Prof. Dr. Matthias Weidemüller**
**apl. Prof. Dr. Jörg Evers**

**Abstract** Rydberg electromagnetically induced transparency (Rydberg EIT) enables extremely strong optical nonlinearities, opening the possibility for photon-photon interactions and exotic states of light. Subjects of this thesis are the development and the experimental test of semiclassical models for Rydberg EIT systems on two-photon resonance. Beyond that, this thesis opens the route towards enhanced photon-photon interactions in terms of an increased interaction time. Three major results are achieved: (i) In the semiclassical regime, we extend existing models and reveal that a two-body, two-photon resonance leads to an enhanced nonlinear optical response. (ii) We develop an experimental method to rigorously test semiclassical models of Rydberg EIT. For this purpose, we go beyond previous experimental investigations and measure transmission spectra on two-photon resonance, where the linear response of the system vanishes. We identify qualitative differences between a measured absorption feature and predictions provided by a mean-field model, a Monte-Carlo rate equation simulation, and a theory based on a pairwise treatment of atomic interactions. (iii) In the quantum regime, we propose and analyze a novel scheme to endow a stationary light polariton with a Rydberg character, resulting in a stationary Rydberg polariton. Our scheme offers the prospect for polariton interactions with increased interaction time, and thus might find application in the creation of exotic states of light.

**Zusammenfassung** Elektromagnetisch induzierte Transparenz mit Rydbergatomen (Rydberg EIT) ermöglicht extrem starke optische Nichtlinearitäten, welche die Möglichkeit für Photonen-Photonen Wechselwirkungen und exotische Zustände von Licht eröffnen. Themen der vorliegenden Arbeit sind die Entwicklung und die experimentelle Überprüfung von semiklassischen Modellen für Rydberg EIT Systeme auf Zwei-Photonen-Resonanz. Darüber hinaus ebnet diese Arbeit den Weg für verstärkte Photonen-Photonen Wechselwirkungen mittels einer verlängerten Wechselwirkungszeit. Drei wesentliche Ergebnisse werden erzielt: (i) Im semiklassischen Regime erweitern wir bestehende Modelle und zeigen, dass eine Zwei-Körper, Zwei-Photonen-Resonanz zu einer verstärkten nichtlinearen optische Antwort führt. (ii) Wir entwickeln eine experimentelle Methode für die rigorose Überprüfung semiklassischer Modelle der Rydberg EIT. Hierfür gehen wir über vorherige experimentelle Studien hinaus und messen Transmissionsspektren auf Zwei-Photonen-Resonanz, wo die lineare Antwort des Systems verschwindet. Wir identifizieren qualitative Abweichungen zwischen gemessenen Absorptionseigenschaften und Vorhersagen von einer Molekularfeldtheorie, einer Monte-Carlo Ratengleichungssimulation und einer Theorie, die auf einer paarweisen Behandlung von atomaren Wechselwirkungen beruht. (iii) Im quantenmechanischen Regime schlagen wir ein neues Schema vor, mit welchem ein stationäres Licht-Polariton mit einem Rydberg-Charakter ausgestattet wird, und analysieren dieses. Als Ergebnis erhalten wir ein stationäres Rydberg-Polariton. Unser Schema bietet die Aussicht auf Polaritonen-Wechselwirkungen mit einer verlängerten Wechselwirkungszeit und könnte daher Anwendung in der Erzeugung von exotischen Zuständen von Licht finden.

# List of publications

This thesis is based on the following manuscript and publications:

- **Blockade-induced resonant enhancement of the optical nonlinearity in a Rydberg medium**
  A. Tebben, C. Hainaut, V. Walther, Y.-C. Zhang, G. Zürn, T. Pohl and M. Weidemüller, Phys. Rev. A **100**, 063812 (2019)
- **Nonlinear absorption in interacting Rydberg electromagnetically-induced-transparency spectra on two-photon resonance**
  A. Tebben, C. Hainaut, A. Salzinger, S. Geier, T. Franz, T. Pohl, M. Gärttner, G. Zürn and M. Weidemüller, Phys. Rev. A **103**, 063710 (2021)
- **A stationary Rydberg polariton**
  A. Tebben, C. Hainaut, A. Salzinger, T. Franz, S. Geier, G. Zürn and M. Weidemüller, arXiv: 2108.00657 (2021)

The author furthermore contributed to the following manuscripts:

- **Floquet Hamiltonian Engineering of an Isolated Many-Body Spin System**
  S. Geier, N. Thaicharoen, C. Hainaut, T. Franz, A. Salzinger, A. Tebben, D. Grimshandl, G. Zürn and M. Weidemüller, arXiv:2105.01597 (2021)
- **Glassy quantum dynamics of disordered Ising spins**
  P. Schultzen, T. Franz, S. Geier, A. Salzinger, A. Tebben, C. Hainaut, G. Zürn, M. Weidemüller and M. Gärttner, arXiv:2104.00349 (2021)
- **Semiclassical simulations predict glassy dynamics for disordered Heisenberg models**
  P. Schultzen, T. Franz, C. Hainaut, S. Geier, A. Salzinger, A. Tebben, G. Zürn, M. Gärttner and M. Weidemüller, arXiv:2107.13314 (2021)
- **Microwave-engineering of programmable XXZ Hamiltonians in arrays of Rydberg atoms**
  P. Scholl, H. J. Williams, G. Bornet, F. Wallner, D. Barredo, T. Lahaye and A. Browaeys – L. Henriet and A. Signoles – C. Hainaut, T. Franz, S. Geier, A. Tebben, A. Salzinger, G. Zürn and M. Weidemüller, arXiv:2107.14459 (2021)

Parts of this thesis have been published in the following articles.

Adapted with permission from:
A. Tebben, C. Hainaut, V. Walther, Y.-C. Zhang, G. Zürn, T. Pohl and M. Weidemüller,
*Blockade-induced resonant enhancement of the optical nonlinearity in a Rydberg medium*
Phys. Rev. A **100**, 063812 (2019)
DOI: 10.1103/PhysRevA.100.063812,


Adapted with permission from:
A. Tebben, C. Hainaut, A. Salzinger, S. Geier, T. Franz, T. Pohl, M. Gärttner, G. Zürn and M. Weidemüller,
*Nonlinear absorption in interacting Rydberg electromagnetically-induced-transparency spectra on two-photon resonance*
Phys. Rev. A **103**, 063710 (2021)
DOI: 10.1103/PhysRevA.103.063710,


Parts of this thesis appear in the following manuscript.

A. Tebben, C. Hainaut, A. Salzinger, T. Franz, S. Geier, G. Zürn and M. Weidemüller,
*A stationary Rydberg polariton*
arXiv:2108.00657 [quant-ph] (2021)

# Contents

CHAPTER 1

# Introduction

Light is of fundamental importance for our everyday life, and understanding as well as controlling light laid the base for groundbreaking scientific advances. As a prominent example, the laser [1, 2], a coherent source of light, has become indispensable for our daily communication as well as for medical and industrial applications. Moreover, it has revolutionized the field of atomic physics by enabling sophisticated techniques for optical cooling and trapping of atoms [3]. Today we perceive light not only as an electromagnetic wave described by Maxwell's equations, but at the same time as to be composed of quantum mechanical particles called photons. Despite the linearity of Maxwell's equations in free space, which implies the superposition principle, the question arose whether one could make photons interact [4]. Being a question of fundamental interest by itself, its affirmation opens up entirely new perspectives: for example, exotic states of light, such as photon crystals and fluids [4–6], and all-optical quantum information processing [7–10] become in reach. Therefore, it is not surprising that in the last decades a lot of scientific work has been devoted to achieve photon-photon interactions [4].

By now it is well established that effective photon-photon interactions can be mediated by matter [4]. This possibility arises as the superposition principle is not valid in media that feature a nonlinear optical response to the applied electromagnetic field. If the nonlinearity is sufficiently strong such that the optical response to a single photon is different to that of a pair of photons, effective photon-photon interactions emerge [4]. However, the optical nonlinearity of conventional media is typically very weak due to the small probability of atom-photon scattering [4]. Therefore, it manifests itself only in combination with strong light fields provided by high-intensity lasers. In this case effects such as self-trapping of light [11] and second-order [12] as well as high harmonic generation [13, 14] have been observed.

Strong optical nonlinearities can be generated via strong light-matter coupling induced, for example, by mode confinement in cavities coupled to atoms [15, 16] or quantum dots [17, 18]. Yet another possibility is to transfer strong atomic interactions provided by Rydberg atoms onto light under conditions of electromagnetically induced transparency (EIT) [19, 20], an approach called Rydberg

EIT [21–24].

Within this approach EIT provides an exceptionally coherent form of light-matter coupling. Here, an atomic medium is rendered transparent for a probe field in the presence of a second, strong control field since the system settles into a non-decaying dark-state. The lossless propagation of the probe field under EIT conditions has first been demonstrated in an atomic vapor [20] and can be exploited for enhanced frequency conversion [19]. However, not only the dissipative, but also the dispersive properties of the medium are changed under EIT conditions. As a consequence, light can be slowed down remarkably to group velocities as low as 17 m/s [25]. It even becomes possible to completely stop light inside the medium as an atomic [26–30] or as a stationary photonic excitation [31–45]. On the single-photon level, EIT is associated with the formation of a quasi-particle called dark-state polariton [26, 30]. As it is composed of a photonic excitation and an atomic coherence, the polariton inherits kinetic properties from its light part and dispersion from its matter part.

Strong atomic interactions inherent to Rydberg EIT are introduced by coupling to a highly excited, so-called Rydberg state. These Rydberg atoms [46–49] feature strong and long-range interparticle interactions due to their large polarizability. The high controllability of these interactions makes Rydberg atoms an ideal platform for applications in quantum simulations and technologies [50–52] as well as in information processing [53]. Moreover, a very important consequence of the interactions between Rydberg atoms is the occurrence of the Rydberg blockade effect [54–56]. As a consequence of an interaction-induced level shift, this effect prevents the simultaneous excitation of two atoms into the Rydberg state, if the atoms are closer to each other than a certain distance called the blockade radius.

The Rydberg blockade effect is the key for enabling exceptionally strong optical nonlinearities in Rydberg EIT systems [23, 24]. While one photon experiences EIT transparency, EIT conditions for a second photon are destroyed if it propagates along the first one with a distance smaller than the blockade radius. As a consequence of this nonlinear response, the second photon can experience a drastic attenuation and phase shift [24, 57]. Moreover, due to the long-range character of Rydberg interactions, the associated nonlinearity is highly nonlocal [58, 59]. Rydberg EIT can also be understood in the picture of the EIT dark-state polariton introduced before. Due to their Rydberg component the polaritons, now called Rydberg polaritons [24], inherit the ability to interact with each other while propagating through the atomic medium.

The field of Rydberg EIT has rapidly evolved in the last two decades: In the semiclassical regime, the strong nonlinear attenuation of a classical probe field has been observed [23, 60–65] and applications such as interaction enhanced imaging of Rydberg impurities [66, 67] and microwave electric field sensing [68, 69] have been put forward. In the quantum regime, where the correlation of the light field is strongly affected by the nonlinear response of the Rydberg EIT medium, strong photon-photon interactions, ranging from attractive to repulsive, have been demonstrated [24, 57, 59, 70–73]. Moreover, exotic states of light such as bound states of photons have been observed [57, 71, 72], and precursors of photonic quantum technologies such as all-optical switches [74], transistors [9, 75, 76] and

photonic gates [8, 10] have been demonstrated.

Despite its great success, the field of Rydberg EIT faces two major challenges: First, developing theoretical models is complicated due to correlations emerging from strong interactions in the system. Second, limitations on the achievable interaction strength hinder the efficiency of quantum optics applications of Rydberg EIT. As we address both challenges in this thesis, we will comment on them briefly in the following.

Concerning the first challenge, the semiclassical regime is seemingly simpler to describe than the quantum regime as photon-photon correlations can be discarded [77]. Nevertheless, atomic correlations emerging in a strongly interacting Rydberg gas complicate the development of theoretical models significantly. Exact or numerical calculations are restricted to a small number of atoms [23, 78, 79] as atomic interactions strongly couple the underlying equations of motion. Therefore, approximate models for the nonlinear response of the Rydberg EIT medium have been elaborated, e.g. based on a mean-field assumption [60, 64, 65, 80], Monte-Carlo rate equation simulations [78, 81–83] or low intensity expansions [58, 84]. These models have been shown to explain several aspects of measured Rydberg EIT transmission spectra when the control field is on resonance [23, 60, 62, 64, 65]. However, the occurrence of certain features, including an asymmetry and shift of the spectrum, has been discussed [62, 64]. Therefore, inevitable the two questions

*How to model the strongly interacting and thus strongly correlated light-matter system under Rydberg EIT conditions?*

and

*How to experimentally test these models?*

emerge.

The second challenge of a limited interaction strength arises although the Rydberg EIT nonlinearity outperforms the one of conventional media by orders of magnitude [61]. This is rooted in the fact that both the attenuation and phase shift which a photon can experience over the length of a Rydberg blockade radius are experimentally limited [24, 57, 85, 86]. Approaches to enhance photon-photon interactions in Rydberg EIT settings beyond current schemes included to increase the interaction strength per photon by transferring Rydberg EIT into a cavity setting [87–91], or to increase the interaction time [59, 92–95]. Therefore, also the question

*How to enhance photon-photon interactions?*

is at the heart of current research.

In this thesis we investigate the phenomenon of Rydberg EIT in the semiclassical and quantum regime. Thereby, we address these three questions in the following manner: First, in the semiclassical regime, we develop an intuitive picture that explains an enhanced nonlinear response of the Rydberg EIT medium as resulting from a two-body, two-photon resonance [96]. Second, we develop a method to test this theoretical prediction and other existing models by measuring EIT transmission spectra in the presence of Rydberg interactions. Our approach goes beyond

previous experimental investigations by exploring Rydberg EIT on two-photon resonance, where the linear response of the medium vanishes [97]. Third, in the quantum regime, we propose and analyze a novel scheme that equips a stationary light polariton with a Rydberg character [98]. Due to its stationary nature, the resulting stationary Rydberg polariton holds prospects for enabling enhanced photon-photon interactions due to an increased interaction time.

This thesis is structured as follows:

In *Chapter 2* an introduction to light propagation through an atomic medium from a semiclassical and a quantum mechanical point of view is provided. In the semiclassical regime, the concept of EIT is explained and introduced as a method to control the dissipative and dispersive properties of the medium. Moreover, the emergence of slow and stationary light is discussed. In the quantum regime, the EIT dark-state polariton and the associated slow- and stationary light polaritons are introduced.

In *Chapter 3* the benefits of both EIT and Rydberg physics are combined to arrive at a strong nonlinear optical response of the atomic medium. First, a brief overview on the main characteristics of Rydberg atoms is given. Afterwards, Rydberg EIT is introduced from a semiclassical and quantum mechanical perspective. Finally, we develop our intuitive picture that allows us to considerably deepen our understanding of the enhanced nonlinear optical response of the Rydberg EIT medium in the semiclassical regime.

In *Chapter 4* we experimentally explore Rydberg EIT with classical light fields and compare our findings to theoretical predictions. In particular, we present measurements of EIT transmission spectra with the control beam on resonance and – following our new approach – on two-photon resonance. We compare our experimental results with the predictions of three different theories. Finally, we discuss possible routes towards a better understanding of the observed nonlinear effects from a theoretical and experimental point of view. This chapter is supported by several appendices, covering experimental as well as theoretical details.

In *Chapter 5* we introduce and analyze our scheme for a stationary Rydberg polariton. In order to learn about how interactions influence our scheme, we investigate the system in the presence of a Rydberg impurity. Finally, we consider an experimental realization of the stationary Rydberg polariton and comment on possible applications of our scheme.

In *Chapter 6* we conclude on the presented work in the context of the three questions raised above.

CHAPTER 2

# Basic concepts: From slow to stationary light

Light propagates unaffected through vacuum with the speed of light. However, light-matter interfaces allow to change the propagation of light on a fundamental level, e.g. by absorption and refraction [4]. Moreover, tuning the material properties of light-matter interfaces even enables to actively control the propagation of light. It has been found, that under conditions of electromagnetically induced transparency (EIT) the dissipative and dispersive response of an atomic gas can be strongly altered [19, 20, 99]. With this technique controlling the speed of light inside a medium becomes possible. As a consequence, the group velocity of a light pulse can be remarkably slowed down to 17 m/s [25], leading to the phenomenon of slow light [25, 99, 100].

A light pulse can even be brought to a complete stop inside the medium when laser parameters are dynamically varied. Thereby, the photonic excitation is completely transferred into an atomic excitation [26, 30]. Being able to retrieve the light field after a variable storage time has been demonstrated experimentally with classical light fields [27, 28] and single photons [29]. This lays the ground for quantum memory devices based on stored light [29, 30, 101]. While in this scheme light is stored in the medium as a pure atomic excitation, preserving the photonic character of the light field during the storage process has been enabled by the novel concept of stationary light [31–37].

Controlling the propagation of light by adjusting the optical response of an atomic medium is the precursor for nonlinear optics with Rydberg atoms as addressed within this thesis. Therefore, in this chapter, we discuss the basic concepts of light propagation inside an atomic medium and elaborate how slow and stationary light phenomena emerge. In Sec. 2.1 we approach this topic from a semi-classical perspective and introduce the susceptibility as a measure for the optical response of an atomic gas. We provide the explicit form of the susceptibility for a driven three-level system as obtained from the optical Bloch equations. Moreover, we introduce the effect of EIT as a method to control the dissipative and dispersive properties of the medium, e.g. for the generation of slow and stationary light.

We proceed in Sec. 2.2 with a quantum mechanical view of light propagation in an atomic medium. Here, EIT is associated with the emergence of quasi-particles called dark-state polaritons [26]. They can be slowed down and stopped inside the medium as an atomic excitation. Finally, we introduce the concept of stationary light polaritons, where the photonic component is preserved at zero group velocity [37].

## 2.1 Semiclassical description of light propagation

In this section we present a semiclassical description of light propagation through an atomic medium under EIT conditions. For this purpose, we first introduce the susceptibility as a measure for the optical response of a system in Sec. 2.1.1, and provide the susceptibility of a three-level system, which can be derived from the optical Bloch equations, in Sec. 2.1.2. Afterwards, we explain in Sec. 2.1.3 the phenomenon of EIT from a semiclassical perspective and highlight some details and implications, such as spectral properties and the creation of slow and stationary light. These concepts are relevant for the discussion in subsequent chapters of this thesis.

### 2.1.1 Wave equation and optical response of an atomic gas

The propagation of a classical, scalar light field $E(\mathbf{r},t)$ through an atomic medium is described by the wave equation [102]

$$\left[\frac{1}{c^2}\frac{\partial^2}{\partial t^2}-\nabla^2\right]E(\mathbf{r},t)=-\frac{1}{\epsilon_0 c^2}\frac{\partial^2}{\partial t^2}P(\mathbf{r},t) \tag{2.1}$$

for a dielectric, isotropic medium. Here, $c$ is the speed of light, $\epsilon_0$ is the vacuum permittivity and $P(\mathbf{r},t)$ is the polarization of the atomic medium induced by the light field. The susceptibility $\chi$ relates the polarization to the applied field and fully determines the optical response of the atomic medium. In the simplest case of a linear medium, where the polarization $P(\mathbf{r},t)=\epsilon_0\chi E(\mathbf{r},t)$ [102] is proportional to the applied light field, one obtains from Eq. (2.1) in paraxial approximation [102] and in one dimension the propagation equation [58, 103]

$$\frac{\partial}{\partial z}E_0=\frac{ik_p}{2}\chi E_0 \tag{2.2}$$

for a stationary light field with amplitude $E_0$ and wavevector $k_p$. From Eq. (2.2), it is apparent that the imaginary part of the susceptibility gives rise to a reduction of the field amplitude, while the real part leads to a phase shift [102]. As a consequence, the measurable transmission of the light field, defined by the ratio of incident $I_0\propto|E_0|^2$ and transmitted intensity $I$, can be calculated as [103, 104]

$$T=\frac{I}{I_0}=e^{-k_p\mathrm{Im}(\chi)L}=e^{-\mathrm{OD}}\,. \tag{2.3}$$

Here, we have assumed for simplicity an atomic medium with a constant density over a propagation length $L$. Moreover, the optical depth OD of the medium has been defined.

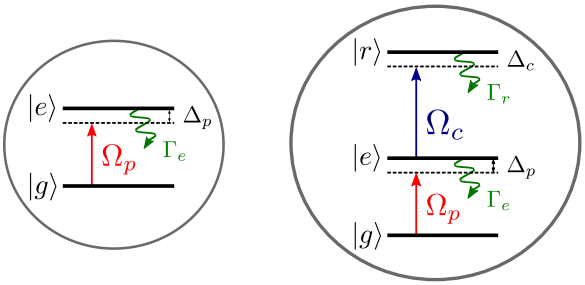


**Figure 2.1: Level schemes for two- and three-level atoms.** A two-level system (left) composed of a ground $|g\rangle$ and excited state $|e\rangle$ with decay rate $\Gamma_e$ interacts with a laser field with Rabi frequency $\Omega_p$ and detuning $\Delta_p$. Adding another laser field with Rabi frequency $\Omega_c$ and detuning $\Delta_c$ completes a ladder-type three-level system (right) with an upper state $|r\rangle$. Within this thesis the upper state is assumed to be long-lived with decay rate $\Gamma_r \ll \Gamma_e$. Level schemes taken and adapted with permission from ref. [96].

The preceding discussion shows that the susceptibility completely describes the propagation of a light field through an atomic medium. Moreover, it becomes apparent that this quantity needs to be derived from optical and atomic properties of the system under consideration. In the following, we discuss that the susceptibility is immediately connected to the quantum state of the atomic system, represented by the density matrix $\hat{\rho}$.

As a simple example, we consider an atomic cloud composed of two-level atoms and exposed to the radiation of a monochromatic light field. The latter couples a ground state $|g\rangle$ to an excited state $|e\rangle$ that decays with rate $\Gamma_e$, as depicted in Fig. 2.1. The macroscopic polarization is related to the dipole moment $\hat{d}$ of the atoms via $P = \rho_0\langle\hat{d}\rangle = \rho_0 \mathrm{Tr}[\hat{\rho}\hat{d}]$ [103] with $\rho_0$ being the atomic density. As a result, one obtains the susceptibility [103–105]

$$\chi_{\mathrm{2lvl}} = \frac{\rho_0\langle\hat{d}\rangle}{\epsilon_0 E_0} = -\frac{2\rho_0|d_{ge}|^2}{\hbar\epsilon_0}\frac{\rho_{eg}}{\Omega_p} = -\chi_0\frac{\Gamma_e}{\Omega_p}\rho_{eg}\,, \tag{2.4}$$

where $\hbar$ denotes the reduced Planck constant. The susceptibility is determined by the dipole matrix element $d_{ge}$ of the ground to excited state transition, the corresponding density matrix element $\rho_{eg}$ and the Rabi frequency

$$\Omega_p = -d_{eg}E_0/\hbar \tag{2.5}$$

of the light field. In order to obtain the third equality of Eq. (2.4), $\chi_0 = \sigma_0\rho_0/k_p$ has been introduced with the atomic absorption cross section $\sigma_0 = 3\lambda_p^2/2\pi$. Here, $\lambda_p = 2\pi/k_p$ is the wavelength of the light field. Furthermore, we have used the relation [104, 105]

$$\Gamma_e = \frac{|d_{ge}|^2 k_p^3}{3\epsilon_0\pi\hbar} \tag{2.6}$$

for the spontaneous decay rate. From Eq. (2.4) we see, that the optical response of the atomic medium is directly connected to the density matrix element $\rho_{eg}$ of

the atomic transition, which is coupled by the light field. However, calculating $\rho_{eg}$ and therefore the optical response of the system is not always as simple and becomes particularly demanding in the presence of atomic interactions as discussed in Chap. 3.

### 2.1.2 Optical Bloch equations for a driven three-level system

Of particular importance for this thesis is the three-level scheme in ladder configuration shown in Fig. 2.1. Here, two light fields, the so-called probe and control fields, couple the transitions between a ground state $|g\rangle$, an intermediate state $|e\rangle$ and an upper state $|r\rangle$. In the following, we provide a brief description of the system in order to arrive at the susceptibility for the driven three-level system. Thereby, we summarize the discussion presented in ref. [103].

In the dipole approximation [105], atom-light interactions are described by the Hamiltonian $\hat{H}_L = -\hat{d}E$. Together with the single-atom Hamiltonian $\hat{H}_0$ the Hamiltonian

$$\hat{H} = \hat{H}_0 + \hat{H}_L \tag{2.7}$$

of the coupled atom-light system in the rotating wave approximation has the form [103, 105]

$$\hat{H} = \frac{\hbar}{2}\begin{pmatrix} 0 & \Omega_p & 0 \\ \Omega_p & -2\Delta_p & \Omega_c \\ 0 & \Omega_c & -2(\Delta_p + \Delta_c) \end{pmatrix} \tag{2.8}$$

in matrix notation and in the basis of the bare atomic states. Here, the coupling is determined by the probe and control field Rabi frequencies $\Omega_p$ and $\Omega_c$, which are detuned from the bare atomic levels by $\Delta_p$ and $\Delta_c$, respectively.

The von Neumann equation [105]

$$\partial_t \hat{\rho} = -\frac{i}{\hbar}\left[\hat{H}, \hat{\rho}\right] \tag{2.9}$$

describes the coherent time evolution of the system with density matrix $\hat{\rho}$. However, typically the system also possesses an incoherent evolution originating from spontaneous population decay and dephasing of the atomic coherences [103, 104, 106]. In our case, spontaneous decay concerns the intermediate and upper states with decay rates $\Gamma_e$ and $\Gamma_r$, respectively. In turn, dephasing of the atomic coherences can, for example, result from laser phase noise, and is characterized by dephasing rates $\gamma_{ge}$, $\gamma_{er}$ and $\gamma_{gr}$ for the three atomic coherences, respectively [107]. Both effects, spontaneous population decay and dephasing of the coherences, can be introduced into the von Neumann equation, Eq. (2.9), in terms of so-called Lindblad operators [108, 109]. For a detailed discussion of these effects and for the corresponding expressions of the Lindblad operators, the reader is referred to e.g. refs. [103, 107–109].

From Eq. (2.9) including such Lindblad operators, the time dynamics of the density matrix elements $\rho_{\alpha\beta} = \langle\alpha|\,\hat{\rho}\,|\beta\rangle$ with $\alpha, \beta \in \{g, e, r\}$ is obtained in form of

the single-body optical Bloch equations (OBE) [62, 81, 110]

$$\partial_t \rho_{gg} = -\Omega_p \mathrm{Im}[\rho_{ge}] + \Gamma_e \rho_{ee} \,, \tag{2.10a}$$
$$\partial_t \rho_{ee} = \Omega_p \mathrm{Im}[\rho_{ge}] - \Omega_c \mathrm{Im}[\rho_{er}] - \Gamma_e \rho_{ee} + \Gamma_r \rho_{rr} \,, \tag{2.10b}$$
$$\partial_t \rho_{rr} = \Omega_c \mathrm{Im}[\rho_{er}] - \Gamma_r \rho_{rr} \,, \tag{2.10c}$$
$$\partial_t \rho_{ge} = -\Gamma_{ge} \rho_{ge}/2 + i\Omega_c \rho_{gr}/2 + i\Omega_p(\rho_{gg} - \rho_{ee})/2 \,, \tag{2.10d}$$
$$\partial_t \rho_{gr} = -\Gamma_{gr} \rho_{gr}/2 - i(\Omega_p \rho_{er} - \Omega_c \rho_{ge})/2 \,, \tag{2.10e}$$
$$\partial_t \rho_{er} = -\Gamma_{er} \rho_{er}/2 - i\Omega_p \rho_{gr}/2 - i\Omega_c(\rho_{rr} - \rho_{ee})/2 \,. \tag{2.10f}$$

Here, the combined rates

$$\Gamma_{ge} = \Gamma_e + \gamma_{ge} + 2i\Delta_p \,, \tag{2.11a}$$
$$\Gamma_{er} = \Gamma_e + \Gamma_r + \gamma_{er} + 2i\Delta_c \,, \tag{2.11b}$$
$$\Gamma_{gr} = \Gamma_r + \gamma_{gr} + 2i(\Delta_p + \Delta_c) \,. \tag{2.11c}$$

have been defined. In order to simplify the subsequent discussion, we also introduce the single-photon detuning $\Delta = \Delta_p$ and the two-photon detuning $\delta = \Delta_p + \Delta_c$ for the three-level system.

Finally, in steady-state and in the limit $\Omega_p \ll \Omega_c$, the susceptibility of the three-level system [103, 110]

$$\chi_{3\mathrm{lvl}} = \chi_0 \frac{i\Gamma_e \Gamma_{gr}^*}{\Gamma_{ge}^* \Gamma_{gr}^* + \Omega_c^2} \tag{2.12}$$

can be obtained from the OBE and Eq. (2.4).

### 2.1.3 Electromagnetically induced transparency

If the upper state $|r\rangle$ of the three-level system depicted in Fig. 2.1 is meta-stable, the susceptibility of the three-level system, Eq. (2.12), gives rise to an effect called electromagnetically induced transparency (EIT) [19, 20]. In the presence of a strong coupling field, the atomic medium is rendered transparent on two-photon resonance for a weak[1] probe field. This phenomenon is a consequence of destructive interference between different excitation pathways [99]. The effect of EIT was first proposed by Harris *et al.* [19] and shortly afterwards experimentally demonstrated by Boller *et al.* [20]. Since then many applications of EIT have been identified including enhanced frequency conversion [19]. For a detailed review on EIT we refer the reader to ref. [99] and only summarize the main aspects relevant for this thesis in the present section.

#### EIT dark state

The occurrence of EIT is connected to the presence of a dark state [99]

$$|D_{\mathrm{EIT}}\rangle = \frac{1}{\sqrt{\Omega_c^2 + \Omega_p^2}} \left[\Omega_c |g\rangle - \Omega_p |r\rangle\right] \tag{2.13}$$

[1] Here, we consider $\Omega_p < \Omega_c$. Changing to the opposite situation leads to a sizable population in the Rydberg state. This regime has been investigated, for example, in the context of coherent population trapping [84].

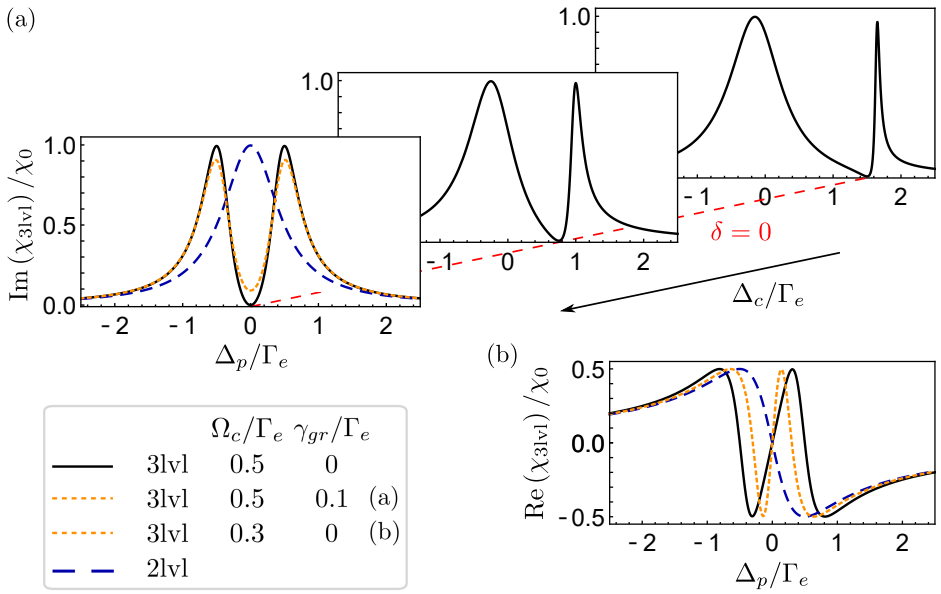


**Figure 2.2: EIT susceptibility.** Imaginary (a) and real (b) part of the three-level susceptibility $\chi_{3\text{lvl}}$, Eq. (2.12), as a function of the probe beam detuning $\Delta_p$ for different Rabi frequencies $\Omega_c$ of the control beam and different dephasing rates $\gamma_{gr}$, as indicated in the legend. The red dashed line connects points where $\text{Im}(\chi_{3\text{lvl}}) = 0$, which results from a vanishing two-photon detuning $\delta = \Delta_p + \Delta_c = 0$ in the absence of dephasing ($\gamma_{gr} = 0$). The susceptibility in the absence of the control beam, corresponding to the one of a two-level system, is shown as a blue dashed line for comparison in (a) and (b). In both plots we have chosen $\Omega_p/\Gamma_e = 0.02$ and $\Gamma_r = \gamma_{ge} = \gamma_{er} = 0$, and $\Delta_c/\Gamma_e = \{0, -0.75, -1.5\}$ in (a) from left to right and $\Delta_c = 0$ in (b).

that can be obtained by diagonalizing the Hamiltonian of the three-level system, Eq. (2.8), for $\delta = 0$. Remarkably, the dark state does not contain the intermediate state. As a consequence, an atom in this state does not scatter the probe field, hence the name dark state [99]. On two-photon resonance, all atoms settle into this dark state, which leads to the EIT transparency for the probe beam.

In Sec. 4.3.3 we discuss in more detail how this dark state can be populated adiabatically by using an appropriate pulse sequence of the applied fields [99]. We prepare $\Omega_p \ll \Omega_c$ for the experiments presented in Chap. 4, meaning that the dark state only possesses a small admixture of the upper state $|r\rangle$ and thus is mostly ground-state like.

### Spectral properties of the EIT susceptibility

Fig. 2.2(a) shows the imaginary part of the three-level susceptibility as a function of the probe and control field detuning $\Delta_p$ and $\Delta_c$, respectively. In the absence of the control field (blue dashed line), the susceptibility reproduces the one of a two-level system and displays strong absorption on resonance. However, the presence of the control field (black line) leads to $\text{Im}(\chi_{3\text{lvl}}) = 0$ on two-photon resonance $\delta = \Delta_p + \Delta_c = 0$ (indicated by the red dashed line), meaning that the probe field

is fully transmitted. The associated transparency window [99]

$$\Delta\omega_{tr} = \frac{\delta_{\mathrm{EIT}}}{\sqrt{\mathrm{OD}}} \tag{2.14}$$

is determined by the EIT linewidth [99]

$$\delta_{\mathrm{EIT}} = \frac{\Omega_c^2}{|\Gamma_e + i\Delta_p|} \tag{2.15}$$

and the optical depth OD of the atomic medium. Assuming $\Gamma_r = 0$, effects of EIT such as the transparency remain visible as long as [99]

$$\frac{|\Omega_c|}{\gamma_{gr}(\Gamma_e + \gamma_{ge})} \gg 1 \tag{2.16}$$

holds. For this reason, it is especially important to preserve the coherence between the two meta-stable states, which could e.g. be diminished by phase fluctuations of the laser fields [99]. If for example $\gamma_{gr} \neq 0$, as shown by the orange dotted line in Fig. 2.2, residual absorption of the probe field arises. Eq. (2.16) also implies, that if the dephasing $\gamma_{gr}$ is sufficiently small [99], EIT can be observed in atomic gases prone to a collisional broadening [111] or in solids [112].

### 2.1.4 Slow light

A transparency for the probe beam could also be realized by a large probe detuning. However, the effect of EIT is special in the sense that it does not only strongly alter the dissipative properties of the atomic medium, but also allows to tune the refraction experienced by the probe field [99]. As a consequence, light can be remarkably slowed down and a group velocity as low as 17 m/s for so called slow light has been observed [25].

In order to understand the origin of slow light in EIT settings, we recall that the refractive properties of the medium are related to the real part of the susceptibility via the refractive index $n = \sqrt{1 + \mathrm{Re}(\chi_{3\mathrm{lvl}})}$ [102]. In Fig. 2.2(b) we show the real part of the three-level susceptibility as a function of the probe field detuning. While in the absence of the control field (two-level situation, blue dashed line) the slope close to resonance is negative and thus leads to anomalous dispersion, the three-level system (black solid line) shows a steep positive slope, indicating normal dispersion [99]. Most importantly, the slope around zero detuning can be increased by decreasing the control field Rabi frequency as indicated in Fig. 2.2(b) by the orange dotted line.

The group velocity associated to the refractive index $n$ reads [25, 99, 104]

$$v_g = \frac{c}{n(\omega_p) + \omega_p \frac{\mathrm{d}n}{\mathrm{d}\omega_p}} = \frac{1}{1 + n_{gr}}\,, \tag{2.17}$$

where the second equality holds for a linear medium on two-photon resonance. Here, [99]

$$n_{gr} = \rho_0 \sigma_0 c \frac{\Gamma_e}{\Omega_c^2 + \gamma_{gr}(\Gamma_e + \gamma_{ge})} \tag{2.18}$$

is the group index and $\sigma_0$ the atomic cross section. It follows that the dispersive properties of EIT allow to remarkably reduce the group velocity inside an atomic medium, e.g. for small Rabi frequencies $\Omega_c$. The probe pulse gets delayed by a time $\tau_d = \mathrm{OD}\Gamma_e/\Omega_c^2$ [99] when traversing the medium, hence the name slow light. However, Eq. (2.17) also implies that the minimal group velocity is limited by the dephasing present in the system [99].

The transparency for the probe pulse is only maintained if its spectral width fits into the EIT transparency window, Eq. (2.14), as otherwise higher spectral components are absorbed [99]. This has severe consequences for the minimally achievable group velocity for a control field that is constant in time: While the spectral width of the probe pulse is not affected for a time-independent group velocity, the EIT transparency width decreases with the Rabi frequency $\Omega_c$ according to Eq. (2.15). For very small Rabi frequencies $\Omega_c$, the pulse spectral width exceeds the EIT transparency window, such that the probe pulse gets absorbed. Therefore, it is not possible to bring light to a complete stop inside an atomic medium with a static control field [99]. However, if the group velocity is reduced in time the spectral width of the probe pulse decreases. Therefore, the ratio of probe pulse to EIT width stays constant when dynamically reducing $\Omega_c$, and thus the group velocity, to zero [30]. As a result, light can be brought to a complete stop inside the atomic medium if $\gamma_{gr} = 0$. Stopping a classical light pulse was first achieved by Liu *et al.* [27] in a cold atomic gas as well as in an atomic vapor by Phillips *et al.* [28]. We complete this section by noting that a spatial reduction of the group velocity, e.g. at the entrance of the medium, is accompanied by a pulse compression given by the ratio $v_g/c$ [99].

### 2.1.5 Stationary light

In contrast to slow and stored light discussed in the previous section, a slight adaption of the conventional EIT systems enables to store a light field inside an atomic medium, while preserving its photonic character. This so-called stationary light is realized by coupling two counter-propagating probe field modes, for which EIT conditions involving the same spin-wave coherence are fulfilled individually [31–33, 37].

Consider for example the $\Lambda$-coupling scheme [32, 42], shown on the left of Fig. 2.3. Here, two counter-propagating control fields with Rabi frequencies $\Omega_{c\pm}$ couple an excited state $|e\rangle$ to a meta-stable state $|d\rangle$. They form an intensity grating that modulates the EIT condition periodically for a probe field, which couples the ground state $|g\rangle$ to the excited state $|e\rangle$. Under phase matching conditions and on four-photon resonance, right- and left-moving probe field modes interfere. Moreover, if $\Omega_{c+} = \Omega_{c-}$, they form a stationary wave pattern. As a result, the probe field can reside in the medium with zero group velocity [32, 42].

After the theoretical prediction of stationary light [31, 32] it was first experimentally observed with the described $\Lambda$ level scheme in a hot atomic vapor by Bajcsy *et al.* [32]. There the stationary field was generated by first storing a probe field inside an atomic medium as an atomic excitation and afterwards retrieving it by turning on the counter-propagating control fields simultaneously.

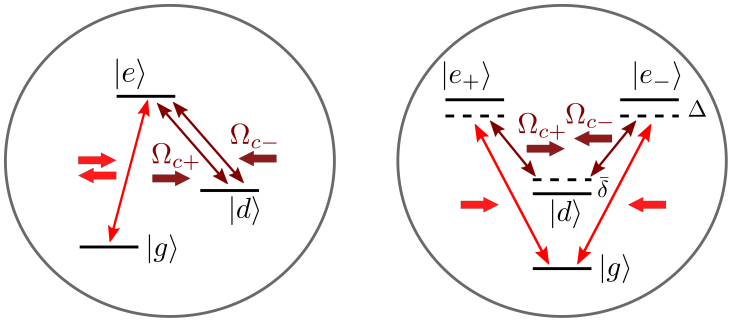


$\Lambda$ level scheme dual-V level scheme

**Figure 2.3: Level schemes for stationary light.** $\Lambda$ (left) and dual-V (right) level scheme support the formation of stationary light as a consequence of interfering left- and right-moving probe fields. Arrows indicate the propagation direction of the fields. For a detailed description and the notation see the main text.

At the same time, it was shown, that under continuous-wave conditions, i.e. if the counter-propagating control beams continuously illuminate the medium, an incident probe beam gets reflected with a high probability, such that the medium behaves like a mirror [32].

The described realization of stationary light with the $\Lambda$ level scheme has the drawback that multiple absorption and re-emission processes in counter-propagating fields can occur [37]. For example, a right-moving probe photon might be scattered into the left-moving control field, leading to a ground- to meta-stable state coherence at a higher momentum [37–41]. While these higher order spatial modes decay quickly in hot vapors due to atomic motion induced dephasing, they prevent the formation of stationary light in cold atom experiments [37, 38]. Detuning from the excited state, such that higher spatial modes become negligible, has solved this problem for the $\Lambda$ level scheme, and enabled the first experimental observation of stationary light in cold atomic ensembles [35, 43].

The dual-V level scheme [34, 37], depicted on the right in Fig. 2.3, also supports stationary light for control fields of equal strength. Here, higher order spatial modes are completely prohibited [34]. The reason is that the two pairs of probe and control fields couple the spin-wave coherence between the states $|g\rangle$ and $|d\rangle$ via two disjunct intermediate states $|e_\pm\rangle$. The complete absence of higher order spatial modes makes this scheme particularly useful for the realization of stationary light in cold atomic ensembles [34]. Furthermore, with a proper choice of atomic hyperfine sublevels, the difference between the frequencies of the probe and control fields can be small. This simplifies phase matching in an experimental realization of this scheme. We present a more quantitative discussion of stationary light with this level scheme in Sec. 2.2.3. For this purpose, we have already included equal single- and two-photon detuning $\Delta$ and $\bar{\delta}$ for the two pairs of co-propagating beams, respectively, in the level scheme shown in Fig. 2.3.

## 2.2 Quantum mechanical description of light propagation

In contrast to the semiclassical case, where the probe field is well described by a Rabi frequency, in the quantum regime photon-photon and photon-atom correlations have to be taken into account [77]. In the following, we review the propagation of a quantized probe field $\hat{\mathcal{E}}(\mathbf{r},t)$ through an atomic medium. First, we introduce in Sec. 2.2.1 a quantum mechanical description for atom-light interactions in three-level and dual-V atomic level schemes. We proceed by linking the phenomena of EIT and slow light to the formation of a dark-state and slow-light polariton in Sec. 2.2.2. Finally, we introduce in Sec. 2.2.3 stationary light polaritons, which are the counterpart of stationary light in the quantum regime.

### 2.2.1 Maxwell-Bloch equations

Assuming a weak quantized probe field $\hat{\mathcal{E}}(\mathbf{r},t)$, the atoms mainly populate the ground state. This permits to introduce bosonic operators $\hat{P}(\mathbf{r},t)$ and $\hat{S}(\mathbf{r},t)$ for the collective polarization and spin-wave coherences, respectively [26, 30, 77, 113]. As in the semiclassical description, the propagation of the probe field is determined by the polarization coherence.

In the case of the three-level system depicted in Fig. 2.1 and within the paraxial approximation, the dynamics of the quantized probe field and the coherences are described[2] by the Maxwell-Bloch equations [77, 115, 116]

$$\partial_t\hat{\mathcal{E}}(\mathbf{r},t) = \left(ic\frac{\nabla_\perp^2}{2k_p} - c\partial_z\right)\hat{\mathcal{E}}(\mathbf{r},t) - ig\sqrt{\rho(\mathbf{r})}\hat{P}(\mathbf{r},t)\,, \tag{2.19a}$$

$$\partial_t\hat{P}(\mathbf{r},t) = -ig\sqrt{\rho(\mathbf{r})}\hat{\mathcal{E}}(\mathbf{r},t) - i\Omega(\mathbf{r})\hat{S}(\mathbf{r},t) - \Gamma_p\hat{P}(\mathbf{r},t)\,, \tag{2.19b}$$

$$\partial_t\hat{S}(\mathbf{r},t) = -i\Omega(\mathbf{r})\hat{P}(\mathbf{r},t) - \Gamma_s\hat{S}(\mathbf{r},t)\,. \tag{2.19c}$$

Here, $g$ is the single-atom coupling strength, $k_p$ is the wavevector of the probe field and $\rho(\mathbf{r})$ denotes the atomic density. Moreover, we have introduced $\Gamma_p = \Gamma_e/2 - i\Delta$, $\Gamma_s = \Gamma_r/2 - i\delta$ and $\Omega = \Omega_c/2$ for convenience.

In steady-state one can solve Eqs. (2.19b) and (2.19c) for the expectation value of the polarization coherence $\hat{P}(\mathbf{r},t)$. Relating it to the optical response of the atomic medium yields the same three-level susceptibility, Eq. (2.12), as derived in Sec. 2.1.2 in the semiclassical description [96].

Likewise, the Maxwell-Bloch equations for the dual-V scheme shown in Fig. 2.3 read [34, 44, 117]

$$\partial_t\hat{\mathcal{E}}_\pm(\mathbf{r},t) = \left(ic\frac{\nabla_\perp^2}{2k_\pm} \mp c\partial_z\right)\hat{\mathcal{E}}_\pm(\mathbf{r},t) - ig\sqrt{\rho(\mathbf{r})}\hat{P}_\pm(\mathbf{r},t)\,, \tag{2.20a}$$

$$\partial_t\hat{P}_\pm(\mathbf{r},t) = -ig\sqrt{\rho(\mathbf{r})}\hat{\mathcal{E}}_\pm(\mathbf{r},t) - i\Omega\hat{D}(\mathbf{r},t) - \Gamma_p\hat{P}_\pm(\mathbf{r},t)\,, \tag{2.20b}$$

$$\partial_t\hat{D}(\mathbf{r},t) = -i\left[\Omega_+\hat{P}_+(\mathbf{r},t) + \Omega_-\hat{P}_-(\mathbf{r},t)\right] - i\bar{\delta}\hat{D}(\mathbf{r},t) \tag{2.20c}$$

and describe the propagation of the two probe fields with wavenumber $k_\pm$, for which the respective quantities are labeled by the indices $+$ and $-$. Both fields

[2] A detailed derivation of these equations can for example be found in refs. [77, 114].

couple with equal strength to the intermediate states $|e_\pm\rangle$, where $\hat{P}_\pm(\mathbf{r},t)$ denotes the corresponding polarization coherence. We assume that the intermediate states decay with the same rate $\Gamma_e$. The coherence between the ground state $|g\rangle$ and the meta-stable state $|d\rangle$ is described by the operator $\hat{D}(\mathbf{r},t)$. Moreover, for simplicity we have assumed equal single- and two-photon detuning $\Delta$ and $\bar{\delta}$ for the two pairs of co-propagating beams.

For one-dimensional systems, where the fields propagate along the $z$ direction and the transversal dependence of the field can be neglected, the Maxwell-Bloch equations can be cast into the matrix form [34, 114]

$$i\partial_t \Upsilon = \mathcal{H}_{\text{eff}} \Upsilon \,, \tag{2.21}$$

where the column vector $\Upsilon \in \{\Upsilon_{\text{3lvl}}, \Upsilon_{\text{dual-V}}\}$ Hereby, $\Upsilon_{\text{3lvl}} = \left(\hat{\mathcal{E}}, \hat{S}, \hat{P}\right)^T$ and $\Upsilon_{\text{dual-V}} = \left(\hat{\mathcal{E}}_+, \hat{\mathcal{E}}_-, \hat{D}, \hat{P}_+, \hat{P}_-\right)^T$. The coefficient matrix $\mathcal{H}_{\text{eff}} \in \{\mathcal{H}_{\text{eff,3lvl}}, \mathcal{H}_{\text{eff,dual-v}}\}$ can be readily obtained from Eqs. (2.19) and Eqs. (2.20), respectively.

### 2.2.2 Dark-state and slow-light polaritons

In Sec. 2.1.3 we have discussed that EIT is connected to the formation of a dark state. Analogously on finds in the quantum regime a quasi-particle called dark-state polariton (DSP) [26] from a momentum space formulation of $\mathcal{H}_{\text{eff,3lvl}}$, Eq. (2.21), for negligible photon dispersion [117]. Hereby, the dark-state polariton is the eigenstate with zero eigenvalue. Explicitly, the form of the DSP reads [26, 117]

$$\hat{\Psi}_{\text{DSP}} = \frac{1}{\sqrt{\Omega^2 + G^2}} \left[\Omega\hat{\mathcal{E}} - G\hat{S}\right] \,, \tag{2.22}$$

where we have used the abbreviation $G = g\sqrt{\rho_0}$ with $\rho_0$ being the constant atomic density. The DSP is composed of a photonic excitation and an atomic coherence. It inherits dynamics from the photonic component and, as we discuss in the subsequent chapter, may inherit interactions from its atomic component [77]. In contrast to the other two eigenstates of $\mathcal{H}_{\text{eff,3lvl}}$, which are commonly called bright-state polaritons (BSP) [30], the DSP does not contain the polarization coherence. For this reason, it does not decay [30].

Fig. 2.4 shows the dispersion relation $\omega(k)$ for the dark-state and bright-state polaritons as a function of the photon momentum $k$. This quantity can be obtained by diagonalizing $\mathcal{H}_{\text{eff,3lvl}}$, given in Eq. (2.21), numerically in momentum space. In addition, an approximate expression for the dispersion relation $\omega_{\text{DSP}}(k)$ for the DSP at small photon momenta can be calculated using either perturbation theory or the Lagrange-multiplier formalism[3] [114]. One obtains [26, 117]

$$\omega_{\text{DSP}}(k) \approx c\left[\frac{\Omega^2}{\Omega^2 + G^2}\right] k + \mathcal{O}(k^2) \,, \tag{2.23}$$

[3] I thank J. Otterbach for helpful discussions and an example calculation illustrating this method.

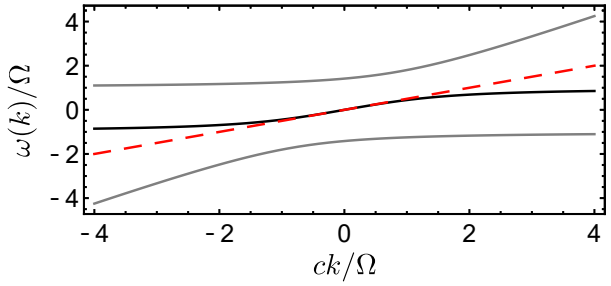


**Figure 2.4: Dispersion relation of the three-level system.** Dispersion $\omega(k)$ as a function of the photon momentum $k$. Three branches, belonging to one dark-state (black) and two bright-state polaritons (gray), are visible. The dispersion relation of the dark-state polariton exhibits a linear slope around zero, which is well approximated by Eq. (2.23), as indicated by the red dashed line. Parameters are $G = \Omega = \Gamma_e = 1$ and $\Delta = \delta = \Gamma_r = 0$. Parameters and scaling of the axes are chosen as in ref. [114].

which shows linear dispersion with group velocity $v_g = \mathrm{d}\omega_{\mathrm{DSP}}(k)/\mathrm{d}k$. In the adiabatic limit, where the BSPs are not populated, and on two-photon resonance, the DSP follows in one dimension the simple equation of motion [26]

$$[\partial_t + v_g \partial_z]\, \hat{\Psi}_{\mathrm{DSP}} = 0\,. \tag{2.24}$$

It describes a form-stable propagation with group velocity $v_g$. For $G \gg \Omega$ the group velocity is remarkably reduced and the polariton is commonly called a slow-light polariton [118]. Adiabatically reducing the Rabi frequency of the control field to zero, ultimately allows to fully transfer the polariton to a collective spin-wave excitation. Thereby, the polariton is completely stopped inside the medium [30]. Full conversion to an atomic coherence is only possible in the absence of dephasing, as discussed in Sec. 2.1.4. Moreover, the spectral width of the probe pulse has to fit into the EIT transparency window and the control field needs to be switched sufficiently slow to avoid coupling to the BSPs [30, 99, 114]. Both conditions can be realized in atomic media with large optical depth OD [30, 99, 114].

Storing single photons inside an atomic medium as a spin-wave coherence opens the route for quantum memory devices [30], as it been experimentally demonstrated by Eisaman *et al.* [29] and Chanelière *et al.* [101].

### 2.2.3 Stationary light polaritons

As discussed in Sec. 2.1.5, stationary light is supported in the dual-V level scheme if the control fields have equal strength[4] ($\Omega_{c+} = \Omega_{c-} = \Omega$). Similar to slow light, stationary light is linked to the formation of a so-called stationary light polariton (SLP) [31, 34, 44, 117]. Its form can be obtained from a momentum

[4] We note that refs. [34, 114] define $\Omega^2 = \Omega_{c+}^2 + \Omega_{c-}^2$. Thus, for a comparison with these references in the case of $\Omega_{c+} = \Omega_{c-}$, $\Omega$ in our equations based on ref. [117] needs to be replaced by $\Omega/\sqrt{2}$.

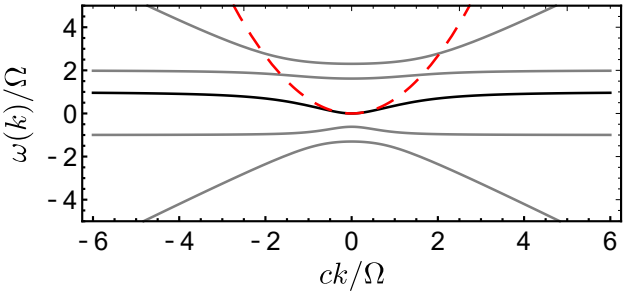


**Figure 2.5: Dispersion relation of the dual-V level system.** Dispersion $\omega(k)$ as a function of the photon momentum $k$. Five branches, belonging to the stationary light polariton (black) and four bright-state polaritons (gray), are visible. The dispersion of the stationary light polariton is quadratic around zero and is well approximated by the expression given in Eq. (2.26), as indicated by the red dashed line. Parameters are $G = \Omega = -\Delta = 1$ and $\delta = \Gamma_e = 0$. Parameters and scaling of the axes are chosen similar as in ref. [114].

space formulation of $\mathcal{H}_{\text{eff,dual-v}}$ for negligible photon dispersion and reads [34, 117]

$$\hat{\Psi}_{\text{SLP}} = \frac{1}{\sqrt{G^2 + 2\Omega^2}} \left[\Omega\left(\hat{\mathcal{E}}_+ + \hat{\mathcal{E}}_-\right) - G\hat{D}\right] . \tag{2.25}$$

The SLP is accompanied by four bright-state polaritons and displays a quadratic dispersion at small momenta, as shown in Fig. 2.5. Again, an approximate expression [34, 117]

$$\omega_{\text{SLP}}(k) \approx -\frac{2ic^2\Gamma_p}{G^2}\left[\frac{\Omega^2}{G^2 + 2\Omega^2}\right] k^2 + \mathcal{O}(k^3) \tag{2.26}$$

can be derived in the adiabatic limit and using the Lagrange-multiplier method. As a consequence of the quadratic dispersion relation at small $k$, stationary light polaritons follow the equation of motion [34]

$$\left[\partial_t + \frac{i\hbar}{2m_{\text{eff}}}\partial_z^2\right] \hat{\Psi}_{\text{SLP}} = 0 . \tag{2.27}$$

If $|\Delta| \gg \Gamma_e/2$, the stationary light polariton behaves like a particle with effective mass $m_{\text{eff}} = \hbar[\mathrm{d}^2\omega(k)/\mathrm{d}k^2]^{-1}$, whose dynamics is governed by the Schrödinger-like equation, Eq. (2.27) [44, 114]. In the opposite case ($|\Delta| \ll \Gamma_e/2$), it shows diffusive behavior [42, 114, 119]. We want to note that $\Omega_{c+} \neq \Omega_{c-}$ leads to a finite group velocity proportional to $(\Omega_{c+}^2 - \Omega_{c-}^2)$. As a consequence, the SLP co-propagates with the control field of higher strength [32]. Stationary light in the quantum regime has been experimentally observed with Rubidium atoms in a magneto-optical trap [36] and in a hollow-core fiber [120].

CHAPTER 3

# A two-body, two-photon resonance in Rydberg EIT

*Parts of this chapter are based on the following publication*[5]*, from which parts of the text have been taken verbatim*:

> **Blockade-induced resonant enhancement of the optical nonlinearity in a Rydberg medium**
> A. Tebben, C. Hainaut, V. Walther, Y.-C. Zhang, G. Zürn, T. Pohl and M. Weidemüller, Phys. Rev. A **100**, 063812 (2019)

In the previous Chap. 2 we have assumed that the induced polarization of the medium is proportional to the applied field, which implies a linear optical response of the system. However, at large field strengths the polarization depends nonlinearly on the applied field and higher order susceptibilities arise [122, 123]. As a result, nonlinear processes such as high harmonic generation [13, 14] and an intensity-dependent refractive index emerge [122]. Only due to the development of high intensity lasers these effects have become experimentally accessible [4, 12, 122, 123]. The reason is that these lasers can provide the required strong electric field that make the nonlinear terms to the leading order contributions in the optical response.

However, aiming at optical nonlinearities on the single-photon level, it is not the electric field, but the higher order susceptibilities themselves that need to be enhanced with respect to the linear response of the medium. Combining the coherent light-matter coupling induced by EIT with strong interactions between Rydberg atoms proved to be a promising solution for achieving strong nonlinearities [4, 23, 61, 63, 77, 85]. While the linear response of the medium is canceled on two-photon resonance under EIT conditions, atomic interactions induce a strong third-order nonlinearity to the system that exceeds the one of conventional media by orders of magnitude [61, 63, 85]. Moreover, effective photon-photon interactions [24, 57, 59, 70–73, 115, 124] arise with possible applications in the field of quantum

[5] The foundation of this work has been laid in my Master thesis [121].

information processing [7–10] and in the generation of non-classical states of light [4–6].

In the introduction of this thesis we have raised the question of how to model this strongly interacting Rydberg EIT system. Various semiclassical models exists [23, 58, 64, 65, 78, 80, 82, 124, 125]. In some of them the dynamics of the intermediate state is adiabatically eliminated. This approximation is well justified for a large detuning to the intermediate state. However, when the intermediate state is explicitly taken into account interesting effects can be revealed [96]. For example, an enhancement of the atomic pair potential, collective effects leading to an enhanced Rydberg excited fraction, and a preservation of coherence as a consequence of suppressed photon scattering have been predicted in the semiclassical regime [79, 126, 127].

In this chapter we investigate Rydberg EIT on two-photon resonance without an adiabatic elimination of the intermediate state dynamics. Extending previous theoretical investigations [58, 121, 126], we find that an enhancement of the nonlinear response of the Rydberg EIT medium emerges as a consequence of a resonance effect [96].

This chapter is structured as follows: We start in Sec. 3.1 with an overview of basic properties of Rydberg atoms and their interactions. In Sec. 3.2 we review the basic concept of Rydberg EIT from a semiclassical and, for completeness, from a quantum mechanical perspective. While in the semiclassical regime the interaction-induced optical nonlinearity is best described by a third-order susceptibility, in the quantum regime effective photon-photon interactions can be understood based on interacting polaritons [77, 85]. Based on this theoretical background, we develop in Sec. 3.3 an intuitive picture for the enhanced nonlinear response of the Rydberg EIT medium in the semiclassical regime [96]. We present a model that allows to derive an analytic expression for the associated nonlinear susceptibility [121]. Moreover, we explain with the help of our intuitive picture the spatial shape of the enhanced susceptibility, and investigate its scaling with relevant system parameters [96]. Finally, we summarize and discuss our results in Sec. 3.4.

## 3.1 Rydberg atoms

Due to their extraordinary properties, as for example a huge polarizability, Rydberg atoms offer a versatile platform for quantum simulations and technologies [50–52], information processing [53], and nonlinear optics [52, 63, 77, 85] as discussed in this chapter. For an in-depth and comprehensive review of Rydberg atoms the reader is referred to the literature, e.g. refs. [46–49]. In this section we only briefly summarize the main aspects relevant for this thesis. First, we introduce the basic properties of Rydberg atoms in Sec. 3.1.1, ranging from the characteristic scaling of their properties with the quantum number $n$ to strong interactions between Rydberg atoms. Afterwards, we put in Sec. 3.1.2 the focus on different existing theoretical models that include Rydberg interactions. They become important for the investigation of nonlinear optics with Rydberg atoms

in the remainder of the present and in subsequent chapters.

### 3.1.1 Basic properties

Rydberg atoms are atoms where one or more valence electrons are excited to a high principal quantum number $n$. For alkali Rydberg atoms with one valence electron, such as Rubidium (Rb) which is considered in this thesis, the binding energy [103, 128]

$$E_{n,l,j} = -hc\frac{R_{Rb}}{(n^*)^2} \tag{3.1}$$

for the state $|n, l, j\rangle$ is hydrogen-like with the distinction that the quantum number $n$ needs to be replaced by the effective quantum number $(n^*) = n - \delta_{n,l,j}$. Here, the quantum defect $\delta_{n,j,l}$ takes into account core-penetration of the electron for low angular momentum states [46]. Furthermore, $R_{Rb}$ is the Rydberg constant for Rubidium atoms, $h$ is the Planck constant and $c$ denotes the speed of light.

Small binding energies for large quantum numbers in combination with the large distance between the atomic core and the outer electron result in a large polarizability of Rydberg atoms scaling as $(n^*)^7$ [46]. As a consequence, Rydberg atoms are strongly affected by external electric fields. For this reason, a precise control of stray electric fields is required in experimental setups [129]. However, at the same time the sensitivity to external fields permits to detect Rydberg excitations via field ionization [46]. The radiative lifetime of Rydberg atoms scales as $(n^*)^3$ for low angular momentum states [46], as the overlap with the ground state is small. This results in radiative lifetimes[6] in the order of $100\,\mu$s, which is much longer than typical experimental timescales[7]. Therefore, Rydberg states are considered to be meta-stable.

#### Rydberg-Rydberg interactions for $|nS\rangle$ states

Rydberg atoms possess strong interactions that result in a classical picture from the interaction between induced dipole moments [48]. For a quantum mechanical description of Rydberg interactions, we closely follow the discussion in refs. [48, 103, 104]. We consider the interaction between two Rydberg atoms separated by a distance larger than the LeRoy radius [131]. In this case their interaction can be described by the dipole-dipole interaction [47, 103]

$$\hat{V}_{dd}(\mathbf{R}) = \frac{\hat{\mathbf{d}}_1 \cdot \hat{\mathbf{d}}_2}{R^3} - \frac{3(\hat{\mathbf{d}}_1 \cdot \mathbf{R})(\hat{\mathbf{d}}_2 \cdot \mathbf{R})}{R^5}\,. \tag{3.2}$$

Here, $\hat{\mathbf{d}}_{1,2}$ are the dipole operators acting on the two atoms, respectively, and $\mathbf{R}$ is the vector connecting the two atomic cores with inter-nuclear distance $R$.

[6] Rydberg atom properties used within this thesis are calculated with the Alkali Rydberg Calculator (ARC) [130].

[7] Black-body induced decay to nearby Rydberg states reduce the effective lifetimes. For the Rydberg state $|48S\rangle$ considered in this thesis, the radiative lifetime of about $113\,\mu$s is reduced to an effective lifetime of about $57\,\mu$s. However, this is still large compared to typical experimental time scales ranging from 5 to $15\,\mu$s.

In this thesis we work with $^{87}$Rb atoms excited to the Rydberg state $|48S\rangle$. Hence, we consider both atoms to be excited to a Rydberg state $|nS\rangle$. Moreover, we neglect the angular dependence of the interaction in the following, which is a good approximation for Rydberg atoms in $|nS\rangle$ states [132, 133].

By using perturbation theory, it is possible to calculate the energy shift of the pair-state $|nS, nS\rangle$ resulting from the dipole coupling [48]. For parity reasons, the first-order energy correction vanishes. For the second-order contribution, in principle, a plethora of other coupled pair-states would need to be considered. Nevertheless, as the energy correction scales with the inverse of the energy difference $\Delta E$ of the pair-states, we only take into account the energetically closest pair-state $|nP, n'P\rangle$ in a simplified two-atom model [48, 103, 104].

For non-degenerate pair-states, i.e. for $\Delta E \gg V_0 = \langle nS, nS| \hat{V}_{dd}(\mathbf{R}) |nP, n'P\rangle$ [103] as it is the case for large atomic separations, this results in a second-order energy shift [48, 104, 134]

$$E_{\mathrm{vdW}}(R) = \hbar C_6 / R^6 \,, \tag{3.3}$$

where the interaction coefficient $C_6 \propto (d_1 d_2)^2 / \Delta E$. The dipole matrix elements $d_{1,2}$ and the energy difference between adjacent $n$ states scale as $(n^*)^2$ and $(n^*)^{-3}$, respectively [46]. Therefore, the coefficient $C_6$ exhibits a strong dependence on the effective quantum number scaling as $(n^*)^{11}$. Moreover, the interaction coefficient determines the sign of the resulting van der Waals interactions. In our case the $|48S\rangle$ states possess strong repulsive interactions [103, 104].

For small inter-nuclear distances $R$ or for degeneracy with $\Delta E = 0$, corresponding to a so-called Förster resonance [54], the energy shift can be obtained by diagonalizing the Hamiltonian [48, 103]

$$\hat{H}_{\mathrm{pair}} = \begin{pmatrix} 0 & V_0 \\ V_0 & \Delta E \end{pmatrix} \tag{3.4}$$

of the reduced system, given in the basis of the two-pair states $|nS, nS\rangle$ and $|nP, n'P\rangle$. A Taylor expansion of the eigenenergies of the Hamiltonian $\hat{H}_{\mathrm{pair}}$ for $\Delta E \gg V_0$ yields the van der Waals type energy shift scaling as $1/R^6$ discussed above [104]. However, an expansion for $\Delta E \ll V_0$ results in an energy shift of $E_{dd}(R) = \hbar C_3 / R^3$ [48, 103, 104, 134]. As the coefficient $C_3 \propto d_1 d_2$, the resulting dipole-dipole interactions scale as $(n^*)^4$. The two regimes of van der Waals and dipole-dipole interactions can be separated in terms of the so-called van der Waals radius $R_{\mathrm{vdW}} = (\hbar c_3 / \Delta E)^{1/3}$ [48, 103].

For the sake of completeness, we note that dipole-dipole interactions also arise for two Rydberg atoms in states of opposite parity as the first-order energy correction does not vanish [48]. Moreover, dipole-dipole interactions become important if the atoms are exposed to a static electric field, since permanent dipole moments are induced [48, 104].

### Rydberg blockade effect

Rydberg-Rydberg interactions have a profound consequence on the Rydberg excitation dynamics. Fig. 3.1 displays the pair-state energies of two atoms either

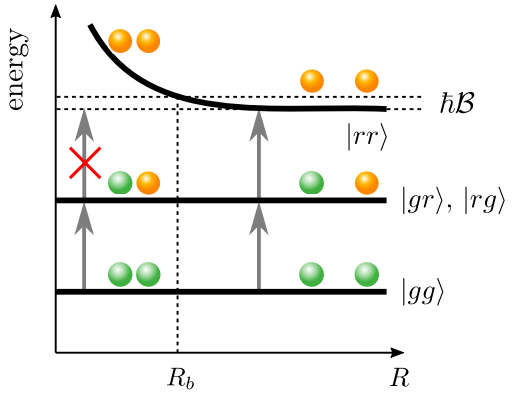


**Figure 3.1: Rydberg blockade effect.** Energies of relevant pair-states as a function of the inter-particle distance $R$. Green (orange) spheres illustrate atoms in the ground (Rydberg) state. For small separations, the doubly excited Rydberg state $|rr\rangle$ is shifted due to Rydberg-Rydberg interactions. As a consequence, excitation of this state is prohibited for inter-particle distances smaller than $R_b$. $\mathcal{B}$ is the Rydberg excitation bandwidth. Figure adapted from refs. [104, 121], with kind permission of M. Gärttner.

being in the ground state $|g\rangle$ or excited to a Rydberg state $|r\rangle$ as a function of the inter-particle distance $R$. As a consequence of Rydberg-Rydberg interactions, the doubly excited Rydberg state $|rr\rangle$ experiences an energy shift, which is $E_{\mathrm{vdW}}(R)$ for van der Waals interactions. For very small inter-particles distances the state $|rr\rangle$ is shifted out of resonance for the excitation laser. Therefore, the simultaneous excitation of two Rydberg atoms is prohibited for $R < R_b$. Here, the so-called blockade radius $R_b$ is determined by the Rydberg excitation bandwidth $\mathcal{B}$ via the equation $\Delta E_{\mathrm{vdW}}(R_b) = \hbar\mathcal{B}$. This Rydberg blockade effect [54–56] is the key to a strong nonlinear optical response of an atomic gas, as explained in Sec. 3.2.

### 3.1.2 Theoretical models for Rydberg-Rydberg interactions

In Sec. 2.1 we have discussed that the optical response of an atomic gas is directly related to the atomic coherence $\rho_{eg}$, which can be derived from the single-body OBE, Eq. (2.10). However, Rydberg-Rydberg interactions introduce strong atom-atom correlations, such that a single-body treatment is no longer sufficient to capture the complete dynamics of the system [104]. Instead, the full many-body optical Bloch equations need to be solved for the atomic coherence $\rho_{eg}$. Due to the interaction terms, the corresponding equations for the density matrix elements $\rho^{(i)}_{\alpha\beta}$ with $\alpha, \beta \in \{g, e, r\}$ of the $i$-th atom now contain two-body correlators $\rho^{(i,j)}_{\alpha\beta,\alpha'\beta'}$ [62, 84]. These quantities themselves depend on three-body correlators and so forth . This hierarchy of equations requires to solve the full N-body dynamics. Since this is computationally demanding, exact and numerical solutions of the many-body optical Bloch equations are typically restricted to a few atoms [23, 78, 79]. Suitable truncation methods have been found to approximate the many-body dynamics. In the following, we collect the most important ones for this thesis.

The simplest truncation completely neglects atom-atom correlations in a so-called mean-field approach, that is $\rho^{(i,j)}_{\alpha\beta,\alpha'\beta'} \approx \rho^{(i)}_{\alpha\beta}\rho^{(j)}_{\alpha'\beta'}$ [56, 84, 135, 136]. This approximation is justified as long as the distance between Rydberg excitations is large. Applying this approach to the many-body OBE, Rydberg-Rydberg interactions are solely included as level shifts of the Rydberg state. Going beyond this crude approximation, higher-order correlations can be taken into account by means of a cluster expansion [84]. With this approach two-atom correlations are treated exactly and three-body effects are approximately included.

Another approach to solve the many-body OBE is based on the assumption that coherences decay fast compared to populations. As a consequence, this allows to obtain equations of the form $\partial_t \rho^{(i)}_{\alpha\alpha} = -a_{\alpha\alpha}\rho^{(i)}_{\alpha\alpha} + \sum_{j\neq i} a_{\alpha\beta}\rho^{(j)}_{\beta\beta}$ [62, 81, 82] for the populations only. Atomic interactions can straightforwardly be included in this model as an effective detuning $\Delta^{(i)}_{c,\mathrm{eff}} = \Delta^{(i)}_c - \sum_{j\neq i} V_{ij}\rho^{(j)}_{rr}$ [81], and the resulting rate equations can be solved in a Monte-Carlo approach. This model includes many-body correlations approximately.

## 3.2 Rydberg EIT

If the state $|r\rangle$ of the three-level ladder system depicted in Fig. 2.1 is a Rydberg state, Rydberg-Rydberg interactions strongly affect the propagation of a light field under EIT conditions. Moreover, as explained in the following, they render the medium highly nonlinear as a consequence of the Rydberg blockade effect [21–24]. Due to the long-range character of the Rydberg-Rydberg interactions, the resulting optical nonlinearity of the Rydberg EIT medium is not only very strong, but also highly nonlocal [77].

A strong nonlinear optical response on the single-photon level ultimately allows for effective photon-photon interactions [24, 115, 124]. This makes the field of Rydberg EIT promising for applications for example in optical information processing [7–10]. Of particular importance in this regard is the question how strong the light field is affected within one blockade radius, i.e. in terms of attenuation and phase shift. A measure for this is the optical depth per blockade radius [77, 115]

$$\mathrm{OD}_b = \mathrm{OD}\frac{R_b}{L} = \frac{2g^2\rho R_b}{c\Gamma_e}\,, \tag{3.5}$$

where $L$ is the length of the atomic medium and $R_b$ is the blockade radius for van der Waals type interactions $V(R) = C_6/R^6$ defined via [77, 115]

$$V(R_b) = \delta_{\mathrm{EIT}}\,. \tag{3.6}$$

Here, $\delta_{\mathrm{EIT}}$ is the EIT linewidth, Eq. (2.14).

For $\mathrm{OD}_b \ll 1$, the effect of the nonlinearity on the light field is weak and the coherent nature of the light field remains unchanged. Therefore, it can be treated classically [77]. This domain defines the semiclassical regime of Rydberg EIT, where the Rydberg EIT nonlinearity is best described in terms of a nonlinear susceptibility, as illustrated in Fig. 3.2(a). However, for $\mathrm{OD}_b > 1$ the light field experiences a substantial attenuation and phase shift on the single-photon level,

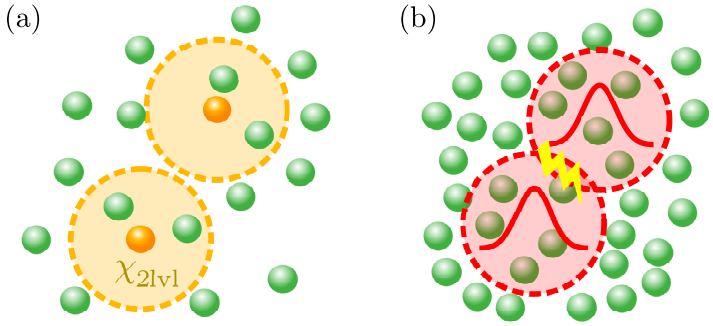


**Figure 3.2: Rydberg EIT nonlinearity.** Simplified illustration of Rydberg nonlinear optics (a) in the semiclassical regime ($OD_b \ll 1$) and (b) in the quantum regime ($OD_b > 1$). Green (orange) circles depict atoms in the ground- (Rydberg) state and dashed circles the blockade radius. Red objects in (b) illustrate two interacting polaritons.

when traversing the distance of one blockade radius. As a consequence, the photon statistics changes, giving rise to the quantum regime of Rydberg EIT [77]. Here, effective interactions between polaritons emerge, as schematically shown in Fig. 3.2(b). A detailed discussion on Rydberg EIT can be found, for example, in refs. [77, 85]. In the following, we briefly convey the general idea of Rydberg EIT and give a short overview over some relevant theoretical models in the semiclassical and quantum regime in Sec. 3.2.1 and Sec. 3.2.2, respectively.

### 3.2.1 Semiclassical regime: Nonlinear susceptibility

In Sec. 2.1.3 we have explained in the semiclassical regime the phenomenon of EIT based on the occurrence of a dark-state. However, if $|r\rangle$ is a Rydberg state, the dark-state contains a Rydberg component and Rydberg-Rydberg interactions have to be taken into account. In this case the atoms can no longer independently settle into the dark-state [77]. Instead, within one blockade volume only one Rydberg excitation is allowed, which destroys the EIT condition for all other atoms in that volume. Hence[8], these blockaded atoms can effectively be modeled as two-level atoms, and thus scatter the incoming probe light according to the two-level susceptibility $\chi_{2lvl}$, as schematically illustrated in Fig. 3.2(a). This is in sharp contrast to the EIT transparency, which the probe beam experiences in the non-interacting case. The more Rydberg atoms are excited and the more ground state atoms are within one blockade volume, the larger is the number of blockaded atoms. As a consequence, the optical response of the medium is increasingly dominated by the two-level response of the blockaded atoms [77]. At the same

[8] We note that this picture oversimplifies the system, as the level-shift induced by Rydberg interactions is considered to be infinite inside the blockade volume and zero outside. For an appropriate model this hard cut-off has to be relaxed and interaction-induced level shifts beyond the distance of a blockade radius need to be considered. This is for example pursued in refs. [64, 82].

time, the fraction of Rydberg excitations scales approximately as $\rho_0\Omega_p^2/\Omega_c^2$ [58, 82, 125]. This means that the optical response of the medium depends on the intensity of the probe field, such that an optical nonlinearity arises [58, 77, 82]. Moreover, as the Rydberg blockade radius is typically on the order of a few micrometer, the nonlinear response of the Rydberg EIT medium is also nonlocal [58, 59].

The modified optical response of the medium results in a nonlinear propagation of the probe beam. The most prominent observable consequence is the blockade-induced nonlinear absorption of the probe beam on resonance [23, 58, 60, 62, 64, 65, 77, 85]. This feature led for example to a novel method of imaging Rydberg impurities [67]. But also in the dispersive regime, where the probe beam detuning is large compared to the decay rate of the intermediate state, interesting effects such as the formation of ring structures have been predicted [58].

In the semiclassical regime, theoretical models face the challenge to account for atom-atom correlations in a strongly interacting Rydberg gas. Numerically solving the coupled equations for the many-body systems becomes demanding for a large number of atoms [23, 78, 79]. However, there exists several approximate theories for deriving the nonlinear susceptibility. One of them connects to the intuitive picture explained above. Here, the susceptibility $\chi$ of the medium can be related to the fraction $f_{bl}$ of blockaded atoms and follows the universal relation [82]

$$\frac{\mathrm{Im}\chi}{\mathrm{Im}\chi_{2\mathrm{lvl}}} = \frac{f_{bl}}{1+f_{bl}} \tag{3.7}$$

on two-photon resonance. This relation is supported by theoretical [82, 125] and experimental [62] investigations, but was also predicted to break down when collective effects in the many-body system become important [79]. Another approximate model connects a superatom description of the atomic medium with the two-photon correlation function inside the blockaded volume [124]. This model was able to explain measured EIT transmission spectra in the presence of Rydberg interactions as presented in ref. [23].

Moreover, also the mean-field and rate equation models introduced in the context of Rydberg-Rydberg interactions in Sec. 3.1.2 can be extended to incorporate the probe beam propagation in terms of a nonlinear susceptibility [64, 65, 78, 80]. In the following chapter, we comment on the details and the range of validity of two specific implementations of these models [64, 78]. Moreover, we compare them to experimental investigations of nonlinear absorption in Rydberg EIT spectra.

In Sec. 3.3 we present yet another model for the nonlinear susceptibility in the semiclassical regime [96, 121]. This one is based on a low intensity expansion in the probe field [58] and includes atomic interactions exactly up to second order. In contrast to previous studies, we explicitly include the dynamics of the intermediate state and find a resonantly enhanced nonlinear response of the Rydberg EIT medium as a consequence of a two-body, two-photon resonance [96, 121].

### 3.2.2 Quantum regime: Interactions between polaritons

In the quantum regime, the notion of dark-state polaritons, introduced in Sec. 2.2.2, provides a simple picture for the nonlinearity emerging from Rydberg interaction:

The Rydberg blockade effect prevents the formation of two polaritons at distances smaller than the blockade radius [24]. As polaritons comprise a photonic excitation, this results in effective photon-photon interactions [24, 57, 59, 70–73, 115, 124], as illustrated in Fig. 3.2(b).

Depending on the single-photon detuning, the polaritons either scatter of each other or acquire a phase shift [115]. On the one hand, the first effect can, for example, be exploited for producing non-classical states of light, such as anti-bunched light [24, 137] as well as two- and three-photon bound states [57, 71, 72]. Applications in this regime range from single-photon sources [137–139] and absorbers [140], to all-optical switches [74] and transistors [75, 76]. Moreover, microwave control of photon storage and interactions [141, 142] have been demonstrated. Going towards the many-body regime of interacting photons, Rydberg EIT at higher input photon rates [143] has been explored. On the other hand, the second effect of photons acquiring a phase shift, has been demonstrated to enable $\pi$-phase shifts needed for photonic gate applications [8, 10].

In the quantum regime, theoretical models face the challenge that strong atomic interactions not only induce atomic correlations, but also photon-photon and atom-photon correlations [77]. Models for systems restricted to a few photons [24, 57, 115] and to one dimension [6, 71, 118, 143–148] have been put forward successfully. For example, one approach considers the wavefunction of two photons at a distance $R$ [24, 57, 115]. In one dimension and in the dissipative regime, in turns out that the corresponding two-photon amplitude is governed by the effective potential [24, 77]

$$\mathcal{V}(R) = \frac{\mathrm{OD}_b}{1 - 2i(R/R_b)^6}\,, \tag{3.8}$$

whose range is given by the blockade radius $R_b$. Moreover, it crucially scales with the optical depth per blockade radius $\mathrm{OD}_b$.

Understanding the emerging photon-photon interactions in terms of Rydberg polaritons [26, 30] does not only provide an intuitive picture for Rydberg EIT, but also allows to advance theoretical models towards the many-body regime [149]. Other theoretical models in the many-body regime include a low-energy scattering theory [144], an effective field-theory [71, 145] and an input-output formalism [150].

Despite the difficulty in describing the Rydberg EIT system in the quantum regime, proposals for photon subtraction [151], a coherent polariton switch [117], novel types of photon interactions involving a spin or polariton exchange [152, 153], and the crystallization of photons [6, 149] provide fascinating prospects for the field of Rydberg EIT.

## 3.3 Blockade-induced enhancement of the nonlinear response

In three level systems, an adiabatic elimination of the intermediates states is a common approach to simplify the description of the system [58, 154]. Nevertheless, interesting atomic properties have been proposed if the detuning is smaller or comparable to the Rabi frequency of the control beam [79, 126, 127].

In my Master thesis [121] we have omitted an adiabatic elimination of the intermediate state and explicitly considered its dynamics in a ladder-type Rydberg EIT system, as depicted in Fig. 2.1. There, an enhanced nonlinear response has been found that emerges if the Rabi frequency of the control field equals the single-photon detuning. In the present section, we now develop an intuitive picture of the enhanced nonlinearity and find that it is a two-body, two-photon resonance which leads to the enhancement of the nonlinear response [96]. Moreover, we extend the parameter regime of the previous study [121], and analyze the spatial shape of the nonlinear susceptibility with the help of our intuitive picture.

In the following, we first introduce our intuitive picture in Sec. 3.3.1. Afterwards, we summarize in Sec. 3.3.2 the derivation of an analytic expression for the nonlinear susceptibility [121]. We present the emergence of the enhanced nonlinearity and analyze its spatial shape [96]. We comment on the scaling of the nonlinearity with important laser parameters and show that the resonance affects the propagation of the probe field [96, 121].

### 3.3.1 Intuitive picture in the dressed pair-state basis[9]

The enhanced nonlinear response of a Rydberg EIT medium, can be intuitively understood by examining the effect of atomic interactions on the energy levels in a pair-state model. In the following, we introduce this intuitive picture.

We consider an atomic cloud that is traversed by two counter-propagating probe and control fields, as illustrated in Fig. 3.3(a). The resulting Rydberg EIT system in ladder configuration has been discussed in Sec. 3.2, and the level scheme is shown in Fig. 2.1. The probe and control fields have Rabi frequencies $\omega$ and $\Omega$, respectively[10]. Moreover, we consider van der Waals interactions $V(R)$ between the atoms, which depend on the inter-atomic separation $R$.

For two interacting atoms, Fig. 3.3(b) shows the corresponding level scheme in the pair-state basis [126]. Starting with both atoms in the ground state $|gg\rangle$ either one or both atoms are excited to the intermediate state $|e\rangle$ or to the Rydberg state $|r\rangle$. Therefore, the level scheme can be subdivided into a singly- and doubly-excited subspace given by the states $\{|ge\rangle_+, |gr\rangle_+\}$ and $\{|ee\rangle, |er\rangle_+, |rr\rangle\}$, respectively. Here, $|ij\rangle_+ = (|ij\rangle + |ji\rangle)/\sqrt{2}$ with $i, j \in \{g, e, r\}$ denotes the respec-

[9] Adapted from Tebben *et al.* [96].

[10] In contrast to the discussion in Sec. 2.1, we introduce the frequencies $\omega = \Omega_p/2$ and $\Omega = \Omega_c/2$ for convenience. With these quantities the single-atom Hamiltonian on two-photon resonance ($\delta = 0$) in the basis of the single-atom states reads

$$\hat{\mathcal{H}} = \hbar \begin{pmatrix} 0 & \omega & 0 \\ \omega & -\Delta & \Omega \\ 0 & \Omega & 0 \end{pmatrix} .$$

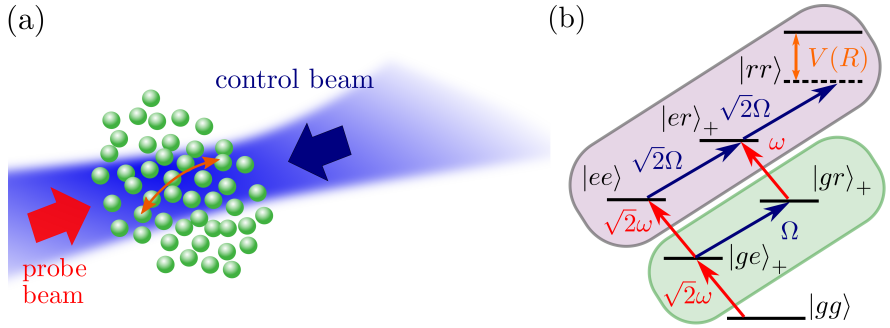


**Figure 3.3: Illustration of the Rydberg EIT system and pair-state basis.** (a) Counter-propagating probe and control beams result in EIT conditions for a strongly interacting Rydberg gas composed of three-level atoms (green spheres). (b) Level scheme of two interacting Rydberg atoms in the pair-state basis. It is subdivided into a singly- (doubly-) excited subspace indicated by the green (purple) shaded areas. Red (blue) arrows indicate transitions coupled by the probe (control) field. Resonant couplings are assumed for simplicity. For a detailed description and the notation see the main text. Figure (a) taken and adapted with permission from ref. [96]. Figure (b) adapted from ref. [126] with kind permission of T. Pohl. Copyrighted by the American Physical Society.

tive symmetric pair state [126]. The corresponding Hamiltonian [126]

$$\hat{\mathcal{H}} = \begin{pmatrix} 0 & \sqrt{2}\omega & 0 & 0 & 0 & 0 \\ \sqrt{2}\omega & -\Delta & \Omega & \sqrt{2}\omega & 0 & 0 \\ 0 & \Omega & 0 & 0 & \omega & 0 \\ 0 & \sqrt{2}\omega & 0 & -2\Delta & \sqrt{2}\Omega & 0 \\ 0 & 0 & \omega & \sqrt{2}\Omega & -\Delta & \sqrt{2}\Omega \\ 0 & 0 & 0 & 0 & \sqrt{2}\Omega & V(R) \end{pmatrix} \tag{3.9}$$

includes interactions between the two atoms as an effective level shift of the doubly-excited Rydberg state $|rr\rangle$. In the absence of interactions ($V(R) \to 0$) the system displays a linear EIT response to the probe field.

In order to learn about how interactions affect the two-body system, we investigate the spectrum of the Hamiltonian, Eq. (3.9), in the following. While transitions between the subspaces involve a probe photon, states within a subspace are coupled by the control field. As we assume $\Omega \gg \omega$, we simplify the system by diagonalizing the singly- and doubly-excited subsystems individually [126], which results in eigenstates $\{|\alpha\rangle_+, |\alpha\rangle_-\}$ and $\{|\beta\rangle_-, |\beta\rangle_+, |\beta\rangle_0\}$, respectively.

Fig. 3.4 shows the energy level diagram of the dressed states. For strong interactions ($V(R) \gg \Omega$) the eigenstate $|\beta_0\rangle \approx |rr\rangle$. Due to interactions this state is shifted far away in energy from the other eigenstates and thus can be neglected. On single-photon resonance ($\Delta = 0$) the remaining dressed eigenstates are equally distributed in energy around $E/\hbar = \omega_p$ and $E/\hbar = 2\omega_p$, where $\hbar\omega_p$ is the energy of one probe photon. However, for $\Delta = -\Omega$ the eigenstate $|\beta_-\rangle$ is resonantly coupled to the ground state $|gg\rangle$. As $|\beta_-\rangle$ contains a sizable fraction of the intermediate

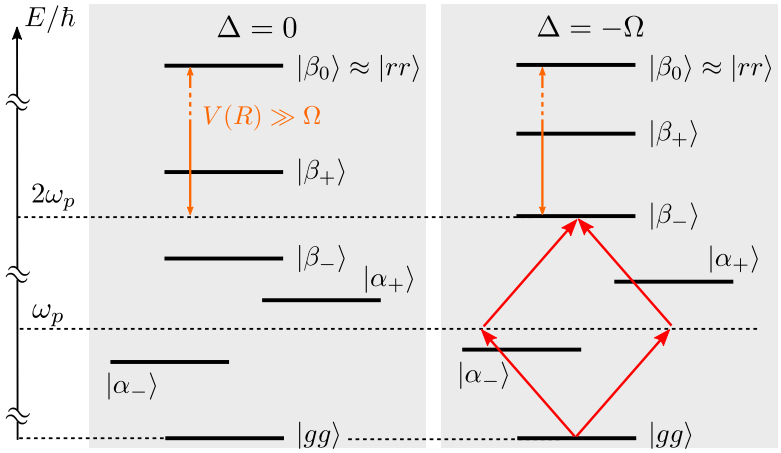


**Figure 3.4: Resonance in the dressed pair-state picture.** Energy level diagram of the laser-dressed pair-states for $\Delta = 0$ (left) and $\Delta = -\Omega$ (right), respectively. For $\Delta = \pm\Omega$ the eigenstate $\beta_\pm$ is resonantly coupled to the ground state $|gg\rangle$ by two probe photons (indicated by the red arrows). Figure taken and adapted with permission from [96].

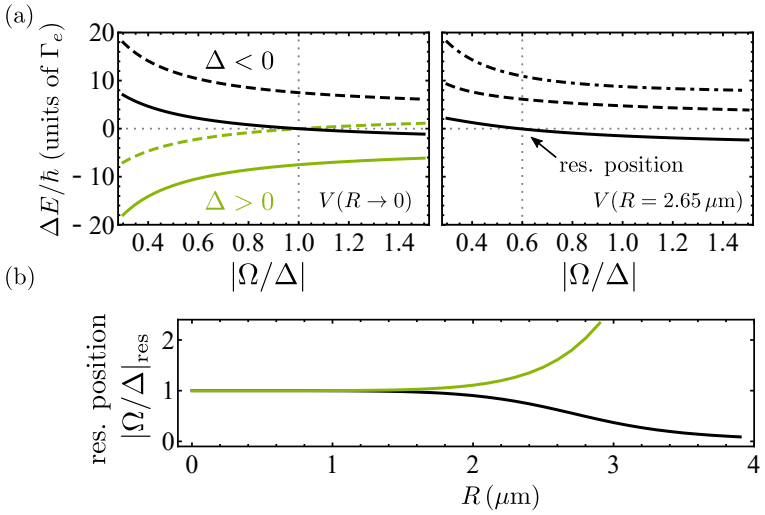


**Figure 3.5: Dependence of the dressed-state energies and the resonance position on the atomic interaction strength.** (a) Energy $\Delta E$ of the dressed levels $|\beta_-\rangle$ (solid line), $|\beta_+\rangle$ (dashed line) and $|\beta_0\rangle$ (dashed-dotted line) against the ratio $|\Omega/\Delta|$ for positive (green) and negative values (black) of $\Delta$, respectively. The situation $\Delta E = 0$ corresponds to the two-photon resonance with the ground state, which is met for infinite ($R \to 0$, left) and finite (right) interactions for different values of $|\Omega/\Delta|$. (b) Resonance position $|\Omega/\Delta|_{\text{res}}$ against the inter-atomic distance $R$ for positive (green) and negative (black) single-photon detunings. Figure and caption taken and adapted with permission from [96].

state, this leads to strong absorption of the probe field. Likewise, for $\Delta = +\Omega$ the state $|\beta_+\rangle$ moves into resonance and the same reasoning applies. It is this two-photon, two-body resonance that results in an enhanced nonlinear response of the atomic gas in the subsequently derived semiclassical model. This resonance has also been studied in the context of an enhanced atomic pair potential [79, 126, 127].

For finite interactions, the doubly excited Rydberg state $|rr\rangle$ can no longer be assumed to be decoupled from the remaining level scheme, and does affect the energy spectrum significantly. Fig. 3.5(a) shows the energy spectrum of the doubly excited subspace as a function of $|\Omega/\Delta|$ and with respect to the ground state energy $E_{|gg\rangle} = 0$. As shown in the left graph, for infinite interactions $V(R \to 0)$ the state $|\beta_\pm\rangle$ is on the two-photon resonance for $|\Omega/\Delta|$, where $\Delta E/\hbar = 0$, as discussed before. However, for finite interactions all eigenstates are reduced in energy and the state $|\beta_0\rangle$ appears in the spectrum. The right graph in Fig. 3.5(a) displays one example for $V(R = 2.64\,\mu\text{m})$ and $\Delta < 0$. As a consequence, the resonance appears at lower (higher) values of $|\Omega/\Delta|$ for negative (positive) single-photon detunings. Fig. 3.5(b) shows this dependence of the resonance position on the interaction strength explicitly for positive and negative single-photon detunings.

### 3.3.2 Enhanced nonlinear susceptibility[11]

In this section, we first summarize the derivation of an analytical expression for the nonlinear, nonlocal susceptibility that allows us to study the optical response for various interaction strengths, non-flat probe fields and nonconstant atomic density distributions. Details of the derivation can be found in refs. [96, 121]. Afterwards, we use the previously presented intuitive picture to explain the spatially-dependent refraction and absorption features of the nonlinear, nonlocal susceptibility. Finally, we discuss the scaling of the susceptibility with relevant laser parameters and its observable signature in the transmission spectrum of the probe field.

#### Perturbative solution of the Maxwell-Bloch equations

The derivation of the nonlinear susceptibility is based on the bosonic Maxwell-Bloch equations, Eq. (2.19), that we have introduced in Sec. 2.2.1. They accurately describe the non-interacting many-body system under weak-driving conditions. Accounting for atomic interaction and taking the expectation value for the probe field, the Maxwell-Bloch equations for the Rydberg-EIT system can be obtained and read [77, 121]

$$\partial_t \mathcal{E}(\mathbf{r}) = \left( ic\frac{\nabla_\perp^2}{2k_p} - c\partial_z \right) \mathcal{E}(\mathbf{r}) - ig\sqrt{\rho(\mathbf{r})}\hat{P}(\mathbf{r})\,, \tag{3.10}$$

$$\partial_t \hat{P}(\mathbf{r}) = -\,ig\sqrt{\rho(\mathbf{r})}\mathcal{E}(\mathbf{r}) - i\Omega(\mathbf{r})\hat{S}(\mathbf{r}) - \Gamma_p \hat{P}(\mathbf{r})\,, \tag{3.11}$$

$$\partial_t \hat{S}(\mathbf{r}) = -\,i\Omega(\mathbf{r})\hat{P}(\mathbf{r}) - \Gamma_s \hat{S}(\mathbf{r}) - i\int \mathrm{d}\mathbf{r}' V(\mathbf{r}-\mathbf{r}')\hat{S}^\dagger(\mathbf{r}')\hat{S}(\mathbf{r}')\hat{S}(\mathbf{r})\,, \tag{3.12}$$

[11] Taken verbatim from Tebben *et al.* [96] with some adaptions for the ease of readability.

where we have dropped the time-dependence of the field and operators for convenience.

Eqs. (3.10)-(3.12) have been solved in the semiclassical regime for $\Delta$ or $\Gamma_e \gg \Omega$ [58, 77], where the intermediate state dynamics can be eliminated. In these works, it has been shown, that the Rydberg EIT system exhibits a strong nonlinear and nonlocal response to the driving field. Motivated by this, we recast, in steady state, Eq. (3.10) into [121]

$$i\partial_z \mathcal{E}(\mathbf{r}) = -\frac{\nabla_\perp^2}{2k_p}\mathcal{E}(\mathbf{r}) + \chi^{(1)}(\mathbf{r})\mathcal{E}(\mathbf{r}) + \int \mathrm{d}\mathbf{r}'\chi^{(3)}(\mathbf{r}-\mathbf{r}')|\mathcal{E}(\mathbf{r}')|^2\mathcal{E}(\mathbf{r})\,, \tag{3.13}$$

where the linear $\chi^{(1)}(\mathbf{r})$ and nonlinear susceptibility $\chi^{(3)}(\mathbf{r}-\mathbf{r}')$ are directly related to the polarization coherence via

$$\langle \hat{P}(\mathbf{r})\rangle = \frac{c}{g\sqrt{\rho(\mathbf{r})}}\left[\chi^{(1)}(\mathbf{r})\mathcal{E}(\mathbf{r}) + \int \mathrm{d}\mathbf{r}'\chi^{(3)}(\mathbf{r}-\mathbf{r}')|\mathcal{E}(\mathbf{r}')|^2\mathcal{E}(\mathbf{r})\right]. \tag{3.14}$$

In Eq. (3.13), the two complex susceptibilities $\chi^{(1)}(\mathbf{r})$ and $\chi^{(3)}(\mathbf{r})$ act as an effective light potential responsible for refraction and absorption on the linear and nonlinear level, respectively.

For $\omega \ll \Omega$, we solve the Maxwell-Bloch equations by obtaining the expectation value of the polarization coherence with a perturbative expansion in the probe field. In zeroth order the probe field vanishes, such that all atoms remain in the ground state. Moreover, the second and all higher even orders vanish due to the centrosymmetry of the atomic gas. The first order provides the linear susceptibility [121]

$$\chi^{(1)}(\mathbf{r}) = -ig^2\frac{\Gamma_s}{c(\Omega^2+\Gamma_s\Gamma_p)}\rho(\mathbf{r})\,. \tag{3.15}$$

It recovers the well-known effect of EIT in the absence of atomic interactions and leads, for $\Gamma_s = 0$, to a full transmission of the probe field on two-photon resonance ($\delta = 0$).

Solving the third-order equations is more involved due to the appearance of correlations between Rydberg spin-wave excitations $\langle \hat{S}^\dagger(\mathbf{r}')\hat{S}(\mathbf{r}')\hat{S}(\mathbf{r})\rangle$. Ultimately, this leads to an infinite hierarchy of equations for the many-body system, which needs to be truncated appropriately. Here, the weak-probe assumption in combination with the blockade effect provides a natural way of truncating the hierarchy as it limits the density of Rydberg excitations in the system [77]. Therefore, the probability of finding two Rydberg excitations within a blockaded volume is small, and becomes negligible for three or more excitations. In this case, we can discard three-body interactions, and correlations of this and higher orders are fully suppressed [77]. This assumption does not only allow us to truncate the hierarchy of equations, but also implies that two-body atomic correlations are taken into account exactly.

After some calculations, which are presented in refs. [96, 121], we arrive at the third-order susceptibility [121]

$$\chi^{(3)}(\mathbf{r}-\mathbf{r}') = \frac{\Omega^4 g^4 \rho(\mathbf{r}')\rho(\mathbf{r})}{c|a|^2 a}\frac{2(\Gamma_s+\Gamma_p)V(\mathbf{r}-\mathbf{r}')}{2a(\Gamma_s+\Gamma_p)+i(a+\Gamma_p^2)V(\mathbf{r}-\mathbf{r}')}\,, \tag{3.16}$$

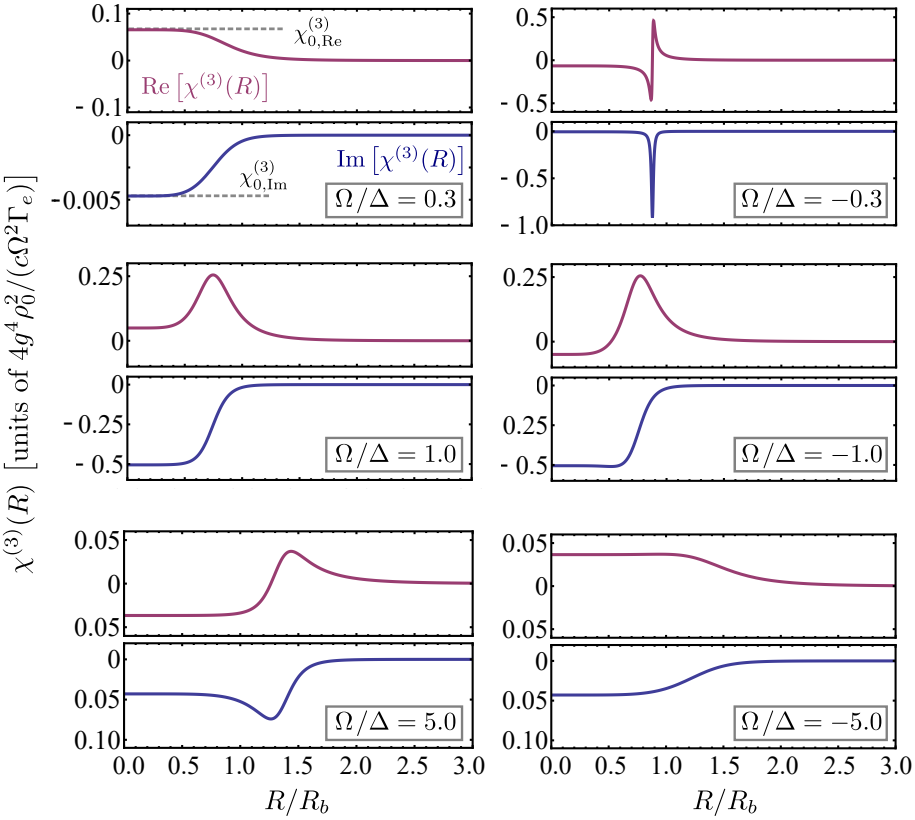


**Figure 3.6: Spatial shape of the nonlinear susceptibility.** Real (purple upper line) and imaginary part (blue lower line) of the nonlinear susceptibility $\chi^{(3)}(R)$ against the interparticle distance $R$ for various ratios $\Omega/\Delta$ (left column: $\Delta > 0$, right column: $\Delta < 0$). The susceptibility is scaled with a factor of $4g^4\rho_0^2/(c\Omega^2\Gamma_e)$. Plotted with $\Omega = 2.5\Gamma_e$ and $|48\mathrm{S}_{1/2}\rangle$ as the Rydberg state of $^{87}$Rb atoms for a constant atomic density distribution with $\rho_0 = 2 \times 10^{11}\,\mathrm{cm}^{-3}$. The blockade radii $R_b$ are $\{3.6, 2.9, 2.4\}\,\mu$m for $|\Omega/\Delta| = \{0.3, 1.0, 5\}$, respectively. Figure and caption taken and adapted with permission from [96].

where $a = \Omega^2 + \Gamma_s\Gamma_p$. Having obtained a result for the first- and third-order susceptibility, we arrive at a closed Eq. (3.13) for the propagation of the probe field through the highly nonlinear and nonlocal Rydberg EIT medium.

### Spatial shape of the nonlinear susceptibility

After having obtained an analytic expression for the nonlinear, nonlocal susceptibility in Eq. (3.16), we are in a position to investigate its spatially dependent absorption and refraction features, given by its imaginary and real part, respectively.

Fig. 3.6 displays typical shapes of the nonlinear susceptibility $\chi^{(3)}(R)$ as a function of the interatomic distance $R$ for a constant atomic density distribution $\rho(\mathbf{r}) = \rho_0$. For large values of $R$, the real and imaginary parts tend to zero for

all ratios $\Omega/\Delta$, reflecting the trivial non-interacting regime. In the case of $R \to 0$, the real and imaginary parts are constant for a large range of atomic distances $R$ with plateau values $\chi^{(3)}_{0,\mathrm{Re}}$ and $\chi^{(3)}_{0,\mathrm{Im}}$, respectively. For $\Omega = |\Delta|$ the latter gets maximal, meaning that the system displays the strongest nonlinear absorption.

For intermediate atomic distances $R$, the shapes of the real and imaginary parts strongly depend on the ratio $\Omega/\Delta$ and can display additional features. First, we examine the case for a positive single-photon detuning ($\Delta > 0$, left column). For $\Omega/\Delta < 1$, both the imaginary and real parts of the nonlinear susceptibility feature a soft-core shape. However, for $\Omega = \Delta$ the real part shows a strong maximum and for $\Omega > \Delta$ it features a sign-change where the imaginary part gets minimal at a finite distance. For $\Delta < 0$ (right column in Fig. 3.6) the situation is reversed, such that the minimum of the imaginary part at a finite distance appears for $\Omega < |\Delta|$. Moreover, it is more pronounced than for $\Delta > 0$.

The observed position of the additional features is a direct consequence of the van der Waals interactions and can be understood in terms of the energies of the dressed eigenstates in our intuitive picture. Examining Fig. 3.5(b), we see that for $\Delta > 0$ (green) the resonance condition is only met for absolute values of the ratio $\Omega/\Delta$ being larger than 1, while for $\Delta < 0$ (black) the opposite holds. This is exactly the reason, why we observe a minimum of the imaginary part of the nonlinear susceptibility for ratios $\Omega/\Delta$ larger (smaller) than 1 for positive (negative) single-photon detunings in Fig. 3.6. As a result, the ratio $\Omega/\Delta$ allows spatial shaping of the absorption and refraction properties of the nonlinear susceptibility.

### Scaling of the resonance

We now discuss the scaling properties of the resonance by looking at the susceptibility for $R \to 0$. Assuming $\Gamma_r = 0$ and $\rho(\mathbf{r}) = \rho_0$ for simplicity we obtain

$$\begin{aligned}\chi^{(3)}_{0,\mathrm{Re}} &= \frac{2g^4\rho_0^2}{c\Omega^2}\frac{\Delta\left(\bar{\gamma}_e^2 + \Delta^2 - \Omega^2\right)}{\bar{\gamma}_e^4 + \left(\Delta^2 - \Omega^2\right)^2 + 2\bar{\gamma}_e^2\left(\Delta^2 + \Omega^2\right)} \\ &\approx \frac{g^4\rho_0^2}{2c\Delta^3}, \qquad \text{for } \Omega = |\Delta|, \bar{\gamma}_e \ll |\Delta| \end{aligned} \tag{3.17}$$

for the real part and

$$\begin{aligned}\chi^{(3)}_{0,\mathrm{Im}} &= \frac{-2g^4\rho_0^2}{c\Omega^2}\frac{\bar{\gamma}_e\left(\bar{\gamma}_e^2 + \Delta^2 + \Omega^2\right)}{\bar{\gamma}_e^4 + \left(\Delta^2 - \Omega^2\right)^2 + 2\bar{\gamma}_e^2\left(\Delta^2 + \Omega^2\right)} \\ &\approx \frac{-g^4\rho_0^2}{c\bar{\gamma}_e\Delta^2}, \qquad \text{for } \Omega = |\Delta|, \bar{\gamma}_e \ll |\Delta| \end{aligned} \tag{3.18}$$

for the imaginary part, where $\bar{\gamma}_e = \Gamma_e/2$ has been introduced for convenience. Here, the second line in Eqs. (3.17) and (3.18) gives the value at the resonance condition $\Omega = |\Delta|$ in the nonadiabatic limit.

Fig. 3.7(a) displays the real and imaginary parts of $\chi^{(3)}_0$ as a function of the ratio $\Omega/\Delta$. Here, the imaginary part is resonantly enhanced for $\Omega = |\Delta|$, in agreement with the discussion of our intuitive picture in the pair-state basis in

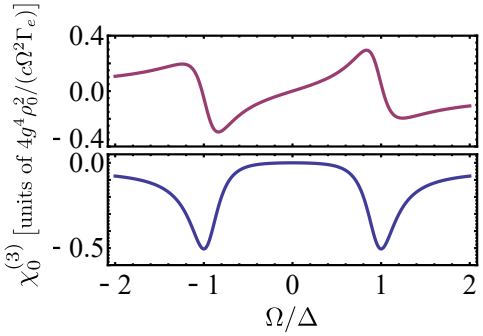


**Figure 3.7: Enhancement of the nonlinear susceptibility.** Real (purple, upper) and imaginary (blue, lower) parts of the nonlinear susceptibility $\chi_0^{(3)}$ for strong interactions ($V(R) \gg \Omega$) against the ratio $\Omega/\Delta$. At the resonance position ($\Omega = |\Delta|$) the real part features a sign change, while the imaginary part is resonantly enhanced. Plotted using $^{87}$Rb atoms with $|48S_{1/2}\rangle$ as the Rydberg state and $\Omega = 2.5\Gamma_e$. Figure and caption taken and adapted with permission from [96].

Sec. 3.3.1. The real part exhibits a sign change with a negative (positive) slope around $\Omega/\Delta = \pm 1$.

At the resonance condition $\Omega = |\Delta|$, the imaginary part interestingly depends on the intermediate state decay rate, while the real part does not. This allows us to increase the imaginary part independently by choosing an atomic species with a long-lived intermediate state.

### Signature of the resonance in the probe transmission

In this section, we investigate whether the two-body, two-photon resonance is experimentally accessible. For this purpose, we solve the propagation Eq. (3.13). Numerically, this can be done in a straightforward manner by exploiting a split-step Fourier propagation scheme [155, 156], as shown in my Master thesis [121] and in App. B.1.

However, for a better understanding, we derive an analytic solution of the propagation Eq. (3.13) under the assumption of a flat input field. Neglecting diffraction, this results in an effective one-dimensional equation [121]

$$\partial_z \mathcal{I}(z) = a_1 \mathcal{I}(z) + a_2 \mathcal{I}^2(z) \tag{3.19}$$

for the probe field intensity $\mathcal{I}(z) = |\mathcal{E}(z)|^2$, with [121]

$$a_1 = 2\mathrm{Im}\left\{\chi^{(1)}\right\}, \tag{3.20}$$

$$a_2 = 2\int \mathrm{d}\mathbf{r}' \mathrm{Im}\left\{\chi^{(3)}(\mathbf{r}-\mathbf{r}')\right\}. \tag{3.21}$$

Eq. (3.19) holds if the probe field intensity is approximately constant over the range of the nonlinear susceptibility (Fig. 3.6). This so-called local approximation

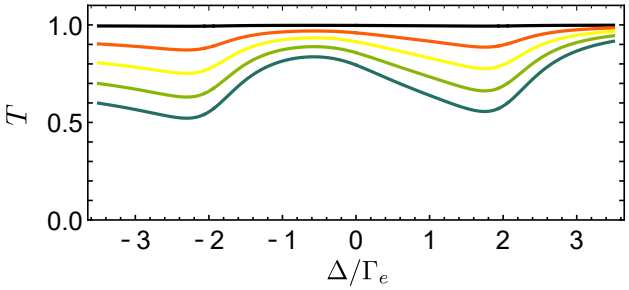


**Figure 3.8: Probe beam transmission in the presence of an enhanced nonlinear susceptibility.** Transmission $T = \mathcal{I}(L)/\mathcal{I}_0$ of the probe field after propagating a distance $L$ as a function of the single-photon detuning $\Delta$ for $\omega/\Omega = 0.008, 0.02, 0.04, 0.06, 0.08$ (black to blue, from top to bottom), respectively. In the nonlinear regime with high $\omega$, two transmission minima for $\Delta \approx \pm\Omega$ appear as a consequence of the two-body, two-photon resonance. Plotted for $\{\Omega, \delta, \rho_0, L\} = \{2\Gamma_e,\ 0,\ 1 \times 10^{11}\,\mathrm{cm}^{-3},\ 400\,\mu\mathrm{m}\}$ using Eq. (3.22). Figure and caption taken and adapted with permission from [96].

allows us to reduce the convolution integral in Eq. (3.13) to an integration solely over the susceptibility in Eq. (3.21). In addition, we assume in the simplest case a constant atomic density distribution. In this case only $V(\mathbf{r} - \mathbf{r}')$ is left to be position dependent.

A solution of Eq. (3.19) can be obtained readily and reads [121]

$$\begin{aligned}\mathcal{I}(z) &= \frac{a_1 \mathcal{I}_0 e^{a_1 z}}{a_1 + a_2 \mathcal{I}_0 - a_2 \mathcal{I}_0 e^{a_1 z}} \\ &\approx \mathcal{I}_0 e^{a_1 z} + \frac{a_2}{a_1} e^{a_1 z}(e^{a_1 z} - 1)\mathcal{I}_0^2 + \mathcal{O}(\mathcal{I}_0^3)\,, \end{aligned} \tag{3.22}$$

where the second line is an expansion for a small initial probe field intensity $\mathcal{I}_0 = \mathcal{I}(0)$. The first order describes an exponential reduction of the intensity, while the second contains the nonlinear absorption. Eq. (3.22) provides a leading-order nonlinear description of the probe field's propagation in the limit of a flat input field and a constant intensity distribution of the control field.

Fig. 3.8 shows a transmission spectrum of the probe field as a function of the single-photon detuning. In the non-interacting regime (small $\omega$), the transmission equals 1 for all values of the single-photon detuning $\Delta$, due to the EIT effect on two-photon resonance, where $\delta = 0$. Increasing the Rabi frequency of the probe field gradually, the interacting, nonlinear regime is reached. Here, two transmission minima occur as a consequence of the enhanced susceptibility at $\Delta \approx \pm\Omega$.

The overall shift of the spectrum towards negative values of $\Delta$ is a result of an integration over the nonlinear susceptibility in Eq. (3.21), as the shape of its imaginary part exhibits a minimum at a finite distance for a positive (negative) ratio $\Omega/\Delta$ above (below) 1, as shown in Fig. 3.6.

The distinct absorption features in the transmission spectrum allow us to access the resonance effect experimentally. The parameters in Fig. 3.8 indicate that

the two-body, two-photon resonance is experimentally accessible. However, for a realistic experimental situation a Gaussian atomic density distribution should be considered. This geometry is straightforward included in our theory [96, 121] and the resonance is still observable.

## 3.4 Summary and discussion

In this chapter we have studied the nonlinear optical response of an interacting Rydberg EIT medium from a theoretical perspective. Hereby, we have focused on the regime on two-photon resonance, where the ground state is resonantly coupled to the Rydberg state in a three-level scheme. Moreover, we have explicitly considered the dynamics of the intermediate state in our investigation. This allows us to study the nonadiabatic regime of Rydberg EIT, in which the single-photon detuning $\Delta$ is smaller than or comparable to the Rabi frequency $\Omega$ of the control field. It is in this regime, where an enhancement of the nonlinear response of a Rydberg EIT medium has been predicted for $\Delta = \Omega$ [121]. The semiclassical model, which describes this effect, has been summarized in the present section as it constitutes the starting point for our subsequent investigations. It provides an analytic expression for the associated third-order susceptibility and is applicable for various atomic density distributions and probe field geometries [121].

Here, we have extended this previous study [121] and significantly deepened the understanding of the enhancement. In particular, we have developed an intuitive picture for the enhanced nonlinear response that is based on laser-dressed interacting pair-states [96]. Analyzing the energy spectrum of this system, we have revealed that the enhancement results from a Rydberg blockade induced two-body, two-photon resonance. Moreover, in comparison to the previous study [121], we have extended the parameter regime to negative single-photon detunings. We have found that the resonance feature in the optical response emerges on both sides of the spectrum for $|\Delta| = \Omega$. Furthermore, we have shown that the spatial shape of the nonlinear response can be adjusting by the ratio $\Omega/\Delta$ [96]. Emerging features, such as soft-core shapes and local resonances, can be explained with the help of our intuitive model. Finally, we have shown that the transmission spectrum of the probe field displays an enhanced absorption around $\Delta = \pm\Omega$. We have explained a shift of the spectrum towards negative single photon detunings with the particular spatial shape of the nonlinear susceptibility [96].

The presented semiclassical model as well as the developed intuitive picture both assume low intensities of the probe field. Thus, they are only applicable if the Rabi frequency of the probe field is much smaller than the one of the control field. Moreover, the semiclassical model takes pair-wise interactions exactly into account, but neglects higher order correlations. In view of the results presented in the following chapter, it would be interesting to extend the theory to higher orders in the atomic correlations [97]. Here, the developed intuitive picture could aid in obtaining a first intuition by extending it to more than two atoms. Moreover, the derivation of the analytic formula for the nonlinear response of the medium, is based on the assumption that the control field is spatially constant [121]. However,

in experiments the available power for the control beam and thus also its maximal possible waist is typically limited. For a comparison to experimental results, it would thus be beneficial to find a possibility for including the geometry of the control field into the model in a future study.

In the nonadiabatic regime of Rydberg EIT with classical light fields, other effects have also been related to the two-body resonance described above. This includes an enhancement of the atomic pair potential, collective effects that lead to an enhanced Rydberg excited fraction, and a preservation of coherence as a consequence of suppressed photon scattering [79, 126, 127]. However, while these studies have focused[12] on atomic properties, our investigation provides a complementary approach by studying optical properties of the interacting Rydberg EIT medium as resulting from the resonance.

Finally, we want to note that also in the quantum regime of Rydberg EIT resonances have been discussed that relate to particular choices of the single-photon detuning and the Rabi frequency of the control beam. In this regard, we want to emphasize that the resonance, which we have covered in this chapter, differs from a so-called Raman resonance, which has been mentioned in ref. [115]. This Raman resonance is a one-body effect that emerges if the interaction-induced level shift plus the two-photon detuning equals $-\Omega_c^2/\Delta$. Depending on the sign of the van der Waals coefficient $C_6$, it manifests itself either for positive or negative single-photon detunings $\Delta$ only. An observed asymmetry in the dispersive part of the optical response with respect to $\Delta$ has been associated to this Raman resonance [8, 57]. In contrast, the resonance discussed in this chapter is a two-body effect and appears for both sides of the spectrum.

Still, also in the quantum regime a resonance feature has been proposed that connects to our two-body, two-photon resonance [77, 144]. Here, the possibility for repulsive photon-photon interactions has been shown to emerge as a consequence of a sign-change of the effective scattering potential for two polaritons at $|\Delta| = \Omega$ [144]. Our investigation complements this finding by examining this resonance effect from a semiclassical point of view [96].

In the following chapter, we compare the prediction provided by our semiclassical theory [96, 121] to measured transmission spectra of the probe beam on two-photon resonance.

[12] We remark that refs. [126, 127] solely addressed atomic properties, while ref. [79] briefly mentioned a connection of their work to the universal relation in Rydberg EIT systems.

CHAPTER 4

# Nonlinear absorption on two-photon resonance

*Parts of this chapter are based on the following publication, from which parts of the text have been taken verbatim*:

> **Nonlinear absorption in interacting Rydberg electromagnetically-induced-transparency spectra on two-photon resonance**
> A. Tebben, C. Hainaut, A. Salzinger, S. Geier, T. Franz, T. Pohl, M. Gärttner, G. Zürn and M. Weidemüller, Phys. Rev. A **103**, 063710 (2021)

As described in the previous chapter, Rydberg interactions render an atomic medium under EIT conditions strongly nonlinear and thus greatly affect the propagation of a classical light field. Spectral transmission properties of Rydberg EIT have so far been investigated with either the probe or the control beam on resonance [62, 64, 65, 84, 97]. Thereby, experimentally observed nonlinear effects included a reduction of the transmission on resonance as well as shifts and asymmetries of the spectrum. Different models have been proposed to explain these effects [58, 60, 64, 65, 78, 80, 82, 83, 96, 124]. While the reduction of the transmission is inherent in all these models, the occurrence of shifts and asymmetries is discussed [97]. This underlines the importance to find new experimental approaches for rigorously testing different theoretical models.

In the present chapter, we study features of Rydberg EIT transmission spectra [97]. We go beyond previous approaches by probing the spectrum not only along one detuning axis, but also by performing measurements where the applied fields are on two-photon resonance [97], as illustrated in Fig. 4.1. Staying on two-photon resonance, preserves EIT conditions and eliminates the linear response of the medium, as discussed in Sec. 2.1.3. Therefore, we can probe nonlinear absorption, resulting from interactions in the Rydberg EIT system, in the absence of linear EIT effects. As a consequence, our measurements constitute a rigorous method for testing existing models of Rydberg EIT in the semiclassical regime [97].

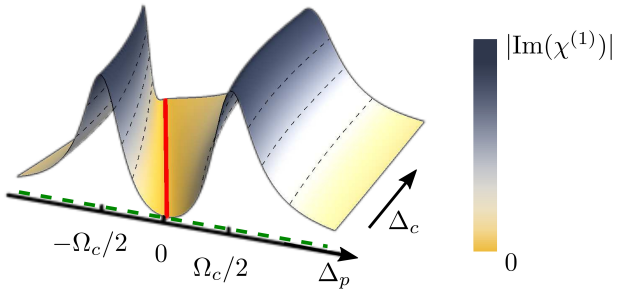


**Figure 4.1: Full spectral response of a linear EIT medium.** The imaginary part of the single-body optical response $|\mathrm{Im}(\chi^{(1)})|$ (color-coded and z-axis of the plot) of an atomic medium under EIT conditions is conventionally probed by changing the detuning $\Delta_p$ of the probe beam (green dashed line). However, staying on two-photon resonance $\delta = \Delta_p + \Delta_c = 0$ by simultaneously changing the detuning $\Delta_c$ of the control beam (red line), eliminates the linear response of the system. Figure taken and adapted with permission from [97].

This chapter is structured as follows: First, we introduce in Sec. 4.1 our experimental setup for Rydberg EIT experiments. It features state-of-the-art experimental techniques for obtaining strong atomic interactions while maintaining the coherence needed for EIT experiments. In Sec. 4.2 we study the dependence of dissipative and dispersive effects in EIT systems on the experimental geometry. This turns out to be particularly important for the case that pure dissipative effects are to be measured. We then present a careful characterization of the EIT system in the non-interacting regime in Sec. 4.3. Having laid the foundation for Rydberg EIT experiments, we present in Sec. 4.4 measurements of EIT transmission spectra in the presence of interactions. Here, we probe the spectrum with the control beam on resonance, and – following our new approach – on two-photon resonance. We compare in Sec. 4.5 our measurements [97] with the predictions based on a mean-field model [60, 64, 65, 80], a Monte-Carlo rate equation simulation [78, 81–83], and a low-intensity expansion [58, 96]. Finally, we summarize and discuss our results in Sec. 4.6.

## 4.1 Experimental realization of a Rydberg EIT medium

Investigating the nonlinear response of an atomic medium, which arises as a consequence of atomic interactions under EIT conditions, demands high atomic densities, high coherence properties of the system and strong atomic interactions. Therefore, an experimental setting featuring the following characteristics is required:

**(i) Cold and dense atomic cloud:** Atomic motion can lead to a Doppler broadened linewidth as well as dephasing, e.g. mediated by atomic collisions [157]. In order to avoid these effects, we require a temperature of the atomic cloud for which the Doppler shift and the collision rate are small

compared to the decay rate of the intermediate state.
The nonlinear response of the atomic medium scales quadratically with the peak atomic density, as shown in Sec. 3.3. Hence, high atomic densities are favorable. At the same time, the possibility for tuning the density without changing the geometry of the atomic cloud, turned out to be very valuable for a straightforward comparison of measured transmission spectra and theoretical predictions [121].

**(ii) Well-defined three-level system:** Isolation of a well-defined three-level system is a prerequisite for EIT experiments. Otherwise coupling or decay to levels outside the three-level systems can lead to unwanted multi-level systems. Therefore, preparation of a single hyperfine substate of the ground-state manifold is necessary.

**(iii) Rydberg EIT and detection methods:** In order to enable strong and long-range atomic interactions we choose the energetically highest level in a ladder-type EIT system to be a Rydberg state. This has several implications and results in the following two requirements: First, the ground- to Rydberg state coherence needs to be maintained [99]. This requires a Rydberg excitation scheme with a small linewidth. Second, Rydberg atoms feature large polarizabilities and are therefore susceptible for strong DC-Stark shifts, as described in Sec. 3.1. For example, the $|48S\rangle$ state used in this thesis possesses a polarizability of $\sim 40\,\mathrm{MHz/(V/cm)^2}$ [158]. This means that already for an electric field of about $0.8\,\mathrm{V/cm}$, the DC-Stark shift exceeds $100\Gamma_r$ [103, 129]. Here, $\Gamma_r/2\pi = 17.5\,\mathrm{kHz}$ is the lifetime of the Rydberg state given by the natural linewidth and black-body decay. Therefore, a precise control of electric fields is required.
Moreover, suitable detection methods are needed, which in the ideal case allow for simultaneous probing of optical as well as atomic properties of the medium.

In order to fulfill all these requirements, we use the experimental setup and sequence schematically shown in Fig. 4.2. First, we prepare a cold and dense atomic sample with a combination of different cooling stages in two magneto-optical traps (MOT), and subsequent confinement in an optical dipole trap. Details about all three traps and the preparation of our atom cloud can be found in Sec. 4.1.1. Afterwards, we prepare the atoms in a single sublevel of the ground-state manifold with a combination of optical pumping [159] and Landau Zener transfers [160] between hyperfine sublevels. The latter allows us to tune the atomic density, while preserving the shape of the atomic cloud. These two techniques are described in Sec. 4.1.2. Finally, we exploit a two-photon Rydberg excitation scheme with a small linewidth and compensate stray electric fields using specially designed electrodes [129]. Moreover, we use a combination of a transmission measurement and field ionization for the simultaneous detection of optical and atomic properties of the system. These techniques are described in Sec 4.1.3 and all together lay the foundation for our Rydberg EIT measurements.

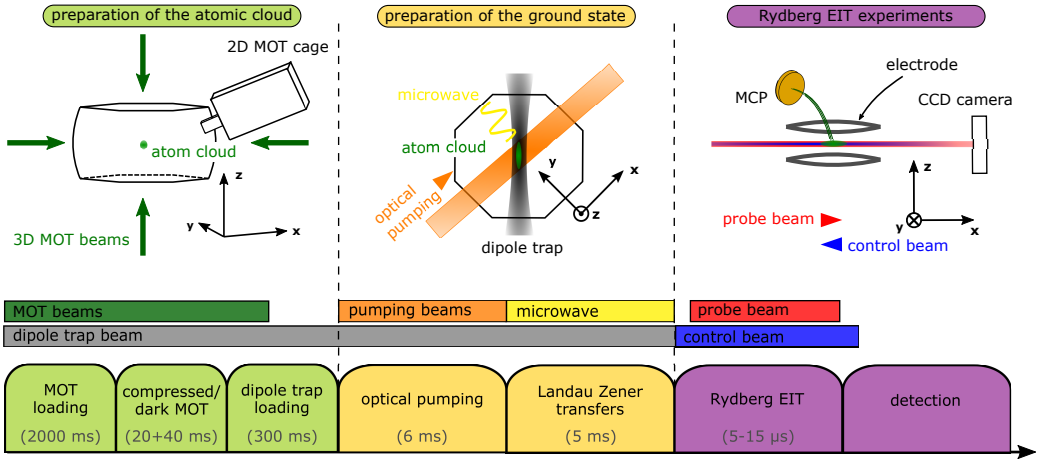


**Figure 4.2: Schematic experimental setup and sequence.** A cold and dense atomic sample is created using a combination of a 2D- and 3D-magneto-optical trap (MOT) and a dipole trap. Subsequent preparation of the atoms in a single hyperfine ground state by optical pumping and Landau Zener transfers provides the starting point for Rydberg EIT measurements. Vertical bars indicated, when the respective fields are turned on, while the lower row indicates the timing of the sequence. For details of the setup and sequence see the main text. Schematic illustrations of the setup adapted with permission from [121].

### 4.1.1 Preparation of a cold and dense atomic cloud

Our experimental setup, which is capable of obtaining an atomic cloud with temperatures as low as a few tenths of $\mu$K and peak atomic densities of up to $2 \times 10^{11}\,\mathrm{cm}^{-3}$, relies on highly developed cooling and trapping techniques, well-known in ultra-cold atom experiments [3, 161]. In particular, we make use of a 3D-MOT, loaded from a 2D-MOT [129, 162], and subsequent transfer and thermalization of the atomic cloud into an optical dipole trap. While the first two traps allow for efficient trapping and cooling of Rubidium atoms, the dipole trap ensures a tight confinement geometry and deterministic high peak-atomic densities.

The 2D- and 3D-MOT used in our experiment have been implemented, described and characterized in detail in previous work [103, 106, 129, 133, 163, 164] and recently in ref. [121]. The optical dipole trap has been redesigned and characterized in the course of my Master thesis [121]. In the following, the key aspects of these traps and the corresponding experimental sequence for the creation of a cold and dense atomic cloud are summarized. Thereby, we closely follow the discussion in refs. [103, 106, 121, 133, 163].

#### 2D-MOT

For an efficient loading of the 3D-MOT, a high flux of atoms with a mean velocity below the capture velocity of the 3D-MOT is required, which is typically in the order of 10 m/s [161, 163]. However, the mean velocity of atoms in a Rubidium

vapor provided by dispensers or a Rubidium oven is typically in the range of a few hundreds of m/s [161]. For this reason, it necessary to slow down the atoms. One option to decelerate the atoms is a so-called Zeeman slower, where the atoms are subject to a laser beam in the presence of a magnetic field gradient [3, 161]. However, this method does not provide cooling in transverse direction and puts strong constraints on the experimental geometry [163]. A 2D-MOT [129, 162] as a cold atom source allows to overcome these limitations. In our setup, a Rubidium background vapor is emitted by a dispenser and loaded into a 2D-MOT. Here, the atoms are cooled in two dimensions. An additional laser beam in the third dimension supports the atom beam to leave the 2D-MOT glass cell through a differential pumping stage. Separation of the glass cell from the main experimental chamber and careful alignment of the atom beam on the differential pumping stage ensures that mainly $^{87}$Rb atoms enter the main experimental chamber. Moreover, for good optical access the glass cell is connected to a view port of the main experimental chamber off-axis [129], as indicated in Fig. 4.2.

### 3D-MOT

Our 3D-MOT utilizes a combination of six laser beams for cooling the atoms in all three dimensions, as schematically illustrated in Fig 4.2. Cooling beams couple the $|5S_{1/2}, F = 2\rangle$ to $|5P_{3/2}, F = 3\rangle$ transition with a detuning of $\Delta_{\text{cooler}} \approx 3\Gamma_e$, as indicated in Fig. 4.3. Additional so-called repumping beams, which are resonant to the $|5S_{1/2}, F = 1\rangle$ to $|5P_{3/2}, F = 2\rangle$ transition, close the cooling cycle. Magnetic field coils in anti-Helmholtz configuration are located below and above the main experimental chamber [133]. The position of zero magnetic field can be fine-tuned with the help of additional pairs of magnetic field coils, so-called compensation coils. They are attached to the chamber viewports on all three axes. The pair of compensation coils in $x$-direction is furthermore used to apply a magnetic offset field of 30 G during the EIT sequence described subsequently. A micro-controller based interlock system prevents the coils from overheating.

After loading the 3D-MOT from the 2D-MOT (see Fig. 4.2), we apply a compressed MOT phase [165] and a dark-MOT phase [166]. These sequences allow us to increase the peak atomic density, and to reduce the temperature and size of the atomic cloud for optimal loading into the dipole trap. The timing and ramps of these two phases are optimized for an efficient loading into the optical dipole trap [121]. At the end of the MOT sequence the atoms populate the hyperfine state $|5S_{1/2}, F = 1\rangle$ [129].

### Optical dipole trap

In order to achieve a tight confinement of the atomic cloud and high atomic densities, we load the atoms into an optical dipole trap. Such traps rely on a light-induced shift of the ground state to trap neutral atoms, where the resulting trapping potential is proportional to the laser intensity [168]. For a red detuned trapping beam, the atoms are confined in the region with highest intensity. In principle, one tightly focused laser beam is sufficient for the creation of an optical

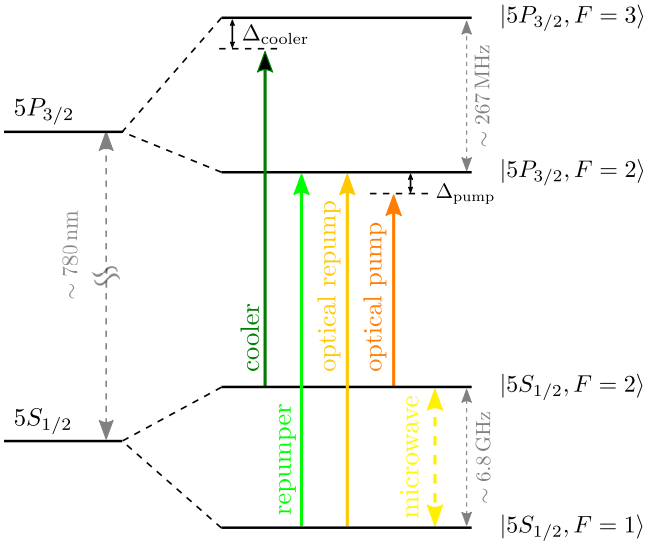


**Figure 4.3: Schematic level scheme for cooling and ground-state preparation of $^{87}$Rb atoms.** Shown are the relevant hyperfine levels of $^{87}$Rb. Transitions driven by external fields are indicated by arrows. So-called cooler and repumper beams (green) are used for the creation of a 3D-MOT. Optical pump and repump beams (orange) provide the basis for an optical pumping stage, while a microwave field (yellow) is used for Landau-Zener passages. See main the text for details of the techniques and ref. [167] for details of the Rubidium level scheme.

dipole potential. However, the confinement in axial direction in such a potential is rather small due to the smaller intensity gradient. In order to achieve larger axial confinement, we use a so-called crossed optical dipole trap [169, 170]. In this configuration, the dipole trap beam is retro-reflected into the chamber and crosses the atomic cloud a second time under an angle of approximately 9° [121]. The dipole trap has an angle of 45° with respect to the main propagation axis $x$ through the experimental chamber, as indicated in Fig. 4.2.

The waist of the laser beam was optimized for a compromise between a trap size and trap depth that allow for an efficient loading from the 3D-MOT, and the maximally possible size in propagation direction of the EIT laser beams [121]. The latter is needed to achieve a strong optical response of the system. For an efficient loading of the dipole trap, the dipole trap beam is already turned on at the beginning of the experimental sequence. After the MOT lasers and the magnetic field gradient are turned off, we allow for a time of 300 ms for thermalization, as schematically shown in Fig 4.2. With this experimental sequence we obtain an atomic cloud with $1/e^2$-waists of approximately $40 \times 40 \times 300\,\mu\text{m}^3$ [97].

### 4.1.2 Ground-state preparation

After having obtained a cold and dense atomic cloud, the next requirement for Rydberg EIT experiments is the preparation of the atoms in a ground state, as

defined by a single hyperfine level of the ground-state manifold. For this purpose, we use a combination of optical pumping [159] and two Landau-Zener transfers [160] to efficiently populate the ground state $|5S_{1/2}, F = 2, m_F = 2\rangle$, as also reported in a Master thesis of our group [171]. The details of these techniques are presented in the following.

### Optical pumping

After loading the dipole trap, the atoms populate all $m_F$ states of the hyperfine manifold $|5S_{1/2}, F = 1\rangle$. In order to transfer the atoms to the targeted ground-state level, we use two right-circular polarized laser beams that propagate along the $x$-axis of the experimental chamber (see Fig. 4.2 for the coordinate system) in the presence of a 2 G magnetic field. The first laser beam (optical repump beam, see Fig. 4.3) with a power of 200 $\mu$W addresses the atoms and transfers them to the $|5P_{3/2}, F = 2\rangle$ manifold. From there the atoms can either decay back into the initial state or to the intended $|5S_{1/2}, F = 2\rangle$ manifold. The second laser beam (optical pumping beam) couples the $|5S_{1/2}, F = 2\rangle$ to $|5P_{3/2}, F = 2\rangle$ transition with a power of $\sim 2.1\,\mu$W and a detuning of about $-7$ MHz with respect to the clock-transition. After a time of 6 ms, most of the atoms have cycled to the targeted ground state $|5S_{1/2}, F = 2, m_F = 2\rangle$, which is a dark state for the optical pumping scheme in our setup.

### Landau-Zener passages

We remove residual atoms in $m_F$ sublevels other than the targeted ground-state level in the following way: First, we transfer the atoms to the $|5S_{1/2}, F = 1, m_F = 1\rangle$ state. Afterwards, we remove residual atoms in the $|5S_{1/2}, F = 2\rangle$ manifold by application of a resonant laser pulse. Finally, the other atoms are transferred back into the desired ground-state level. With this procedure we end up with 95% of the atoms being in the ground state $|5S_{1/2}, F = 2, m_F = 2\rangle$.

The atom transfer is achieved by utilizing a so-called Landau-Zener passage [160]. This technique enables a coherent transfer of atoms between two states $|1\rangle$ and $|2\rangle$, as illustrated schematically in the inset of Fig. 4.4. For this purpose, the detuning $\Delta(t)$ between the two states is varied linearly in time. In this way, the desired state is reached via an adiabatic transfer that involves the instantaneous eigenstates of the two-level system. In our case a microwave field couples the ground state $|5S_{1/2}, F = 2, m_F = 2\rangle$ to the state $|5S_{1/2}, F = 1, m_F = 1\rangle$, as depicted in Fig. 4.3. The microwave field is produced by a 6.8 GHz microwave generator [171] and emitted by a small antenna inside the vacuum chamber, as indicated in Fig. 4.2. Ramping its frequency $\omega_{\mathrm{mw}}$ from a value far below to a value far above the resonance frequency of the transition in the presence of a 2 G magnetic field, realizes the state transfer. The probability of a successful transfer between the two states

$$P_{\mathrm{LZ}} = 1 - \exp\left(-\frac{\Omega_{\mathrm{mw}}^2}{\Delta\omega_{\mathrm{mw}}/t_{\mathrm{mw}}}\right) \tag{4.1}$$

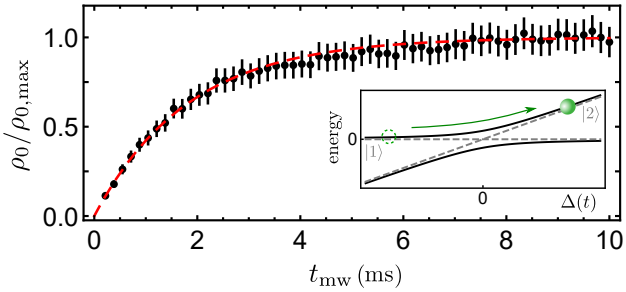


**Figure 4.4: Atomic density tuning using a Landau-Zener transfer.** Measured scaled peak atomic density $\rho_0/\rho_{0,\max}$ against the duration $t_{\rm mw}$ of the microwave pulse. The density $\rho_{0,\max}$ is achieved after a full Landau-Zener transfer at large $t_{\rm mw}$. Error bars indicate shot-to-shot fluctuations of the atomic density of $\pm 8\%$. The red dashed line is a fit of the Landau-Zener formula, Eq. (4.1), to the data. From the fit we extract a microwave Rabi frequency $\Omega_{\rm mw}/2\pi$ of $(5.3 \pm 0.6)$ kHz. The inset illustrates schematically the Landau-Zener transfer between two quantum states $|1\rangle$ and $|2\rangle$, where solid (dashed) lines depict the eigenstates (bar states) of the two-level system. $\Delta(t)$ is the time-dependent detuning between the two states.

is determined by the Rabi frequency $\Omega_{\rm mw}$ of the microwave and the total change $\Delta\omega_{\rm mw}$ of the microwave frequency [160, 172]. In our case $\Delta\omega_{\rm mw}/2\pi = 320\,$kHz [171]. Furthermore, $t_{\rm mw}$ denotes the duration of the microwave pulse. The dependence on $t_{\rm mw}$ allows us to tune the atomic density. For this purpose, we vary the duration of the microwave pulse in the first of the two Landau-Zener passages, which we use for removing residual atoms in other than the desired ground state. A measurement of the peak atomic density $\rho_0$ as a function of the microwave duration $t_{\rm mw}$ is depicted in Fig. 4.4. In contrast to other methods of tuning the atomic density, e.g. by a free ballistic expansion of the cloud, this procedure has the advantage that the geometry of the atomic cloud remains unchanged.

### 4.1.3 Rydberg EIT and detection methods

After having prepared the atoms in a single ground-state sublevel, the EIT sequence and a subsequent combined detection of optical and atomic properties of the system follow, as indicated in Fig. 4.2. The three-level EIT scheme in ladder configuration, with the energetically highest level being a Rydberg state, as well as the detection methods, given by transmission and field-ionization measurements, have been implemented and characterized in previous works [103, 106, 121, 129, 133, 173, 174]. Closely following these works, the main aspects of the level scheme and of the detection methods are summarized in the following.

#### Rydberg EIT level system

Starting with the atoms in the ground state $|g\rangle = |5S_{1/2}, F = 2, m_F = 2\rangle$, we realize a Rydberg EIT system with an intermediate state $|e\rangle = |5P_{3/2}, F = 3, m_F = 3\rangle$, and a metastable Rydberg state $|r\rangle = |48S_{1/2}, m_j = 1/2\rangle$, as shown in Fig. 4.5(a).

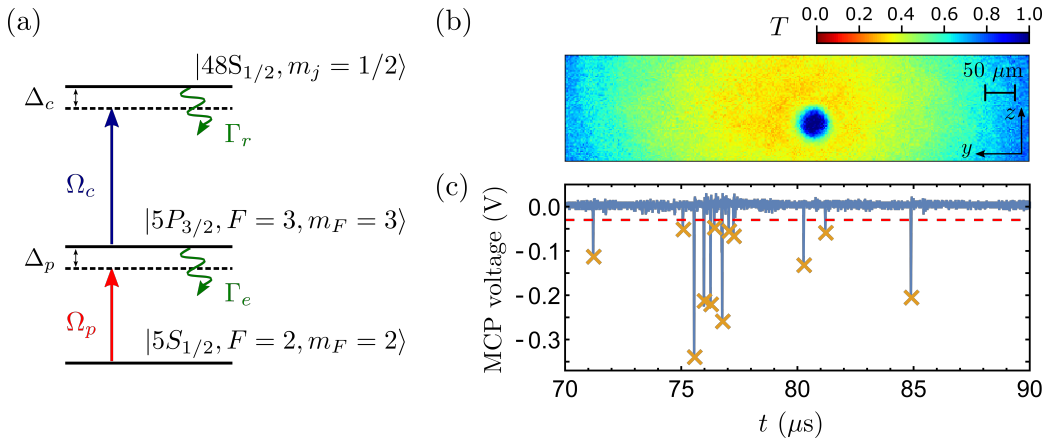


**Figure 4.5: Level scheme for Rydberg EIT and detection methods.** (a) Three-level scheme for Rydberg EIT with $^{87}$Rb atoms coupled by probe and control beams with Rabi frequencies $\Omega_p$ and $\Omega_c$, respectively. See the main text for a detailed description. (b) Typical image of the EIT transmission $T$ of the probe beam measured with the technique of absorption imaging. (c) Example for an ion trace after field ionization. Shown is the measured MCP voltage against the arrival time $t$ of the ions on the MCP. Voltage peaks below a certain threshold (red dashed line), which are marked with a cross, are ion counts. Layout of the figure as in ref. [133].

The intermediate state is short-lived with population decay rate $\Gamma_e/2\pi = 6.07\,\mathrm{MHz}$ [167]. The Rydberg state has a population decay rate $\Gamma_r/2\pi = 17.5\,\mathrm{kHz}$ given by natural and black-body decay. A probe beam with wavelength $\lambda_p = 780\,\mathrm{nm}$ and Rabi frequency $\Omega_p$ couples the ground state $|g\rangle$ to the intermediate state $|e\rangle$. A control beam with a wavelength $\lambda_c = 480\,\mathrm{nm}$ and Rabi frequency $\Omega_c$ couples the intermediate state $|e\rangle$ to Rydberg state $|r\rangle$. These laser beams are counter-propagating along the $x$-axis of the experimental chamber, which makes Doppler shifts negligible. Moreover, they cross the atomic cloud under an angle of 45°, as shown in Fig. 4.2. While the control beam is focused onto the atom cloud and has a $1/e^2$-waist of 20 to 32 $\mu$m, the probe beam has a collimated beam waist of 3 mm. In Sec. 4.2 we present a modification of this setup to a geometry, where the probe beam has a smaller waist than the control beam.

In order to ensure the isolation of a well-defined three-level system, the probe (control) beam is right-(left-) circular polarized with respect to an applied magnetic offset field of 30 G, which points along the $x$-axis. Moreover, the probe and control beams are frequency stabilized using the Pound-Drever-Hall looking technique [175] with a high finesse Fabry-Pérot cavity. The cavity has been implemented and characterized in [176]. Using direct-digital-synthesis (DDS) sources, the detuning of both lasers can be adjusted independently over a range of several hundreds of MHz. The maximally achievable detuning is limited by half of the free-spectral range of the cavity, which is 1.5 GHz in our setup [121].

The EIT sequence typically involves a probe beam exposure time of 5-15 $\mu$s. For the probe intensities used here, the exposure time is small enough to avoid

an avalanche creation of Rydberg ions [121, 177]. In addition, the control beam is switched on 2 $\mu$s before the probe beam to ensure a preparation of the EIT dark state [99] (see also Sec. 4.3). After the EIT sequence, the system is probed with the help of the detection methods that are described in the following.

### Transmission measurement

With the purpose of measuring EIT transmission spectra, we use an Andor iXon Ultra 897 EM-CCD camera to record the probe light that is transmitted through the atomic cloud, as indicated in Fig. 4.2. A $4f$-imaging system with a resolution of 5 $\mu$m results in an effective pixel size that corresponds to 2.1 $\mu$m in the imaging plane at the atom position [173]. The transmission $T(y,z)$ of the probe field is defined as [121]

$$T(y,z) = \frac{n_{c,\mathrm{abs}}(y,z) - n_{c,\mathrm{bg}}(y,z)}{n_{c,\mathrm{ref}}(y,z) - n_{c,\mathrm{bg}}(y,z)}\,. \tag{4.2}$$

Here, the so-called absorption image $n_{c,\mathrm{abs}}(y,z)$ in the presence of the atoms, the reference image $n_{c,\mathrm{ref}}(y,z)$ without atoms, and the background image $n_{c,\mathrm{bg}}(y,z)$ without atoms and without the probe beam are given by the number of counts $n_c(y,z)$ on the CCD camera sensor. For each transmission measurement, these images are taken within one experimental cycle. An example transmission image under EIT conditions is shown in Fig. 4.5(b).

Besides the probe beam transmission, we can also infer the geometry of the atomic cloud and the Rabi frequency of the probe beam from the measured images, as explained in the following. The optical depth $\mathrm{OD}(y,z)$ of the medium can be obtained from the transmission $T(y,z)$, Eq. (4.2), as [121]

$$\mathrm{OD}(y,z) = -\ln\left[T(y,z)\right] = \sigma_{\mathrm{abs},0}\int_{-\infty}^{\infty}\rho(x,y,z)\,\mathrm{d}x\,. \tag{4.3}$$

Here, $\sigma_{\mathrm{abs},0} = 2.907\times10^{-9}\,\mathrm{cm}^2$ is the resonant cross section for the $^{87}$Rb $D_2$ line ($5S_{1/2}\rightarrow 5P_{3/2}$) [167] in the weak probe limit ($\Omega_p \ll \Gamma_e$), and $\rho(x,y,z)$ denotes the atomic density. The second equality follows from Lambert-Beers law under the assumption that the probe beam intensity is much smaller than the saturation intensity of the transition. By assuming that the atomic density distribution is Gaussian in all spatial dimensions, atomic properties such as the peak optical depth, the peak atomic density $\rho_0 = \rho(0,0,0)$, and the size of the atomic cloud can be inferred from the OD image by fitting a 2D Gaussian function. We determine that the cigar-shaped atomic cloud has $1/e^2$-waists of about $40\times40\times400\,\mu\mathrm{m}^3$ [97]. Moreover, with a time-of-flight measurement we record a temperature of the atomic cloud of approximately 100 $\mu$K [97].

Finally, the Rabi frequency of the probe beam can be directly determined from the reference image $n_{c,\mathrm{ref}}$ in each experimental cycle. The intensity in each pixel [121]

$$I_{\mathrm{px}}(y,z) = \frac{hc/\lambda_p n_{c,\mathrm{ref}}(y,z)}{q t_{\mathrm{exp}} A_{\mathrm{px}}^2} \tag{4.4}$$

is given by the pixel area $A_{\mathrm{px}}$, the exposure time $t_{\mathrm{exp}}$ and the photon detection efficiency $q$. As outlined App. A.1, we have measured $q$ to be $0.47\pm0.02$. Using

Eq. (2.5), the Rabi frequency can be calculated from Eq. (4.4) for each pixel. In the following sections we have always determined the probe Rabi frequency in this way.

#### Field ionization for Rydberg atom detection

Besides the measurement of the probe beam transmission, our setup also features a simultaneous detection of Rydberg excitations present in the medium. Atoms in the Rydberg state are ionized by application of a strong electric field [46, 129]. Afterwards, the resulting ions guided with the help of specially designed ring electrodes [129] onto a micro-channel plate (MCP), as indicated in Fig. 4.2. An example of a time-dependent ion trace, measured with an oscilloscope with 1 GHz temporal resolution, is shown in Fig. 4.5(c). The efficiency of our ion detection can be determined by using depletion imaging [178] and is approximately 0.10 ions per Rydberg excitation [179]. Moreover, we measure $0.743 \pm 0.096$ ion counts in the absence of the control beam, where no Rydberg excitations and thus no ions can be created [97]. This gives a lower bound for the number of detectable Rydberg excitations.

In addition to field ionization, the ring electrodes also serve for the compensation of stray electric fields. For this purpose, the ion signal is recorded as a function of the applied electrode voltage and of the control Rabi frequency for each axes of the experimental chamber. Symmetrization of these so-called DC-Stark maps yields the electrode voltages for which residual electric fields are minimized at the atom position [174].

## 4.2 Minimizing dispersive effects in EIT transmission spectra

The transmission of a probe beam through a Rydberg EIT medium is affected by dissipative and dispersive effects induced by the atomic cloud. Both effects strongly depend on the particular geometry of the experimental system. For example, Han *et al.* [180] pointed out that the EIT region can act as a gradient index lens in a geometry, where the control beam is focused onto the atomic cloud within a uniform probe beam. As a consequence, dispersive effects dominate the spatial structure of recorded transmission images.

The experimental setup that has been used in previous studies of our group consisted of a probe beam with a collimated $1/e^2$-beam waist of 3 mm, which illuminates the atomic cloud uniformly. Moreover, a control beam with a $1/e^2$-beam waist between $20-32\,\mu$m is focused into the atomic cloud. Therefore, lensing effects as the one mentioned above are expected. However, we seek to investigate the dissipative part of the nonlinear susceptibility and thus aim at canceling the dispersive one. This would enable an unambiguous observation of pure nonlinear absorptive effects in Rydberg EIT. In this section we describe the realization of an experimental setup that minimizes dispersion. Here, a probe beam that is focused onto the atomic cloud with a waist smaller than the one of the control beam is utilized.

For this purpose, we first review in Sec. 4.2.1 the spatial structure of EIT transmission images that have been recorded with the experimental setup previously used in our group. Following the work of ref. [180], we study the role of the dissipative and dispersive part of the susceptibility of the atomic medium and compare our measurements to a numerical simulation of the probe beam propagation. This discussion emphasizes the need for a different experimental geometry. In Sec. 4.2.2, we provide some relevant details on the implementation of a focused probe beam in our setup, which has a waist smaller than the one of the control beam. A detailed characterization of the implemented probe beam can be found in App. A.2. Finally, we present in Sec. 4.2.3 that the new experimental geometry leads to an EIT transmission measurement, which displays minimized dispersive effects. This experimental geometry serves as a starting point for the investigation of nonlinear absorption in the subsequent sections.

### 4.2.1 Effect of dissipation and dispersion on EIT transmission

As explained in Sec. 2.1 the optical response of a medium is determined by its susceptibility. While the imaginary part of the susceptibility $\chi$ is immediately connected to dissipation, the real part is linked to dispersive effects [102]. The latter are characterized by a refractive index $n$. For weakly absorbing media this quantity can be approximated as [102]

$$n \approx \sqrt{1 + \mathrm{Re}[\chi]}\,. \tag{4.5}$$

If the susceptibility is position-dependent, absorption and the refractive index also become spatially dependent and strongly vary according to the geometry of the experimental setup. As a consequence, the atomic medium may act as a gradient index lens due to the geometry of the laser beams [180]. In the following, we show that the experimental setup so far used in our group leads to strong lensing effects.

We emphasize that these effects, including especially the structure of transmission images and spectral features of the probe beam transmission, have already been investigated in detail in ref. [180]. Here, we discuss the results of ref. [180] in the context of our experimental situation for two purposes: First, we want to emphasize the need for a new experimental geometry that minimizes dispersive effects, as introduced in the subsequent Sec. 4.2.2. Second, we want to convey an understanding of lensing effects in order to motivate the particular choice we have made for the new experimental geometry.

We begin by presenting a transmission measurement, where a collimated probe beam illuminates the atomic cloud uniformly, while the control beam is focused onto the atoms, as schematically shown in Fig. 4.6(a). The transmission spectrum, evaluated in the center of the control beam displays, typical Autler-Townes minima shown in Fig. 4.6(b). Moreover, an asymmetry in the spectrum, and a transmission larger than unity around a probe beam detuning $\Delta_p/2\pi$ of $-2\,\mathrm{MHz}$ are apparent. From the position of the minimum at positive[13] detunings we extract a Rabi

[13] We have found with the numerical simulations presented subsequently, that the minimum position at positive detunings does not change in the presence of lensing effects for the considered situation.

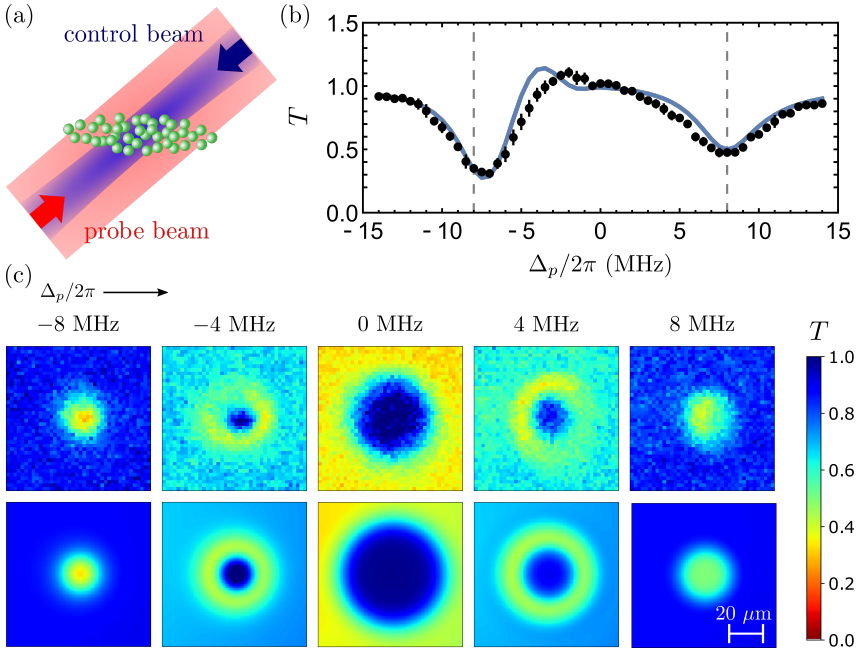


**Figure 4.6: Spatial structure of EIT transmission images.** (a) Experimental geometry (not to scale) for an EIT transmission measurement of a collimated probe beam (red, 3 mm $1/e^2$-waist) in the presence of a focused control beam (blue, $20 - 32\,\mu$m $1/e^2$-waist) on resonance ($\Delta_c = 0$). (b) Measured transmission $T$ in the center of the control beam as a function of the probe beam detuning $\Delta_p$ (black points). Vertical dashed lines indicate $\Delta_p = \Omega_c/2$ with $\Omega_c/2\pi = (16.0 \pm 0.1)$ MHz. (c) Spatial structure of the measured transmission images for different probe beam detunings $\Delta_p/2\pi$ as given above the panels (upper row). The result of a numerical simulation, as explained in the main text, is shown as a blue solid line in (b) and in the lower row of (c). Other parameters are the Rabi frequencies $\Omega_c/2\pi = (16.0 \pm 0.1)$ MHz and $\Omega_p/2\pi = (0.59 \pm 0.01)$ MHz of the control and probe beam, respectively, and a peak atomic density of $(0.007 \pm 0.001)\,\mu\text{m}^{-3}$. Figure (a) adapted with permission from [97].

frequency of $2\pi \times (16.0 \pm 0.1)$ MHz for the control beam. Here, the error results from the uncertainty in the estimation of the minimum position.

The 2D transmission images recorded with the CCD camera feature a complex spatial structure, which are shown as a function of the detuning $\Delta_p$ of the probe beam in the upper row of Fig. 4.6(c)[14]. On resonance a large, almost flat-top transparency region is visible. In contrast, for $\pm\Omega_c/4 = \pm 4$ MHz a ring-like structure arises, where absorption is enhanced. The radius of the ring is larger for positive than for negative detunings. Around the transmission minima at $\pm\Omega_c/2 = \pm 8$ MHz the ring structure vanishes. Again, the structure is larger for

[14] A transmission image of the whole atomic cloud is for example shown in Fig. 4.5(b). Here, we restrict the region-of-interested to the region, where the control beam traverses the atomic cloud.

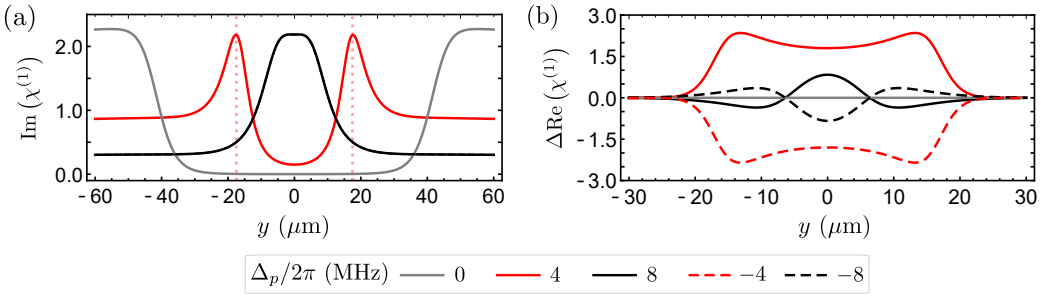


**Figure 4.7: Cross sections of the spatially dependent linear susceptibility.** (a) Calculated imaginary part of the linear susceptibility $\mathrm{Im}(\chi^{(1)})$ as a function of position $y$ transversal to the propagation direction of the laser beams (see Fig. 4.2 for the coordinate system) for different probe beam detunings $\Delta_p$. Red dotted lines indicate the position where $\tilde{\Omega}_c(y)/2 = \pm\Delta_p$. Curves for $-4$ and $-8$ MHz detuning fall on top of the respective curves for positive detunings. (b) Difference of the real part of the susceptibility $\Delta\mathrm{Re}(\chi^{(1)}) = \mathrm{Re}(\chi^{(1)}) - \mathrm{Re}(\chi^{(1)}_{\Omega_c=0})$ as a function of position $y$ for different probe beam detunings. Here, $\mathrm{Re}(\chi^{(1)}_{\Omega_c=0})$ is the susceptibility in the absence of the control beam corresponding to the one of a two-level system. Parameters are the same as for the measurement presented in Fig. 4.6.

positive detunings.

### Relation of the transmission images to the spatially dependent susceptibility

In order to get a deeper insight into the complex spatial structure of the EIT transmission images, we plot in Fig. 4.7 the position-dependent real- and imaginary part of the linear susceptibility, Eq. (2.12). Due to the Gaussian beam profile of the laser, we assume that the Rabi frequency of the control beam varies[15] as $\tilde{\Omega}_c(y) = \Omega_c \exp(-y^2/w_c^2)$ transversal to the propagation direction. Here, $w_c$ is the $1/e^2$-waist and $\Omega_c$ the peak Rabi frequency of the control beam. In general, the susceptibility varies within the limits of a three-level EIT system, as present in the center of the control beam, to the one of a two-level system, as obtained outside the control beam area with $\tilde{\Omega}_c(y) = 0$.

The imaginary part of the susceptibility, displayed in Fig. 4.7(a), is zero for a resonant probe beam for a large spatial range. Outside of the area of the control beam, the susceptibility levels off to the one of a two-level system. While two local maxima are apparent for an intermediate probe beam detuning of $\pm 4$ MHz, only a single one is visible for a detuning of $\pm 8$ MHz. The imaginary part of the susceptibility can be related to the absorption of the probe beam. For zero detuning, the vanishing imaginary part of the susceptibility results in the observed flat-top region of full transmission [180], as shown in Fig. 4.6(c). Moreover, the

[15] The Rayleigh range of our control beam is about 3 mm. This is large compared to the extent of the atomic cloud in propagation direction. Thus, the size of the beam in transversal direction is approximately constant over the length of the atom cloud. Therefore, the control beam can be described by assuming a constant phase and beam size in propagation direction.

local maxima shown in Fig. 4.7(a) for a probe beam detuning of ±4 MHz are the origin for the observed enhanced absorption. Due to the rotational symmetric structure of the control beam, the absorption feature becomes ring-like in the transmission images. The position of this enhanced absorption, indicated by red dashed lines in Fig. 4.7(a), corresponds to "local" Autler-Townes resonances within the control beam where $\tilde{\Omega}_c(y)/2 = \pm\Delta_p$ [180]. With increasing detuning, the radius of the ring becomes smaller. Around the Autler-Townes minima at a probe beam detuning of ±8 MHz the ring collapses into a single absorption peak.

The gradient of the real part of the susceptibility defines the resulting refractive index gradient [180]. In our experimental setup, the steepest change of the susceptibility is determined by the spatially dependent control beam. Again, the susceptibility levels off to the one of a two-level system outside the control beam, where $\tilde{\Omega}_c(y) = 0$. In order to highlight the spatial change of the susceptibility, we subtract the real part of the susceptibility of the full three-level system $\mathrm{Re}(\chi^{(1)})$ by $\mathrm{Re}(\chi^{(1)}_{\Omega_c=0})$, corresponding to the one in the absence of the control beam. The spatial dependence of the difference $\Delta\mathrm{Re}(\chi^{(1)})$ of these susceptibilities is shown in Fig. 4.7(b). For a resonant probe beam, the real part vanishes for all positions, meaning that no dispersive effects are expected. However, if the detuning of the probe beam is non-zero, a complex structure of the spatially dependent susceptibility is apparent. For $\Delta_p/2\pi = +4$ MHz, the difference $\Delta\mathrm{Re}(\chi^{(1)})$ is larger than zero in the central part of the control beam. According to Eq. (4.5), this leads to a refractive index that is larger in the inner part of the beam [121]. For positive detunings this results in a defocusing effect [180]. For a negative probe detuning of −4 MHz, the opposite is the case reversed leading to a focusing effect [180]. As a consequence, the absorption ring in Fig. 4.6(c) is not symmetric around zero detuning, but is slightly larger for a positive detuning [180]. Also, the observed transmission above unity for a probe beam detuning of about −2 MHz in Fig. 4.6(b) can be understood as a consequence of this focusing effect. The spatial dependence of the real part of the susceptibility for $\Delta_p/2\pi = \pm 8$ MHz shows a more complex structure, but a similar lensing effect depending on the slope of the real part emerges. Here, it leads on the negative detuning side to an increased probe beam intensity in the center of the control beam [180]. As a consequence, absorption in Fig. 4.6(b) is overestimated. The situation is again reversed for the positive detuning, which explains the asymmetry of the transmission spectrum.

#### Determination of the control beam waist from the transmission images

As explained before, the ring-like structures in the transmission images result from "local" Autler-Townes resonance [180], where the radius of the ring depends on the geometry of the control beam. Knowing the peak Rabi frequency of the control beam, it is therefore possible to extract the waist of the control beam from these images. In the absence of dispersion, the radii of the rings should be equal for positive and negative detunings. However, the previously described lensing effect results in an asymmetry of the ring radii as a function of the probe beam detuning. In order to determine the waist of the control beam, we therefore extract the radius of the absorption rings for detunings $1.5\,\mathrm{MHz} \leq |\Delta_p|/2\pi \leq 6\,\mathrm{MHz}$ and take the

mean value for each pair of positive and negative detunings at values of $\pm\Delta_p$. Using the Rabi frequency of the control beam as estimated from the positions of the Autler-Townes minima, we obtain a waist[16] of $(20.0 \pm 0.5)\,\mu$m.

### Comparison of recorded transmission images and numerical simulations

In order to investigate the combined effect of dissipation and dispersion on EIT transmission images from a theoretical perspective, we numerically simulate the probe beam propagation[17]. Details of the simulation can be found in App. B. We want to note, that a simulation of the full setup, including the atomic cloud and the subsequent imaging system, is complicated by the vastly different length scales present in our experimental setup. For example, while the waists of probe and control beams are of the order of tenths of micrometer, the CCD camera is located at a distance of about 760 mm [173] from the atoms. In order to circumvent this issue, the simulations presented in this section are based on the two following assumptions: First, we assume that the imaging system exhibits negligible optical aberrations. This allows us to discard the imaging system and evaluate the transmission images of the probe beam directly in the object plane, which is in the center of the cloud. Moreover, since the optical depth of the atomic medium is low, we assume that absorption depends linearly on the atomic density. In this way, it is possible to obtain the level of transmission after a complete propagation through the atomic cloud, by doubling the experimentally applied atomic density in the simulation. We further explain this approach, in App. B.

We use the experimental parameters, the three-dimensional geometry of the atomic cloud, and a waist of the control beam of $w_c = 21\,\mu$m as an input for the simulation. From the simulation we obtain the transmission spectrum and images shown in Fig. 4.6(b) and (c), respectively. Our numerical simulation results show a reasonable agreement with the main features of the measured spectrum and transmission images. In order to obtain a better agreement with the measurement, a dephasing $\gamma_{gr}/2\pi = 1\,$MHz was chosen for the simulation. In our measurement we cannot completely ascertain the absence of interactions, which could explain the need for this rather high dephasing rate. In particular, such a dephasing decreases the transmission where it exceeds unity in the spectrum. Moreover, this dephasing does not influence the radii of the absorption rings. However, most importantly it reduces the size of the transmission feature in the image at zero probe beam detuning. Our numerical simulations have shown that the size of the transmission feature at a detuning of $\Delta_p = 0$ actually strongly depends on the dephasing rate $\gamma_{gr}$. Therefore, in the complete absence of atomic interactions, the size of the transmission feature at zero detuning would give a very sensible probe for the dephasing rate $\gamma_{gr}$.

[16] This estimation is inconsistent with the expected waist of the control beam due to the measured beam intensity, which is approximately $32\,\mu$m. However, this inconsistency does not affect the main measurements of this chapter presented in Sec. 4.4, as we always infer the Rabi frequency of the control beam unambiguously from a measurement of the Autler-Townes splitting.

[17] We note that numerical simulations of transmission spectra in the presence of lensing effects are also presented and discussed in ref. [180].

Finally, we note that the measured transmission images for $\pm 4\,\mathrm{MHz}$ show a slight asymmetry in the intensity distribution within the ring structure. This could hint towards possible aberrations of our imaging system. As these are not taken into account in the simulation, they might be the cause of remaining deviations between the measurement and simulation results.

#### Summary

As a summary, dissipative and dispersive effects in EIT strongly depend on the geometry of the experiment [180]. So far, our group has used a geometry where the control beam is embedded in a uniform probe beam. However, in this case absorption ring structures manifest themselves in the transmission images, and lensing effects obscure an unambiguous measurement of EIT transmission spectra [180]. We have observed these lensing effects, as presented in this section. However, aiming at investigating nonlinear absorption in Rydberg EIT, dispersive effects should be minimized. Therefore, we have inverted the geometry by implementing a probe beam with a waist smaller than the one of the control beam, as outlined in the following sections.

### 4.2.2 Implementation of a probe beam with a waist smaller than the control beam

In the limit $\Omega_p \ll \Omega_c$, the EIT susceptibility, Eq. (2.12), is independent of the Rabi frequency $\Omega_p$ of the probe beam. Especially, this is also true for the real part of the susceptibility, which determines dispersive effects. Therefore, spatial variations of the probe beam within a uniform control beam do not cause a gradient in the index of refraction, and thus no lensing effects. Nevertheless, the maximal waist of the control beam is limited by the requirement of a high Rabi frequency $\Omega_c$ as needed for our subsequent measurements. In order to minimize dispersive effects, the probe beam should thus be focused onto the atoms with a waist smaller than the waist of the control beam.

We have implemented such a geometry into the experimental setup. The focused probe beam is provided by the same laser as the collimated probe beam. It passes a separate AOM in double-pass configuration for fast switching and reaches the experimental optics table via a polarization maintaining fiber. A 50 mm achromatic lens collimates the beam to a $1/e^2$-waist of approximately 3.8 mm. Two lenses of focal length $f = 150\,\mathrm{mm}$ focus the beam onto the atoms, resulting in a waist of about $15\,\mu\mathrm{m}$ at the position of the atoms. The optical setup and an image of the beam are shown in Fig. 4.8.

The two lenses used for focusing the probe beam are not used in the conventional way of a telescope. Instead, the distances between the two lenses as well as between the last lens and the position of the atoms are larger than $2f$ and $f$, respectively. This is a consequence of the restricted space on the experimental optics table. The focused probe beam has to traverse the vacuum chamber on the same axis as the collimated probe beam in order to be counter-propagating to the control beam and for reaching the CCD camera. In addition, a high numerical aperture

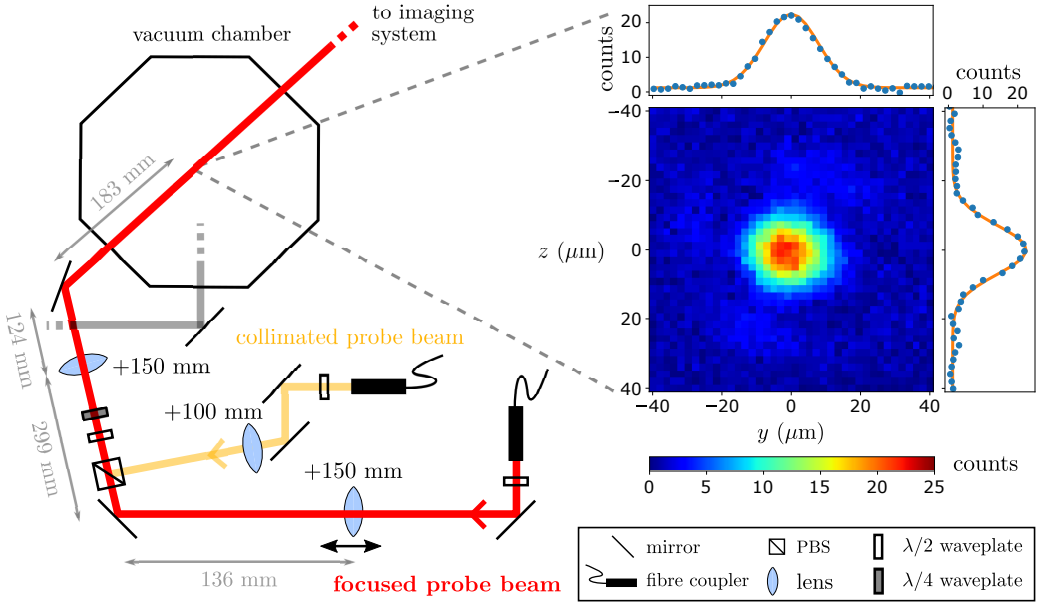


**Figure 4.8: Optical setup and image of the focused probe beam.** The optical setup (not to scale) of the focused probe beam (left, red line) mainly consists of two lenses with focal length +150 mm. An additional lens with focal length +100 mm in the collimated probe beam path (light orange) compensates the focusing lens for the focused probe beam. A polarizing beam splitter (PBS) is used to combine the two beam paths, while $\lambda/2$ and $\lambda/4$ waveplates ensure a right-circular polarization. The path of the dipole trap beam is indicated in gray. An image of the focused probe beam measured with the CCD camera is shown on the right. From a 2D Gaussian fit of the image we obtain Gaussian $1/e^2$-waists of $(15.6 \pm 0.1)\,\mu$m and $(14.1 \pm 0.1)\,\mu$m in $y$- and $z$-direction respectively. The fit is indicated by orange lines in the 1D-cuts of the image, which are taken along the center of the beam. Schematic drawing on the left with permission taken and adapted from ref. [121].

is needed for a small spot size in the focal plane. This is achieved if the lens that focuses the beam onto the atoms has the minimal working distance possible. Without affecting the collimated probe beam path and due to spatial constraints on the optics table, a lens with a focal length of 1000 mm would be needed for this purpose. Such a setup was tested, but proved to be too unstable. Therefore, we decided to put the last focusing lens into the beam path, where the focused and the collimated probe beam already overlap, as indicated schematically in Fig. 4.8. The closest position of this lens to the vacuum chamber is restricted by the dipole trap beam, indicated as a gray line in the drawing. Aiming at a waist of about 15 $\mu$m at the position of the atoms, we have chosen the pair of lenses mentioned above as the optimal solution. Finally, we have implemented an additional +100 mm lens into the collimated probe beam path, in order to compensate for the focusing +150 mm lens. This ensures the collimation of the beam, but decreases its size by a factor of 1.5 to a waist of $\sim 2$ mm.

A detailed characterization of the probe beam in terms of the beam profile and

its positional stability can be found in App. A.2. We have observed that short- and long-term drifts of the center position are below 3 $\mu$m and thus insignificant for the subsequent measurements. Moreover, a small ring structure around the beam is faintly visible in Fig. 4.8. At higher ratios of $\Omega_p/\Omega_c$ spurious Rydberg excitations (see ref. [143] and App. C) might be created in the ring structure. After excitation transport [67, 181, 182] they could affect the probe beam transmission in the center of the beam. Therefore, we have analyzed the ring structure in detail, as presented in App. A.2, and find that the ring structure does not affect measurements at small ratios $\Omega_p/\Omega_c$.

As the probe beam is tightly focused onto the atoms, the beam power needs to be as low as 0.5 nW to obtain Rabi frequencies as low as $2\pi \times 0.5$ MHz. Therefore, we use natural density filters with an optical density of about 7 to attenuate the beam. Moreover, we use a home-build AOM driver for switching the beam. With a rise time of about 50 ns it provides an almost squared pulse shape.

### 4.2.3 Transmission measurement with minimized dispersion

Next, we characterize dissipative and dispersive effects in our new experimental geometry that is shown schematically in Fig. 4.9(a). For this purpose, we measure on the one hand the transmission $T$ of the probe beam in the center of the control beam. On the other hand, we extract the waist of the probe beam from the transmission images by using a two-dimensional Gaussian fit. As we are interested in changes of the beam waist due to dispersive effects, we calculate its relative change with respect to the measured beam waist $w_{p,0}$ in the absence of the atoms. The resulting transmission $T$ and relative beam waist $\Delta w_p$ as a function of the probe beam detuning are displayed in Fig. 4.9(b).

The transmission spectrum shows the expected Autler-Townes minima and does not exhibit an asymmetry or a transmission above unity. The relative beam waist $\Delta w_p$ shows an almost symmetric structure around zero detuning with two zero-crossings for the waist in $y$- and $z$-direction, respectively. Moreover, $|\Delta w_p| \lesssim 0.14$ is apparent.

We compare in Fig. 4.9 the experimental results with a numerical simulation of the probe beam propagation through the atomic cloud and a reduced imaging system (see App. B for details). We want to emphasize that this simulation is based on fewer assumptions than the one for the collimated beam presented in Sec. 4.2.1.

First, we simulate a dispersion free geometry[18], meaning in particular a control beam waist $w_c \to \infty$. We find that the simulated transmission spectrum agrees with the measured data, as can be seen from the gray dashed line in Fig. 4.9(b). Moreover, the relative difference of the beam waist $\Delta w_p$ turns out to be zero for

[18] Since the susceptibility depends on the atomic density, dispersive effects may also arise from a gradient due to the geometry of the atomic cloud. In order to avoid this, we choose an atomic density distribution, which is constant in transversal and Gaussian in propagation direction. This geometry is only used for the dispersion free simulation. For all other simulations, we consider a three-dimensional atomic cloud as in the experiment. We note that dispersive effects due to the geometry of the atomic cloud are much smaller than dispersion arising from the geometry of the control beam.

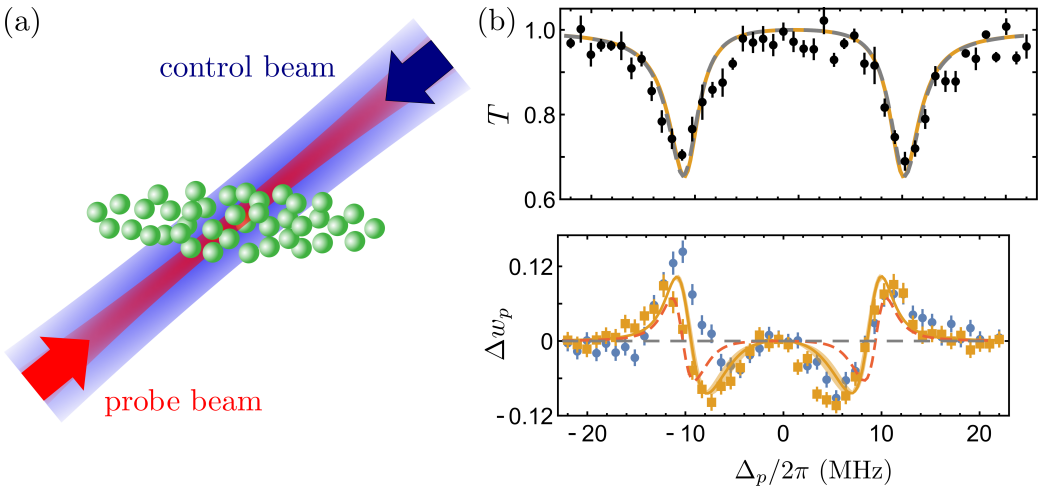


**Figure 4.9: Transmission and dispersion measurement utilizing the focused probe beam.** (a) Schematic illustration of the new experimental geometry, where the probe beam has a smaller waist than the control beam (not to scale). (b) Measured transmission $T$ of the probe beam (black points, upper graph) and relative difference of the beam waist $\Delta w_p = [w_p(\Delta_p) - w_{p,0}]/w_{p,0}$ in $y$- (orange squares, lower graph) and $z$- (blue points, lower graph) direction as a function of the probe beam detuning $\Delta_p$. The orange solid lines are the result of a numerical simulation with a waist of the control beam of $w_c = 20\,\mu$m (the orange shaded area accounts for a variation of the beam waist of $\pm 2\,\mu$m). The red dashed line depicts the result for $w_c = 32\,\mu$m. Gray dashed lines indicate the result for a dispersion free geometry (see the main text for details). Other parameters are the Rabi frequencies $\Omega_c/2\pi = (21.4 \pm 0.2)$ MHz and $\Omega_p/2\pi = (0.93 \pm 0.02)$ MHz of the control and probe beam, respectively, and a peak atomic density of $(0.022 \pm 0.001)\,\mu\text{m}^{-3}$. Figure (a) taken with permission from [97].

all probe beam detunings. This is expected as the control beam Rabi frequency is position independent, such that no dispersive effects and thus no change of the probe beam waist are possible. However, no change in the beam waist, as predicted from this simulation, does not agree with the measurement results for the relative beam waist $\Delta w_p$, as presented in Fig. 4.9(b). Instead, for a blue beam waist of $20\,\mu$m, both the simulated transmission spectrum and the simulated relative change $\Delta w_p$ of the beam waist agree well with the data. This shows in combination with the result for an infinitely large control beam, that a small dispersive effect is still apparent for the implemented geometry. Nevertheless, even though the beam waist is affected by dispersion, the experimentally and numerically obtained transmission spectra do not show the typical features of a dispersion dominated spectrum. In particular, they do not exhibit a transmission above 1 or an asymmetry. Moreover, the two simulated transmission spectra for an infinite and a finite waist agree with each other. Therefore, we conclude that dispersive effects are clearly minimized compared to the geometry as used previously in our group (see Sec. 4.2.1), and that dispersion has a negligible effect

on the transmission spectrum for the parameters of this measurement.

Since the EIT susceptibility, Eq. (2.12), scales linearly with the atomic density, we expect dispersive effects to become more pronounced at higher atomic densities. Nevertheless, using the same simulation as above, but now with a density[19] of $0.16\,\mu\mathrm{m}^{-3}$, we have found that the transmission spectra for an infinite and finite waist of the control beam still agree with each other. Moreover, the measured spectrum at high density and at a small ratio $\Omega_p/\Omega_c$ of the Rabi frequencies (see Fig. 4.14), displays no asymmetry or a transmission larger than 1. Both aspects again underline, that dispersive effects even at higher atomic densities are minimized.

On two-photon resonance, the linear response of the atomic medium, and thus also linear dispersion resulting from the geometry of the Gaussian beams vanish in the ideal case. Still, dispersion from the nonlinear part of the susceptibility might arise. We find experimentally[20] that the relative change in the beam waist $|\Delta w_p| \leq 0.11$. Based on the findings presented above, this could indicate that dispersive effects do not affect the transmission measurement significantly.

Finally, we want to note that varying the control beam waist in the simulation by $\pm 2\,\mu\mathrm{m}$, shown as shaded orange area in Fig. 4.9(b), gives very similar results. This means that this measurement is not a very precise method to determine the waist of the control beam. However, the result for a beam waist of $32\,\mu\mathrm{m}$ (red dashed line), which we would expect[21] from an intensity measurement of the control beam and the observed Autler-Townes splitting, is clearly distinguishable due to the measured structure around zero probe beam detuning.

All the experiments presented in the following have been carried out with the geometry introduced in this section. In particular, they have been performed with a probe beam with a waist smaller than the one of the control beam. The collimated probe beam is only used for determining the size, peak optical depth, and temperature of the atomic cloud in the absence of the control beam, as explained in the previous section.

## 4.3 Characterization of the EIT system in the non-interacting limit

Now, we proceed with a characterization of our experimental system in the non-interacting EIT limit. In this regime Rydberg-Rydberg interactions are negligible due to low atomic densities or small ratios $\Omega_p/\Omega_c$ of the Rabi frequencies. Dephasing present in the system can diminish the coherence needed for EIT [99].

[19] This is the atomic density used in the measurements presented in Chap. 4. For comparability, we also adapted the other parameters in the simulation to match those given in Fig. 4.16.

[20] In the subsequent sections of this chapter, we find that the experimentally observed dissipative effects are not captured by the theoretical models, which we use for comparison. Therefore, we lack a suitable model for the nonlinear susceptibility, on which we could base a simulation.

[21] This inconsistency has also been observed in the measurements with the collimated probe beam. However, it does not affect the subsequent measurements as we always infer the Rabi frequency of the control beam unambiguously from Autler-Townes measurements.

Therefore, we first measure in Secs. 4.3.1 and 4.3.2 the dephasing rates $\gamma_{ge}$ and $\gamma_{gr}$ of the two- and three-level system, respectively. Afterwards, we comment in Sec. 4.3.3 on the adiabatic preparation of the EIT-dark state. We proceed with the characterization of our EIT system by measuring an Autler-Townes spectrum in the non-interacting regime, as presented in Sec. 4.3.4. Finally, we summarize the main characteristics of our EIT system in Sec. 4.3.5.

### 4.3.1 Dephasing in the two-level system

In the following, we consider the two-level system, composed of the ground state $|g\rangle$ and the intermediate state $|e\rangle$, as shown in Fig. 4.5(a). The dephasing rate $\gamma_{ge}$ can be determined from a measurement of the spectral response of this two-level system. In general, the spectral response of a two-level system is determined by the natural lifetime of the involved states [157]. In our case the ground state does not decay. Thus, the natural linewidth of the transitions is given by the population decay rate $\Gamma_e$ of the intermediate state. However, certain mechanisms can lead to a broadening or even a slight reduction of the power broadened linewidth. In the following, we list the most common ones in cold atom experiments:

(i) **power broadening:** Driving the two-level system with a laser intensity that is comparable to or larger than the saturation intensity of the transition results in broadening of the Lorentzian lineshape [109].

(ii) **homogeneous broadening due to decoherence:** Mechanisms such as laser frequency fluctuations or rescattering of photons can lead to decoherence, which effectively increases the dephasing rate $\gamma_{ge}$ of the two-level system [106, 107, 183].

(iii) **collisional broadening:** At high atomic densities or temperatures, collisions can disturb the phase of the coherent evolution of the two-level system. As a stochastic process this result in a Lorentzian spectrum [105, 157]. The width is given by the collision frequency $\Gamma_{\text{coll}} = v/\lambda_{\text{free}}$ and directly adds to the natural linewidth. Here, $v$ is the velocity of the atoms and $\lambda_{\text{free}}$ the mean-free-path.

(iv) **Doppler broadening:** For atoms moving with a certain velocity, the laser frequency is Doppler shifted. Since the velocity distribution of the atoms follows a Boltzmann distribution given by the temperature of the atomic cloud, this leads to a Gaussian line profile [157]. It needs to be convoluted with the natural Lorentzian line shape in order to obtain the combined spectral line profile.

(v) **propagation effects:** During the propagation through the atomic cloud, absorption reduces the intensity of the laser beam. Therefore, atoms at the end of the medium are exposed to a lower intensity. Saturation effects that can cause a broadening are thus weaker in this region. As a consequence, the linewidth gets reduced compared to the expected power broadened linewidth. This propagation effect gets stronger for larger beam intensities and larger optical depths of the atomic cloud.

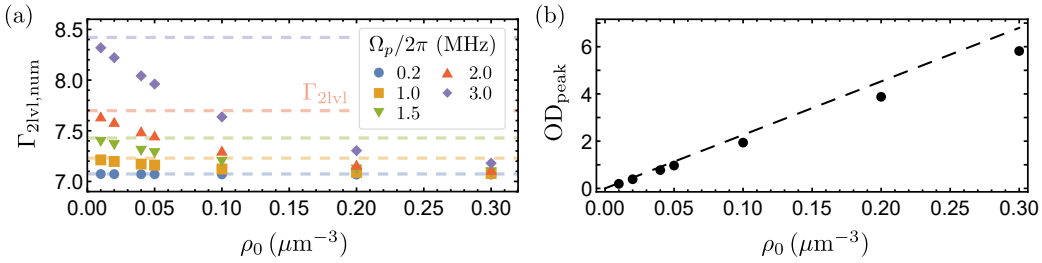


**Figure 4.10: Numerically calculated linewidth and peak OD of the two-level system.** (a) Linewidth $\Gamma_{2\mathrm{lvl,num}}$ as a function of the peak atomic density $\rho_0$ for different probe Rabi frequencies $\Omega_p$ and for $\gamma_{ge}/2\pi = 1\,\mathrm{MHz}$. Dashed lines indicate the expected linewidth $\Gamma_{2\mathrm{lvl}}$ calculated with Eq. (4.6) without propagation trough the medium. (b) Peak optical depth $\mathrm{OD}_{\mathrm{peak}}$ as a function of $\rho_0$ for the same dephasing as in (a). The dashed black line indicates the expectation from the geometry of the cloud, calculated with Eq. (4.3).

By relating the measured linewidth to the contributions listed above, it is possible to extract the dephasing rate $\gamma_{ge}$ from a measurement of the spectral response of the system. The effects (i) and (ii) can be captured by an analytic formula for the linewidth

$$\Gamma_{2\mathrm{lvl}} = \sqrt{\frac{(\Gamma_e + \gamma_{ge})(\gamma_{ge}^2 + \Gamma_e\gamma_{ge} + 2\Omega_p^2)}{\Gamma_e}} \tag{4.6}$$

of the two-level system as resulting from the density matrix element $\rho_{ee}$ of the single-body optical Bloch equations, Eqs. (2.10). As strong optical nonlinearities require high atomic densities or large probe beam intensities, power broadening (i) needs to be considered in our system. Moreover, homogeneous broadening effects (ii) directly enter the dephasing rate $\gamma_{ge}$ and thus will be determined in a measurement of the spectral response of the two-level system.

The collision frequency is about 130 kHz and the Doppler shift for Rubidium atoms is approximately 200 kHz for typical experimental parameters, i.e. an atomic density of $0.16\,\mu\mathrm{m}^{-3}$ and a temperature of $100\,\mu\mathrm{K}$ (see Sec. 4.1.3) [97]. As both are small compared to the natural linewidth of the intermediate state, collisional broadening (iii) and Doppler shifts (iv) can be neglected.

The propagation effect (v) depends non-trivially on possible dephasing mechanisms present in the system. Thus, it is difficult to modify Eq. (4.6) in order to accommodate for these effects. However, the propagation effect can be accounted for by numerically propagating the probe beam through the atomic cloud based on the Maxwell-Bloch equations. As an illustration, Fig. 4.10(a) shows the dependence of the numerically calculated linewidth $\Gamma_{2\mathrm{lvl,num}}$ as a function of the peak atomic density $\rho_0$ for different Rabi frequencies $\Omega_p$ of the probe beam and for $\gamma_{ge}/2 = 1\,\mathrm{MHz}$. In the limit of large densities, the linewidth tends towards $\Gamma_e + \gamma_{ge}$ for all values of $\Omega_p$. In the dilute regime at low atomic densities, $\Gamma_{2\mathrm{lvl,num}}$ approaches the value obtained from Eq. (4.6) without propagation through the atomic cloud (horizontal dashed lines). At the same time, the numerically ob-

tained peak optical depth OD, shown in Fig. 4.10(b), is smaller than the expectation based on the geometry of the cloud, Eq. (4.3), shown as a black dashed line. Both aspects highlight the importance of considering the propagation effect at high atomic densities and high Rabi frequencies of the probe beam.

### Determination of the dephasing rate from measurements of the optical depth[22]

In the discussion presented above we have established an understanding of possible effects that determine the two-level linewidth. Moreover, we have pointed out that at high atomic densities and high Rabi frequencies of the probe beam a numerical calculation of the linewidth is needed in order to account for a reduction of the probe beam intensity over the length of the medium.

Equipped with this knowledge, we now proceed by determining the dephasing rate $\gamma_{ge}$ from a linewidth measurement. For this purpose, we measure the optical depth OD of the atomic cloud as a function of the probe beam detuning $\Delta_p$ in the absence of the control beam ($\Omega_c = 0$) [97]. For comparability with our measurements in the interacting regime, presented in the following Sec. 4.4, we choose a rather high Rabi frequency $\Omega_p/2\pi = 1.7\,\mathrm{MHz}$.

In the low-density regime, shown in Fig. 4.11(a), we extract a linewidth of $2\pi\times(6.8 \pm 0.3)\,\mathrm{MHz}$ and a peak optical depth OD of $1.06 \pm 0.06$ using a Lorentzian fit to the data. Here, the error is the weighted error from the fit. In the high-density regime, as depicted in Fig. 4.11(b), we exclude data points with an OD greater than 1.8 from the fitting routine and obtain a rather large linewidth of $2\pi \times (7.9 \pm 0.5)\,\mathrm{MHz}$ with a peak OD of $3.8 \pm 0.2$. From the fit results and the independently measured geometry of the atomic cloud, we extract numerically the corresponding dephasing rates $\gamma_{ge}/2\pi = (0.5 \pm 0.3)\,\mathrm{MHz}$ and $\gamma_{ge}/2\pi = (1.7 \pm 0.5)\,\mathrm{MHz}$ for the low- and high- density measurements, respectively. The result is shown by blue solid lines in Fig. 4.11.

A density-dependent dephasing mechanism that could cause such a broadening is rescattering of photons. Due to the large extent of the atomic cloud transversal to the propagation direction, the transverse optical depth is large and allows for multiple rescattering of the photons [184, 185]. This could be an explanation for the observed dephasing at high densities.

The dephasing present in our system at high atomic densities prohibits to extract the atomic density by using the peak optical depth and the geometry of the cloud from absorption images as explained in Sec. 4.1.3. For the theoretical curves presented in the following, we linearly extrapolate the dephasing rates determined in the measurement presented in this section, based on the independently measured peak optical depth for the EIT spectra.

Moreover, for an estimation of the atomic density, in these measurements we fit the subsequent data of the Autler-Townes measurement in the non-interacting regime, see Sec. 4.4.1, with the peak atomic density as the only free fitting parameter. Its uncertainty results from shot-to-shot fluctuations of $\pm 8\%$, a statistical error of $\pm 2\%$ given by the uncertainty of the deduced dephasing rate $\gamma_{ge}$, and a

[22] Taken verbatim from Tebben *et al.* [96] with some adaptions for the ease of readability.

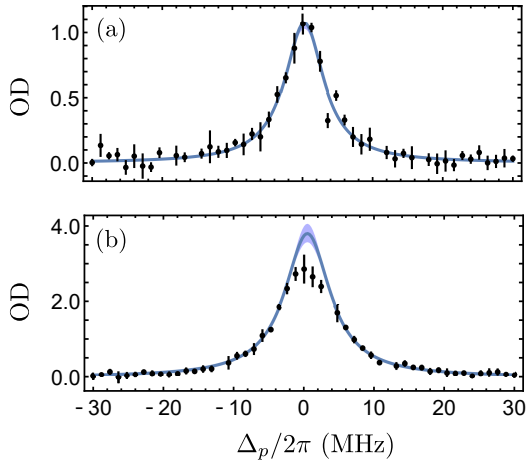


**Figure 4.11: Measured linewidth of the two-level system.** Optical depth OD as a function of the probe beam detuning $\Delta_p$ in the absence of the control beam ($\Omega_c = 0$) and for peak atomic densities of (a) $\rho_0 \approx 0.02\,\mu\text{m}^{-3}$ and (b) $\rho_0 \approx 0.2\,\mu\text{m}^{-3}$, respectively. The result obtained from numerically solving the Maxwell-Bloch equations, Eq. (2.10), is shown as a solid line with the shaded area indicating the uncertainty in the determined dephasing rate $\gamma_{ge}$. Figure and caption taken with permission from [97].

systematic overestimation of the propagation length resulting in an error of +4% for the atomic density. The uncertainty in the density is displayed by a shaded area around the theoretical curves in the plots of Sec. 4.5.

### 4.3.2 Dephasing in the three-level system

Next, we characterize the dephasing rates of the ground- to Rydberg-state coherence $\gamma_{gr}$ and the intermediate- to Rydberg-state coherence $\gamma_{gr}$ for the three-level system shown in Fig. 4.5(a). Possible sources for these dephasings are, for instance, the finite linewidth of the involved lasers, power broadening or motion-induced dephasing [78]. As we typically drive the three-level system with $\Omega_c > \Gamma_e$, dephasing on the intermediate- to Rydberg-state coherence can be neglected and is set to $\gamma_{er} = 0$ in all subsequent discussions. In the following, we explain how to extract the dephasing rate $\gamma_{gr}$ from the linewidth of the two-photon transition between the ground and the Rydberg state [46, 186, 187].

In the previous section we have discussed, that $\gamma_{ge}$ can be determined from the two-level spectral response. Here, the probe beam transmission serves as a probe for the ground- to intermediate-state coherence. In contrast, the dephasing rate $\gamma_{gr}$ can be characterized by measuring the linewidth of the two-photon transition between the ground and the Rydberg state with a large single-photon detuning $\Delta \gg \Gamma_e, \Omega_{p,c}$ to the intermediate state, as pursued in ref. [188]. Thereby, a large detuning $\Delta$ ensures that the fast decay of the intermediate state is effectively eliminated from the atom dynamics. The resulting effective two-level system undergoes Rabi oscillations with a two-photon Rabi frequency $\Omega_{\text{eff}} = \Omega_p\Omega_c/(2\Delta)$

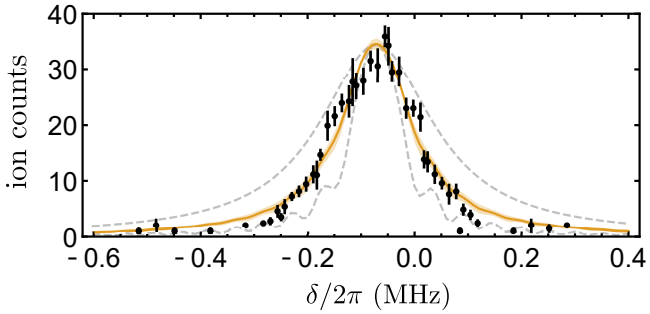


**Figure 4.12: Spectrum of the two-photon transition.** Measured ion counts against the two-photon detuning $\delta$ (black points) for an intermediate state detuning of 97 MHz (data taken from ref. [188], with kind permission of C. Brandl). We show by the solid orange line the numerical solution of the time-dependent optical Bloch equations, Eqs. (2.10), for a three-level system with a dephasing rate $\gamma_{gr}/2\pi = 33\,\text{kHz}$. The shaded area represents a variation of the dephasing rate by $\pm 10\,\text{kHz}$. For comparison, the numerical results for 0 kHz (lower gray dashed line) and 100 kHz (upper gray dashed line) are shown.

[189]. Based on an ion measurement, as explained in Sec. 4.1.3, the Rydberg population is determined and serves as an observable in such a measurement [187].

Fig. 4.12 presents a measurement of the ion counts on the MCP detector, being proportional to the number of Rydberg excitations in the medium, against the two-photon detuning $\delta$. The data is recorded for a large detuning $\Delta$ to the intermediate state of 97 MHz and an excitation time of 20 $\mu$s. We fit a Lorentzian function to the data and obtain a linewidth of $2\pi \times (159 \pm 7)$ kHz. In order to relate this linewidth to the dephasing rate $\gamma_{gr}$, we simulate numerically the time-dependent, single-body optical Bloch equations, Eqs. (2.10). Thereby, the Rabi frequencies $\Omega_p/2\pi = (2.36 \pm 0.05)$ MHz and $\Omega_c/2\pi = (5.7 \pm 0.1)$ MHz of the probe and control[23] beam, respectively, as well as the decay rate of the Rydberg state $\Gamma_r/2\pi = 17.5\,\text{kHz}$ are used as an input. We find that a dephasing of $\gamma_{gr}/2\pi = (33 \pm 4)\,\text{kHz}$ is necessary to obtain the fitted linewidth. The result is shown as the orange line in Fig. 4.12.

The measured dephasing rate gives an upper bound for the linewidths of the two lasers for an integration time of 20 $\mu$s. As subsequent measurements have been performed with excitations times of 5-15 $\mu$s and phase noise of the laser increases with increasing excitation time, this also gives an upper bound for the dephasing present in the subsequent measurements. In the following theoretical investigations this dephasing has been taken into account. However, we expect that it does not have a great impact on the theoretical predictions, as it is much smaller than the decay rate of the intermediate state and the dephasing rate $\gamma_{ge}$ determined in the previous section.

[23] Due to the inconsistency in the determination of the control beam waist (see Sec. 4.2) the dephasing rate $\gamma_{gr}$ has a large systematic error and could be of up to factor of two larger. Nevertheless, $2\gamma_{gr}$ is still small compared to all other frequencies in the system.

### 4.3.3 Adiabatic preparation of the EIT dark state

EIT relies on the preparation of a dark state that does not decay due to coupling to the intermediate state, as explained in Sec. 2.1.3. The most common way of preparing the atoms in the dark state is to use stimulated Raman adiabatic passage (STIRAP) [190–192]. Here, a counter-intuitive pulse sequence, where the control beam is switched on before the probe beam, is used to transfer the atoms adiabatically into the EIT dark state. Thereby, one needs to ensure that the instantaneous dark state $|a_0(t)\rangle$ does not couple to any of the other two instantaneous eigenstates $|a_\pm(t)\rangle$ of the system [99]. This is fulfilled if the coupling is much smaller than the energy $\omega^\pm(t)$ of the eigenstates [99]

$$\left|\left\langle \frac{\mathrm{d}}{\mathrm{d}t} a_0(t) | a_\pm(t) \right\rangle\right| \ll |\omega^\pm(t)| \,. \tag{4.7}$$

On single-photon resonance this condition reduces to [99]

$$\sqrt{{\Omega'_p}^2(t) + {\Omega'_c}^2(t)} \gg |\dot{\theta}(t)| \,, \tag{4.8}$$

where $\tan\theta = \Omega'_p(t)/\Omega'_c(t)$.

In our case we assume a linear rise of the probe Rabi frequency $\Omega'_p(t) = at$, where $a = \Omega_p/t_{\mathrm{AOM}}$ is given by the AOM rise time $t_{\mathrm{AOM}}$ of about 50 ns and the targeted maximal probe Rabi frequency $\Omega_p$. Furthermore, as we turn on the control beam 2 $\mu$s before the probe beam, we have $\Omega'_c(t) = \Omega_c$. Inserting both quantities into Eq. (4.8) leads for $\Omega_p \ll \Omega_c$ to the condition $\Omega_c^2/a \gg 1$ during the ramp of the probe beam Rabi frequency. For typical Rabi frequencies $\Omega_c/2\pi = 20$ MHz and $\Omega_p/2\pi = 1$ MHz used in our experiment, we find $\Omega_c^2/a \approx 126$, which is much larger than one. Therefore, the adiabaticity criterion holds and we expect an adiabatic preparation of the EIT dark state.

### 4.3.4 Autler-Townes spectrum in the non-interacting regime

As a final step for the characterization of our EIT system in the non-interacting regime, we present in Fig. 4.13(a) the transmission $T$ of the focused probe beam against the detuning $\Delta_p$ of the probe beam. The measured transmission spectrum exhibits a transmission of almost unity around resonance, indicating the largely coherent dynamics of the well-prepared three-level system. Moreover, the spectrum shows no asymmetry that could hint towards significant dispersive effects.

In experiments with Rydberg atoms, care has to be taken to avoid the creation of ions or spurious Rydberg excitations, as these could lead to additional absorption. A measurement of the ion counts on the MCP after completing the EIT sequence gives an indication if there are Rydberg excitations present in the medium. Fig. 4.13(b) displays the result of such a measurement, which has been obtained simultaneously to transmission measurement presented in Fig. 4.13(a). We observe that the number of ion counts fluctuates around the value of $0.743 \pm 0.096$. This number of ion counts has been measured in the absence of the control beam and is depicted by the gray dashed line in Fig. 4.13(b). Our measurement indicates

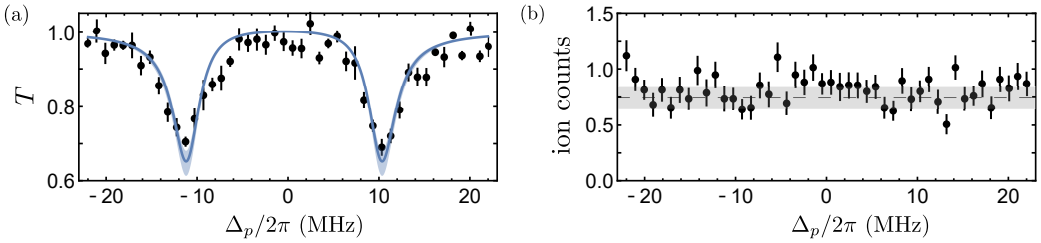


**Figure 4.13: Autler-Townes spectrum at a low atomic density.** (a) Measured transmission $T$ and (b) ion counts as a function of the probe beam detuning $\Delta_p$ for $\Delta_c = 0$ and for a peak atomic density of $(0.022 \pm 0.001)\,\mu\text{m}^{-3}$. The blue solid line in (a) shows the solution of the single-body optical Bloch equations, Eq. (2.10), where the shaded area accounts for the uncertainty in the atomic density. The gray dashed line in (b) marks the mean number of ions detected in the absence of the control beam, where the shaded area indicates one standard deviation.

that the number of Rydberg excitations in the medium is not significant for the presented transmission measurement. At higher atomic densities and larger ratios $\Omega_p/\Omega_c$ of the Rabi frequencies, as used in the subsequent measurements, we have observed a larger number of spurious Rydberg excitations. Therefore, we provide in App. C a detailed discussion about spurious Rydberg excitations in the context of the following measurements.

### 4.3.5 Summary of the main characteristics of our EIT system

We base our subsequent investigation of nonlinear effects in Rydberg EIT on the following main characteristics of our EIT system:

- **isolation of a three-level system:** With the experimental setup and sequence described in Sec. 4.1, we obtain in an optical dipole trap a $^{87}$Rb atom cloud that is cigar-shaped with $1/e^2$-waists of approximately $40 \times 40 \times 400\,\mu\text{m}^3$. The cloud has a temperature of about $100\,\mu$K and peak atomic densities up to $2 \times 10^{11}\,\text{cm}^{-3}$ are achievable [97]. Moreover, we ensure that approximately 95% of the atoms are in the ground state $|5S_{1/2}, F = 2, m_F = 2\rangle$ (Sec. 4.1.2). Using a magnetic field of 30 G provides a level splitting that is large enough to isolate a three-level system involving the Rydberg state $|48S_{1/2}, m_j = 1/2\rangle$.

- **minimized dispersive effects:** Implementation of a probe beam with a waist smaller than the control beam minimizes dispersive effects in EIT transmission spectra, as shown in Sec. 4.2.3.

- **characterized dephasing rates:** As discussed in Sec. 4.3.1, a density-dependent mechanism broadens the linewidth of the two-level system, which is driven by the probe beam. For the atomic densities used in subsequent measurements, the dephasing rate amounts to $\gamma_{ge}/2\pi = (1.4 \pm 0.5)\,\text{MHz}$ [97]. Moreover, we argue that $\gamma_{er} = 0$ for strong driving $\Omega_c \gg \Omega_p$, and

estimate $2\pi \times (33 \pm 4)\,\mathrm{kHz}$ to be an upper limit for the dephasing rate $\gamma_{gr}$ (Sec. 4.3.2).

- **adiabatic preparation of the EIT dark state:** With an appropriate pulse sequence we ensure an adiabatic preparation of the EIT dark state (Sec. 4.3.3).

## 4.4 Nonlinear absorption in the presence of interactions[24]

In this section, we report on investigations of the spectral response of the atomic medium in the presence of Rydberg interactions. First, we benchmark in Sec. 4.4.1 our Rydberg EIT system against existing measurements [23, 62, 64, 65]. For this purpose, we record the probe beam transmission as a function of the probe beam detuning $\Delta_p$ while staying on resonance with the control laser ($\Delta_c = 0$). This measurement follows the green dashed line depicted in Fig. 4.1. Afterwards, we present in Sec. 4.4.2 measurements on two-photon resonance by experimentally following the red line in Fig. 4.1. Here, a new approach for investigating Rydberg EIT is pursued, as the linear response of the medium vanishes in the non-interacting limit.

### 4.4.1 Autler-Townes spectrum with Rydberg interactions

In the non-interacting regime, meaning when the Rabi frequency of the probe beam is small, we vary the probe beam detuning $\Delta_p$ with the control beam on resonance ($\Delta_c = 0$). In this situation, we recover the known Autler-Townes spectrum, as shown by the black data points in Fig. 4.14. A transmission of nearly 1 at zero detuning and a symmetric spectrum supports negligible dephasing $\gamma_{gr}$ on the Rydberg coherence and therefore a largely coherent dynamics of the three-level system.

In the interacting regime at a higher Rabi frequency of the probe beam (red squares in Fig. 4.14), the transmission at zero detuning is reduced. Moreover, we observe a small shift of the left minimum and an asymmetry of the spectrum. Increasing the Rabi frequency of the probe beam even further (purple down-triangles) enhances these effects, while at the largest ratio of $\Omega_p/\Omega_c = 0.25$ of the two Rabi frequency (blue up-triangles) the characteristic Autler-Townes minima vanish completely.

In the first experimental demonstration of nonlinearities in a Rydberg EIT medium, no shift and no asymmetry of the EIT spectrum were measured [23]. A shift or an asymmetry of the spectrum could result from a mean-field shift induced by Rydberg excitations and ions in the medium. Therefore, the absence of these features has been explicitly attributed to the absence of Rydberg excitations or ions. Consequently, their measurements have been interpreted as resulting from a sole cooperative nonlinearity.

However, subsequent publications, even of the same group, showed measurements that exhibited both a shift and an asymmetry in the EIT as well as the

[24] Taken verbatim from Tebben *et al.* [96] and adapted.

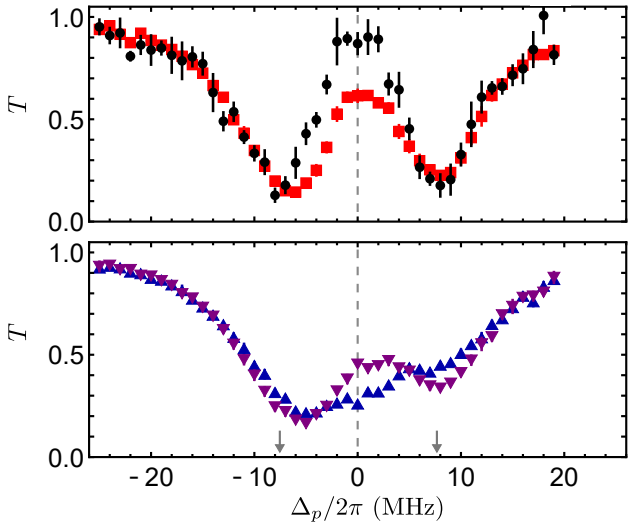


**Figure 4.14: Measured Autler-Townes spectra.** Transmission $T$ of the probe beam against the probe beam detuning $\Delta_p$ for ratios $\Omega_p/\Omega_c$ of the Rabi frequencies of 0.03 (black points), 0.12 (red squares), 0.18 (purple down-triangles) and 0.24 (blue up-triangles). Here, we use $\Delta_c = 0$, a fitted peak atomic density of $0.16\,\mu\text{m}^{-3}$, and a probe pulse duration of $15\,\mu\text{s}$. Gray arrows in the lower panel indicate the position of the Autler-Townes minima in the non-interacting regime (black curve). Figure and caption with permission adapted from [97].

Autler-Townes regime [62, 64, 65]. In one of them [62], the absence of the asymmetry in earlier measurements has been interpreted as the result of increased absorption due to interaction-induced motion in the time of one experimental cycle. In a simple picture this can be understood as follows: In the absence of atomic motion, a Rydberg pair excitation resonance for positive detuning of the probe beam reduces the population in the intermediate state. As a consequence, absorption is reduced and results in an asymmetry of the Autler-Townes spectrum. However, atomic motion due to repulsive interactions moves the atoms apart from each other. Thereby, interaction-induced level shifts are reduced, leading to a shift out of the Rydberg pair excitation resonance. As a result, the asymmetry of the spectrum is averaged out, leading to the conclusion that has been drawn in ref. [62].

Although, we cannot fully exclude motional dephasing originating from interaction-induced repulsion of the atoms in our system, we still observe the asymmetry in contrast to the argument given in ref. [62]. This discussion already shows that some experimentally observed features of Rydberg EIT spectra, with the control beam on resonance, remain to be explained.

### 4.4.2 Measurements on two-photon resonance

In order to investigate the effect of interactions on the transmission spectrum in a different approach, we perform measurements on two-photon resonance where the

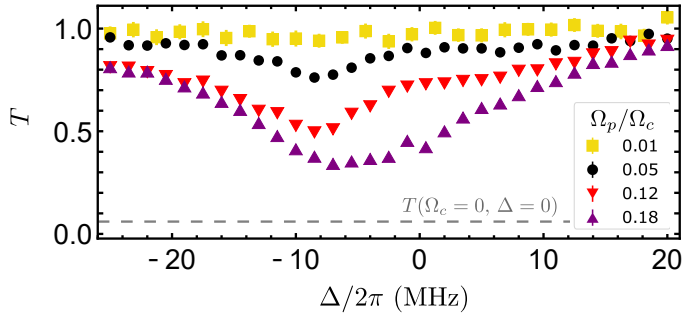


**Figure 4.15: Measurements on two-photon resonance.** Measured transmission $T$ of the probe beam on two-photon resonance $\delta = 0$ for different ratios $\Omega_p/\Omega_c$. The gray dashed line indicates the measured transmission in the absence of the control beam at $\Delta = 0$. Here, $\Omega_c/2\pi = 28\,\mathrm{MHz}$ for the yellow curve and 24 MHz for all other curves. The probe pulse duration is $5\,\mu\mathrm{s}$ for all measurements. Figure and caption taken with permission from [97].

linear response of the medium vanishes in the non-interacting limit (red line in Fig. 4.1). Precisely, we change the single-photon detuning $\Delta$ while staying on two-photon resonance ($\delta = 0$), and record the probe beam transmission as presented in Fig. 4.15.

At low Rabi frequencies $\Omega_p$, the probability to be in the Rydberg state is small, such that this regime can be considered as non-interacting. Here, nonlinear effects induced by Rydberg interactions are negligible. In this regime, the measured transmission is consistent with unity for all single-photon detunings, as shown by the yellow squares in Fig. 4.15. This is expected as on two-photon resonance the linear response of the atomic medium vanishes and EIT conditions are fulfilled.

Gradually increasing the probe Rabi frequency increases the fraction of atoms in the Rydberg state, such that interaction effects influence the dynamics. In this interacting regime, already for a ratio of $\Omega_p/\Omega_c \approx 0.05$, depicted by the black circles in Fig. 4.15, a dip in the transmission to about $T = 0.76$ appears on the negative detuning side. However, this dip is absent on the positive detuning side. For the experimental parameters of this measurement, we can exclude the possibility that this absorption feature results from the influence of stationary Rydberg excitations or ions in the medium. In order to support this statement, we present a measurement of Rydberg excitations after the EIT sequence and an estimation of an upper limit for the resulting absorption from these in App. C.

Increasing the probe Rabi frequency further (red down triangles in Fig. 4.15) increases the strength of the absorption dip, but does not change its position. Moreover, the feature is getting broader, but remains clearly visible until $\Omega_p/\Omega_c \approx 0.12$. For the largest ratio $\Omega_p/\Omega_c \approx 0.18$ of the two Rabi frequencies (purple up triangles), strong absorption continues to persists predominantly on the negative detuning side, but is shifted towards the single-photon resonance and with a broadening. Therefore, the observed absorption feature turns out to be very sensitive to $\Omega_p$, which is characteristic for a nonlinear phenomenon.

## 4.5 Comparison with theoretical models[25]

We now aim at a comparison of our measurements with existing theoretical models. Our measurements have been performed in a regime, where the optical depth per blockade radius $\mathrm{OD}_b \ll 1$, such that the probe field can be treated classically. As a consequence, photon-photon and atom-photon correlations can be neglected [77]. However, interactions between atoms induce atom-atom correlations. On the one hand, these correlations enable strong nonlinear effects and therefore make the system potentially useful for quantum optics applications. On the other hand, they make a theoretical treatment of the Rydberg EIT medium challenging.

As discussed in Sec. 3.1.2, there exists several approaches to include Rydberg interactions into theoretical models. In the following, we compare our measurements with the predictions based on a mean-field model [64], a Monte-Carlo rate equation model [78], and the low intensity expansion [96, 121] that we introduced in detail in Sec. 3.3. For this purpose, we first provide an overview of the theoretical models and their range of validity in Sec. 4.5.1. Afterwards, we present the comparison with our measured Autler-Townes spectra and our measurements on two-photon resonance in Sec. 4.5.2 and Sec. 4.5.3, respectively.

### 4.5.1 Theoretical models and their range of validity

#### Mean-field model

Among other implementations of the mean-field model, we choose to compare our experimental results with an ansatz followed in ref. [64]. We make this choice as experimental parameters in ref. [64], such as the ratio $\Omega_p/\Omega_c$ and the atomic density, are similar to our measurements. In ref. [64], the transmission of the probe field is obtained from the one-dimensional Maxwell Bloch equation, where the optical response of the medium enters as a model susceptibility $\bar{\chi} = \alpha\chi_B + (1-\alpha)\chi_E$ [64]. This model susceptibility is based on the solution for the susceptibility $\chi_{3\mathrm{lvl}}$ of the single-atom master equation for a non-interacting three-level system and includes interactions in terms of level shifts. The two different parts $\chi_B$ and $\chi_E$ of the model susceptibility are weighted according to the fraction $\alpha$ of all blockaded atoms excluding Rydberg atoms [64].

Thereby, $\chi_B$ describes the optical response of blockaded atoms. It is given by a spatial integration of $\chi_{3\mathrm{lvl}}(\Delta_c' = \Delta_c + C_6/r^6)$ over the radius $r$ inside the blockade radius. Here, interactions induce a level shift to the Rydberg state such that $\chi_B$ equals the two-level susceptibility for strong interactions. In addition, $\chi_E = \chi_{3\mathrm{lvl}}(\Delta_c' = \Delta_c - \Delta_R, \gamma_{gr} = \sqrt{\theta_R})$ accounts for interactions of unblockaded atoms with Rydberg excitations at a distance larger than the blockade radius. For this purpose, an average shift $\Delta_R$ and its variance $\theta_R$ are introduced, where the latter leads to a dephasing $\gamma_{gr}$ of the Rydberg coherence [64]. In this model $\Delta_R$ and $\theta_R$ are based on a local density approximation and an approximation for the Rydberg excited fraction, which is derived from a semi-analytical model using superatoms [125].

[25] Taken verbatim from Tebben *et al.* [96] and adapted.

### Monte-Carlo rate equation (MCRE) model

In this approach, the single-atom master equation without interactions is cast into a set of rate equations by adiabatically eliminating the coherences [81–83]. Interactions are included as effective level shifts $\Delta_{\mathrm{int}}^{(i)} = \sum_{j \neq i} C_6 / r_{ij}^6$ for the Rydberg level of the $i$-th atom with distance $r_{ij}$ to atom $j$. Using a Monte-Carlo simulation, the many-body problem is solved by propagating the global ground state to the global steady state. In the Monte-Carlo rate equation (MCRE) model the propagation of the probe field can be included [78]. This is done by taking into account the local probe Rabi frequency $\Omega_p^{(i)}$, which atom $i$ experiences, for the calculation of the steady state of atom $i$ in each Monte-Carlo step. For this purpose, the probe field with local Rabi frequency is propagated through the cloud of randomly positioned atoms according to the one-dimensional Maxwell-Bloch equation until atom $i$ is reached. Thereby in each propagation step, the local attenuation, which is induced by the individual atoms that are passed, is subsequently accounted for. As a result, not only global atomic observables, but also the probe beam transmission can be simulated with this approach.

### Low-intensity theory

This semiclassical model has been described in detail in Sec. 3.3. In essence, this model is based on a low-intensity expansion [58, 96] of the Maxwell-Bloch equations for the driven atomic system. Here, Rydberg interactions evoke atomic correlations. Assuming that the Rydberg population per blockade radius is small, these correlations can be truncated after the second order. As a result, an analytic solution for the linear and nonlinear susceptibility can be derived, which takes two-body correlations exactly into account [96]. The transmission of the probe beam is then calculated analytically by applying a local density approximation and assuming spatially constant probe and control beams.

### Range of validity of the three models

For a comparison of the range of validity of these theoretical models, the strength of the applied fields, the atomic density, and the interaction strength are considered in the following.

The mean-field model includes Rydberg interactions solely as an interaction-induced energy shift based on the assumption that inter-atomic correlations can be completely neglected. This assumption requires that the mean distance between Rydberg excitations is larger than the blockade radius. This is the case, for example, if $\Omega_p / \Omega_c \ll 1$ or if the interaction strength is small. A simple mean-field model failed to explain observations in coherent population trapping experiments as soon as excitation blockade becomes relevant [84]. Depending on the experimental parameters, this might already be the case for low atomic densities. The mean-field model considered here agreed well with an interaction-induced shift and dephasing observed in interacting EIT transmission spectra for densities in the order of $0.1\,\mu\mathrm{m}^{-3}$ [64].

The MCRE model also includes Rydberg interactions as effective energy shifts, but does not rely on assumptions for calculating the average shift experienced by one atom. Instead, it naturally includes the mean-field shift in a self-consistent manner and calculates the steady-state of the $N$-body density matrix. While still requiring $\Omega_p/\Omega_c \ll 1$ or $\Omega_p/\Omega_c \gg 1$ for atomic coherences to vanish [125], these two aspects increase its range of validity to a large range of atomic densities and yields correct results also for densities as high as $0.18\,\mu\mathrm{m}^{-3}$ [62, 82]. For $\Omega_p/\Omega_c \ll 1$, the rate equation model was shown to agree well with the result of a master equation calculation of four fully blockaded atoms independent of the driving strength $\Omega_c/\Gamma_e$ [125]. As a result, the MCRE model was able to explain certain aspects of interacting EIT spectra and the density dependence of nonlinear absorption [62, 78].

The low-intensity theory is based on a perturbative expansion in the probe field and therefore requires $\Omega_p/\Omega_c \ll 1$. Its applicability in terms of atomic densities and interaction strengths is combined in the requirement that the Rydberg population per blockade volume needs to be much smaller than 1 [77, 96, 121]. The low-intensity theory predicts the existence of an enhanced nonlinear optical response for $\Delta \sim \pm\Omega_c/2$ as a consequence of a two-body, two-photon resonance in the non-adiabatic regime [96]. However, it so far has not been compared to experiments in this regime yet. In the regime of large probe beam detunings, where the intermediate state can be adiabatically eliminated, the low-intensity theory has successfully been compared to absorption measurements showing the quadratic dependence on the Rabi frequency of the probe beam at moderate densities [58].

### Consideration of the experimental geometry within the three models

For a comparison with our experimental results, we exploit the three models[26] [64, 78, 96] with a transversely constant intensity of the probe beam and a constant intensity of the control beam in all spatial dimensions. All three models account for the 45° angle between the propagation direction of the lasers and the main axis of the atomic cloud, as depicted in Fig. 4.2. Moreover, they include the Gaussian density distribution in the propagation direction. In the MCRE model, the Gaussian density distribution in the transversal direction is considered[27]. However, it is assumed to be constant for the other two models, such that they are reduced to a one-dimensional situation. This approximation is justified since the probe beam waist is small compared to the cloud dimension in transversal direction. We have checked that in the absence of interactions all three models coincide with each other.

[26] M. Gärttner has provided the code for the MCRE model, which I have adapted, e.g. in terms of the experimental geometry and output quantities. The adapted code has been used for the simulations presented in the following. Scripts for the other two models have been written by myself based on refs. [64, 96].

[27] We have restricted the transversal plane to a region of $8 \times 8\,\mu\mathrm{m}^2$. For the results presented in Fig. 4.17, we have tested that doubling this area gives within the errorbars the same result for $\Delta/2\pi \geq -17\,\mathrm{MHz}$.

### 4.5.2 Comparison with Autler-Townes measurements

First, we compare the predictions of the theoretical models presented in Sec. 4.5.1 with our Autler-Townes measurement. The Rydberg population per blockade volume of the interacting Autler-Townes measurement is 0.16 on resonance and increases off-resonance even further. Since it cannot be considered much smaller than 1, we omit a comparison of the low-intensity theory with the Autler-Townes measurement in the following. For the measurements with the two smallest Rabi frequency ratios, as presented in the upper panel of Fig. 4.14, the requirement $\Omega_p/\Omega_c \ll 1$ holds. Moreover, the atomic density is in a regime where a comparison with the other two models is possible. In the following, we thus use these two measurements for a comparison with the predictions based on the mean-field model und MCRE simulation.

As an input for the mean-field model and the MCRE simulation, we use for both a dephasing rate $\gamma_{ge}/2\pi = (1.4 \pm 0.5)\,\mathrm{MHz}$ of the excited-state coherence. Hereby, we account for density-dependent dephasing present in the system (see Sec. 4.3.1 for details). Dephasing due to laser noise was independently determined in a measurement of the two-photon linewidth and found to be $\gamma_{gr} = (33 \pm 4)\,\mathrm{kHz}$, as detailed in Sec. 4.3.2. Furthermore, we determine the peak atomic density with a fit to the Autler-Townes spectrum in the non-interacting regime and find $(0.16 \pm 0.02)\,\mu\mathrm{m}^{-3}$ with a systematic error of $+4\%$ (see Sec. 4.3.1). With these quantities as an input, the resulting transmission spectra obtained from the mean-field model and the MCRE simulation are shown as blue solid and orange-dashed lines in Fig. 4.16, respectively. The shaded area around both curves takes the uncertainty in the atomic density into account.

In the non-interacting regime, the mean-field model and the result of the MCRE simulation agree well with the measured transmission spectrum in Fig. 4.16(a). Slight deviations around the Autler-Townes minima are apparent, which can originate from a small fluctuation of the control beam power and a possible small misalignment of the counter-propagating beams. These effects are not included in the theoretical models.

In the interacting regime, shown in Fig. 4.16(b), a reduction of the transmission around $\Delta_p = 0$ and an asymmetry in the spectrum are predicted by the two models. Moreover, both theories predict a shift of the resonance position to $\Delta_p/2\pi \approx 3\,\mathrm{MHz}$. The deviation of the transmission obtained with the two theories around single-photon resonance can be explained by the different implementation of the interaction-induced level shift and its variance in the two models (see App. D for details).

Compared to the experimental results, the asymmetry predicted by the two models agrees well with the measured one, as can be seen in Fig. 4.16(b). On resonance at $\Delta_p = 0$, we observe a lower transmission as the one obtained from the two theories. Including an effective dephasing rate $\gamma_{gr}$ in the models could resolve this deviation. Such a dephasing could originate from the interaction with spurious Rydberg excitations, which might be present in the medium for this measurement as discussed in App. C. However, while both models predict a shift of the resonance position, we do not observe this large shift in the experiment.

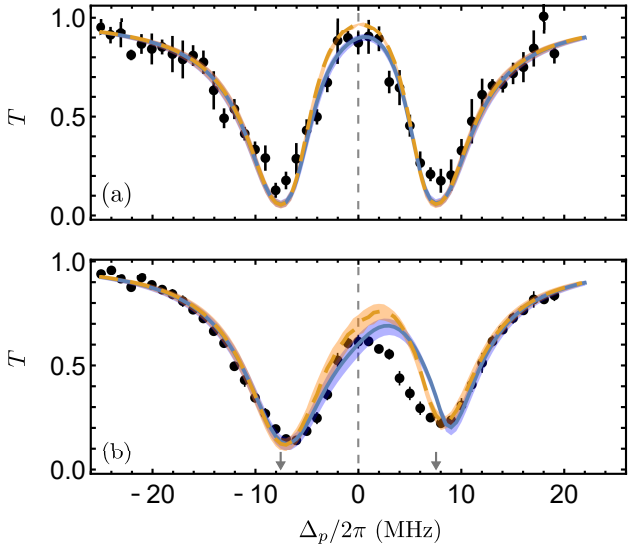


**Figure 4.16: Comparison of Autler-Townes spectra presented in Fig. 4.14(a) with theoretical models.** The measured probe beam transmission $T$ against the probe detuning $\Delta_p$ is shown (black points) for (a) $\Omega_p/\Omega_c = 0.03$ and (b) $\Omega_p/\Omega_c = 0.12$. Here, $\Delta_c = 0$, and the probe pulse duration is $15\,\mu$s. The transmission spectra calculated with a mean-field model (blue solid line) and a MCRE simulation (orange dashed line) are depicted for a fitted peak atomic density of $0.16\,\mu\text{m}^{-3}$. Shaded areas take into account the uncertainty in the atomic density. For both theoretical curves, $\Omega_c/2\pi = 15\,\text{MHz}$ and $\gamma_{ge}/2\pi = 1.4\,\text{MHz}$. Gray arrows in (b) indicate the position of the minima of the curve in (a). Figure and caption taken with permission from [97].

The attenuation of the transmission on resonance is a consequence of Rydberg blockade-induced absorption and an experimentally and theoretically approved feature of interacting Rydberg EIT systems [77]. However, the absence or presence of a shift and an asymmetry in the spectrum are debated in the literature [62, 64]. In theories that rely on a mean-field shift of the Rydberg level, such as the considered mean-field and MCRE models, the asymmetry and shift are a consequence of an anti-blockade effect. This effect permits for a coupling to Rydberg pair states for a positive detuning of the probe field. As a consequence, absorption is reduced and the resonance position is shifted [62]. This shift also emerges in the solution of the master equation for a few atoms [78], but does not appear in a theory based on superatoms [124]. As discussed in Sec. 4.4.1 the asymmetry and shift might be reduced in setups, where interaction-induced atomic motion moves atoms out of the facilitation resonance [62].

### 4.5.3 Comparison with a measurement on two-photon resonance

In the following, we compare the predictions of the theoretical models with our measurements on two-photon resonance. For these measurements, the atomic

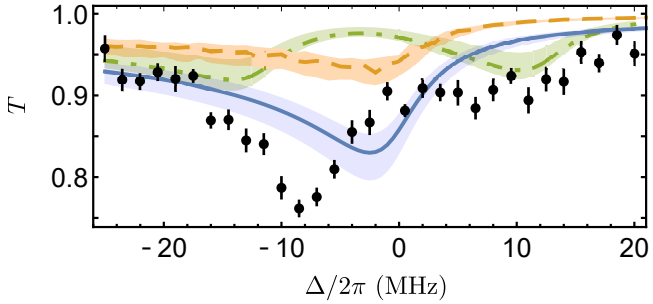


**Figure 4.17: Comparison of a measurement on two-photon resonance presented in Fig. 4.15(a) with theoretical models.** Measured transmission $T$ as a function of the single-photon detuning $\Delta$ for a ratio $\Omega_p/\Omega_c = 0.05$ of the Rabi frequencies (black points). Results of the mean-field model (blue solid line), the MCRE simulation (orange dashed line), and the low-intensity theory (green dashed-dotted line) are shown. Here, the peak atomic density is $0.16\,\mu\mathrm{m}^{-3}$ and $\gamma_{ge}/2\pi = 1.4\,\mathrm{MHz}$. Shaded areas take into account the uncertainty in the atomic density. Figure and caption taken with permission from [97].

density is in a regime where all three models should be applicable. Moreover, the Rydberg population per blockade volume is below 0.05 for the yellow and black curves in Fig. 4.15 for all detunings. However, it exceeds this threshold for the other two curves. This means that at least for the yellow and black curves, for which $\Omega_p/\Omega_c \ll 1$, the requirements for all three models are fulfilled.

In the non-interacting regime on two-photon resonance ($\delta = 0$), the transmission is nearly 1 for all single-photon detunings $\Delta$, as shown by the yellow squares in Fig. 4.15(a). This shows that experimental imperfections, which would lead to single-particle dephasing (e.g. an imperfect initial state preparation or remnant DC electric fields), are negligible. In all three theoretical models a transmission of 1 is expected. This is due to the fact that on two-photon resonance the population in the Rydberg state and thus interaction-induced shifts tend to zero for small $\Omega_p$ or small atomic densities. In combination with $\chi_{3\mathrm{lvl}}(\delta = 0) = 0$ for negligible single-particle dephasing, this results in a vanishing linear response. All three models reproduce this behavior correctly.

For the interacting regime, Fig. 4.17 shows a comparison of the measured transmission spectrum for $\Omega_p/\Omega_c = 0.05$, presented in Fig. 4.15, with the predictions provided by the three different models. For all three models, the independently measured Rabi frequencies are used as an input. The peak atomic density is estimated similarly to the Autler-Townes measurement and possesses the same uncertainty. Moreover, the dephasings $\gamma_{ge}$ and $\gamma_{gr}$ are the same as for the Autler-Townes measurements. Apparently all three models fail to describe the results of our measurement.

As shown in Fig. 4.17, only qualitatively one absorption dip on the negative detuning side is predicted by the mean-field and MCRE models. However, its position deviates from the measured one by about 6 MHz. Moreover, it cannot be

superimposed with the measured absorption dip by changing parameters, such as the atomic density or dephasing rates, within an acceptable range with respect to the experimental parameters. The stronger absorption predicted by the mean-field model compared to the MCRE simulation stems from the inclusion of the variance $\theta_R$ of the interaction-induced shift in the mean-field model. The effect of this variance is more important as compared to the Autler-Townes case, presented in Fig. 4.16, since the fraction $\alpha$ of all blockaded atoms excluding Rydberg atoms is smaller. This variance is not explicitly included in the MCRE simulation (see App. D for details).

The low-intensity theory predicts two transmission minima as a consequence of a two-body two-photon resonance [96]. However, even though the assumptions for this model are met, neither the level of the observed transmission nor the position of enhanced absorption are captured by this model, as shown in Fig. 4.17. Most strikingly, while the theory predicts two absorption features, only one has been measured. Therefore, also this model does not explain our measurement results.

## 4.6 Summary and discussion

In this chapter we have studied the spectral properties of Rydberg EIT in the semiclassical regime. For this purpose, we have first introduced our experimental apparatus, which is capable of simultaneously detecting atomic and optical properties of the Rydberg EIT medium. In particular, the transmission of the probe beam can be measured via absorption imaging, and residual Rydberg excitations in the medium can be detected via electric field ionization. Aiming at the observation of genuine dissipative effects, we have minimized dispersive effects that originate from spatial variations of the control beam [180]. For this purpose, we have implemented an experimental geometry where the waist of the control beam is larger than the one of the probe beam. Moreover, we have carefully prepared and characterized the EIT three-level system in the non-interacting regime, e.g. in terms of dephasing rates.

Based on this preparatory work, we have first probed the spectral response of the medium in the conventional way, meaning with the control laser on resonance. This yields a so-called Autler-Townes spectrum [97]. The observed nonlinear features in the Autler-Townes spectrum in the interacting regime are comparable to previous measurements and theoretical models [23, 62, 64, 65]. Although the reduction of the transmission on resonance is apparent in all these measurements including ours, the occurrence of a shift and asymmetry is under discussion [62, 64, 97].

Afterwards, we have proceeded by investigating the transmission of the probe beam on two-photon resonance, while changing the single-photon detuning [97]. Since on two-photon resonance purely nonlinear effects persist, theoretical models are more rigorously tested with our measurements in this regime [97]. We have observed a broad absorption feature that appears for negative single-photon detunings. We have compared our experimental results with the prediction of models that include Rydberg interactions via an energy shift of the Rydberg level

[64, 78], or treat interactions pairwise [96, 121]. However, neither of them is able to capture the observed transmission spectrum [97]. This underlines the importance of our measurements to serve as a benchmark for future improved descriptions of Rydberg EIT.

In the following, we discuss our results and some possible routes towards a better understanding of our observations on two-photon resonance from both a theoretical and an experimental point of view.

### 4.6.1 Theoretical models and possible improvements

Of central importance for the description of Rydberg EIT systems in the semiclassical regime is the incorporation of atomic correlations in theoretical models. Theories that completely neglect correlations in a mean-field approach [60, 64, 65, 80], take many-body correlations approximately into account as in the Monte-Carlo rate equation (MCRE) model [78, 81–83], or only consider two-body correlations in a low-intensity expansion [58, 96, 121], all seem to fall short in capturing the nonlinear effects observed in our measurements [97].

Atomic correlations would be included accurately in an exact description of the many-body dynamics. However, this would require to solve the many-body optical Bloch equations for $N$ atoms, which would comprise a set of $3^{2N}$ coupled differential equations. This has been achieved for five atoms in ref. [78], but becomes computationally demanding for a larger number of atoms. An equivalent description in terms of a Monte-Carlo wave function approach [193] can yield steady-state solutions for a larger system size, as the number of variables scales with $3^N$. For example, Rydberg excitation dynamics have been investigated for ten atoms with this method [79]. But a system size of $N \sim 10^5$ as used in our experiments is far too large to obtain an exact solution for the full many-body system [97].

However, Pritchard *et al.* have shown that the solution of the optical Bloch equations for $N = N_b$ interacting atoms provides reasonable agreement with their experimental results [23]. Here, $N_b$ is the average number of blockaded atoms, which equals 3 in their case. For a typical atomic density of $0.16\,\mu\mathrm{m}^{-3}$ and a blockade radius of about $2.4\,\mu\mathrm{m}$, the number of blockaded atoms $N_b \sim 9$ in our system. With appropriate computational effort, it might be possible to obtain the steady-state solution for a system of nine atoms, using the Monte-Carlo wave function approach. The probe beam transmission could then be calculated from the ground to excited state coherence. Certainly, it would be interesting to compare the result of such a simulation to our measurements. Nevertheless, the propagation of the probe beam is not included consistently in such an approach, as compared for example to the MCRE simulation. Also, interaction effects beyond the blockade volume would be neglected. Therefore, there might still be deviations between measurement and simulation results.

Besides seeking an exact solution of the many-body dynamics, advancing existing approximate models is another approach to explain our findings [97]. Therefore, we discuss possible improvements of the MCRE model and the low-intensity expansion in the following. In ref. [83] the MCRE model has been extended to

account for two-body correlations exactly, yielding the so-called "hybrid" model. The idea is to treat neighboring atoms with a distance smaller than a critical length as pairs. For those the two-body rate equations are solved exactly in each Monte-Carlo step [83]. We have considered to adapt this model by implementing the probe beam propagation similar as in ref. [78]. This means that the two-body dynamics of the atom, which is considered in one propagation step, and its nearest neighboring atom is solved exactly to determine the probe beam attenuation. However, at high atomic densities as applied in our experiments, each atom is on average paired with more than one atom. This prevents an unambiguous choice of pairs [97]. Therefore, treating larger atomic clusters is required in future theoretical studies [97]. However, we want to note that the computational time needed to find the steady-state solution of a cluster increases with the cluster size. As an average over many trajectories is required for the convergence of the steady-state in the MCRE simulation [78, 83], treating extended atomic clusters is expected to be computationally demanding.

Our theory [96, 121] is based on a low-intensity expansion. It exactly takes into account the two-body quantum dynamics, as explained in Sec. 3.3, but completely neglects mean-field shifts of surrounding Rydberg atoms. In a simple approach to include these mean-field shifts, we have combined the low-intensity expansion model, which provides an analytic solution for the third-order susceptibility [96], with the first order susceptibility of the mean-field model [64]. However, this approach did not lead to a better agreement with the measured data. A rigorous inclusion of higher-order correlations, by extending the expansion to the third or even a higher order via a systematic cluster expansion and a ladder approximation [97], could be pursued in future studies.

### 4.6.2 Experimental considerations and further investigations

The observation of genuine nonlinear effects in Rydberg EIT with classical light fields is greatly complicated and affected by the presence of stationary Rydberg excitations [143]. This is because these excitations can lead to spurious absorption or even an avalanche creation of ions [177], which obscures absorption stemming from nonlinear effects. We have observed that the parameter window where these Rydberg excitations, so-called Rydberg pollutants [143], are suppressed is very small, e.g. in terms of the Rabi frequency of the probe beam (App. C). We emphasize that only in this parameter regime an unambiguous observation of Rydberg EIT effects is possible. At the same time, the precise origin of these pollutants remains vague (see App. C and refs. [97, 143, 194]). Therefore, we can fully support the statement of ref. [143] that further experimental investigations of Rydberg EIT would vastly benefit from a concise study of the creation process and a possible suppression of Rydberg pollutants. For example, state-selective field ionization [174, 195] could be used to determine the state in which these Rydberg pollutants are excited. This method exploits electric field ramps in order to control the ionization and therefore the arrival time of excitations in different Rydberg states on the ion detector. Subsequent suppression of these excitations could greatly increase the parameter regime for genuine Rydberg EIT experiments.

Besides the presence of stationary Rydberg excitations, atomic motion is an obstacle for cold atom experiments that needs to be considered. The effect of Doppler broadening is negligible in our setup as the net momentum is small in case that the probe and control beams are counter-propagating. Nevertheless, we cannot fully exclude the possibility that atomic motion, induced by repulsive van der Waals interactions [62], affects our measurements. We have briefly discussed an intuitive picture of how interaction-induced atomic motion could affect an Autler-Townes spectrum in the interacting regime (see Sec. 4.4.1 and ref. [62]). Nevertheless, its applicability is questionable as it is not a priory clear how motional and spin degree of freedoms are coupled due to Rydberg interactions. Due to the same reasoning, it is also difficult to find an intuition of how atomic motion could affect our measurements on two-photon resonance. On a single-body level, motion-induced dephasing could either depend on the atomic or the Rydberg excitation density [78]. For both cases we tested that including such a dephasing into the mean-field model does not improve the agreement with our measurements on two-photon resonance. Therefore, from an experimental perspective, it would be interesting to investigate if the observed absorption feature changes with the excitation time. From a theoretical point of view, the exploration of motional effects beyond a single-body dephasing would be very beneficial.

The main experimental result of this chapter is the observation of an absorption feature in the transmission spectrum of the probe beam on two-photon resonance [97]. As this regime has so far not been explored yet, our observation is interesting by itself. However, due to spurious Rydberg excitations in the medium, our measurements only cover a small parameter regime. In order to thoroughly characterize this absorption feature, it would be beneficial to map out its dependence on experimental parameters, such as the Rabi frequencies of the probe and control beam, as well as the atomic density. In this way the scaling of the absorption feature with these parameters could be measured and compared to theoretical models.

Finally, reducing the number of blockaded atoms in an experimental setting, might simplify the comparison with theoretical models as discussed above. Therefore, finding a parameter regime where this number is reduced, while at the same time the absorption feature is still observable without any spurious Rydberg excitations in the medium, is an interesting task for future investigations.

CHAPTER 5

# A stationary Rydberg polariton

*Parts of this chapter are based on the following manuscript, from which parts of the text have been taken verbatim*:

> **A stationary Rydberg polariton**
> A. Tebben, C. Hainaut, A. Salzinger, T. Franz, S. Geier, G. Zürn and M. Weidemüller, arXiv: 2108.00657 (2021)

In the introduction of this thesis we have asked the question how to enhance photon-photon interactions. Consider the situation of two photons propagating along each other as polaritons in a Rydberg EIT medium of optical depth OD. In the dissipative regime, the probability for these two photons to blockade each other scales as $1 - e^{-\mathrm{OD}_b}/\sqrt{\mathrm{OD}}$ [24, 85], while in the dispersive regime the associated phase shift is proportional to $\mathrm{OD}_b$ [57, 85]. Thus, increasing the optical depth per blockade radius $\mathrm{OD}_b$ enhances photon-photon interactions. However, the optical depth per blockade radius is experimentally limited, for example, due to atom-electron collisions emerging at high atomic density or high principle quantum number [85]. The highest reported values of recent experiments amount to $\mathrm{OD}_b \sim 6$. [10, 86, 140]. One possibility to circumvent this limitation given by the optical depth per blockade radius is to place the atomic medium into a cavity [87–91, 196]. In this way the photons pass the medium several times, which effectively enhances the single-atom coupling strength and thus increases the effect of interactions [4].

Instead of increasing the interaction strength, photon-photon interactions could also be enhanced by an increased interaction time [59, 92, 93]. In the case of two co-propagating photons, the available interaction time is limited by the time they spent in the medium as propagating polaritons [85, 197]. Reducing the velocity of the polaritons is possible, as discussed in Chap. 2. However, this immediately also reduces their photonic character [26, 30]. In the ultimate limit of a vanishing group velocity, the photons are fully converted into stored spin waves leaving only interacting atomic excitations behind. Enhanced interactions due to the storage process [59, 93], and the interaction between a spin wave and a stationary light pulse [92] have been demonstrated. However, both situations miss true photonic

interactions as the rely on storing the photons as a spin wave in the medium.

An alternative approach to increase the photon-photon interaction time is to enable interactions between stationary light polaritons (SLP). These quasi-particles [31, 34, 44, 117] maintain a non-vanishing photonic component at zero group velocity. In the following, we pursue this approach by adding a Rydberg character to a SLP. A first proposal in this regard has been based on a diamond level scheme [94, 95], where the uppermost state is a high-lying Rydberg state. This scheme has the drawback that the wavelengths of the probe and control fields are vastly different. As a consequence, phase matching conditions might be complicated to fulfill in an experimental realization [37, 94, 95]. However, this is a particularly important requirement since a phase mismatch can lead to a decay of the SPLs [92], and thus ultimately to a limited interaction time [98].

Another level scheme, which supports a stationary light polariton, is the dual-V scheme [34, 44]. As discussed in Sec. 2.2.3, this scheme relaxes the requirement for phase matching considerably. In a recent proposal, this system has been equipped with a Rydberg component by coupling a Rydberg state to one of the intermediate states [117]. This approach does not enable interactions between SLPs, but rather allows for a sophisticated and coherent switch between slow- and stationary light polaritons based on Rydberg interactions [117].

In this chapter, we propose a novel scheme for coupling a Rydberg state to a stationary light polariton based on the dual-V scheme [98]. It is not *a priori* clear that such a coupling preserves the stationary nature of the underlying SLP. Therefore, based on the discussion in ref. [34], we explicitly verify in Sec. 5.1 that our system supports a stationary photonic excitation with a quadratic dispersion relation, which we call a stationary Rydberg polariton. In order to explore the influence of interactions originating from the Rydberg character on our scheme, we investigate the effect of a Rydberg impurity on the system in Sec. 5.2. We then consider an experimental realization of stationary Rydberg polaritons in Sec. 5.3. Finally, in Sec. 5.4 we summarize and discuss our results[28].

## 5.1 Coupling a stationary light polariton to a Rydberg state[29]

We consider a dual-V scheme realization of a SLP [34, 44], as schematically depicted in Fig. 5.1(a). Here, two counter-propagating classical control fields with equal Rabi frequency $\Omega$ induce stationary light conditions for two quantized probe modes $\hat{\mathcal{E}}_{\pm}$, as discussed in Sec. 2.1.5. The underlying atomic level scheme is shown in Fig. 5.1(b) and is composed of a ground-state $|g\rangle$, a metastable state $|d\rangle$, and two intermediate states $|e_{\pm}\rangle$ that decay with rate $\gamma$. We couple the metastable state $|d\rangle$ to a Rydberg state $|r\rangle$ using a classical Rydberg coupling field with Rabi frequency $\Omega_s$.

The equations of motion for the probe field amplitudes and for the continuous

[28] This paragraph on the structure of this chapter is partially taken verbatim from Tebben *et al.* [98].

[29] Taken verbatim from Tebben *et al.* [98] with minor adaptions for the ease of readability.

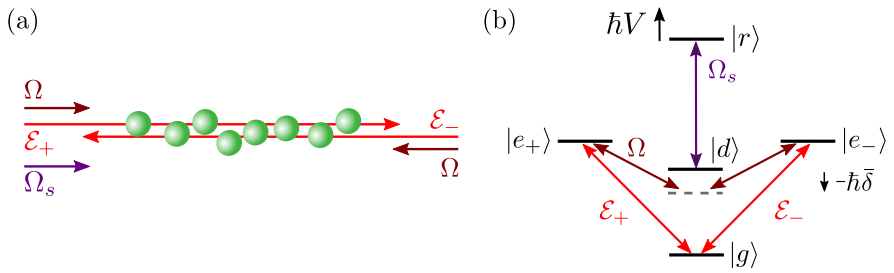


**Figure 5.1: System and level scheme for the creation of a stationary Rydberg polariton.** (a) Schematic illustration of the applied fields for the creation of a stationary Rydberg polariton. (b) Our suggested level scheme for a stationary Rydberg polariton based on a dual-V level scheme. In the presence of a Rydberg impurity, the Rydberg state experiences an energy shift $\hbar V$. For details see the main text. Figure and caption taken and adapted with permission from [98].

bosonic field operators $\hat{D}$, $\hat{S}$ and $\hat{P}_\pm$ of the coherences [26, 30] in the system read in analogy to refs. [34, 44, 117]

$$\partial_t \hat{\mathcal{E}}_\pm = \mp c\partial_z \hat{\mathcal{E}}_\pm - iG\hat{P}_\pm\,, \tag{5.1}$$

$$\partial_t \hat{P}_\pm = -iG\hat{\mathcal{E}}_\pm - i\Omega\hat{D} - \bar{\gamma}\hat{P}_\pm\,, \tag{5.2}$$

$$\partial_t \hat{D} = -i\Omega(\hat{P}_+ + \hat{P}_-) - i\Omega_s\hat{S} - i\bar{\delta}\hat{D}\,, \tag{5.3}$$

$$\partial_t \hat{S} = -i\Omega_s\hat{D} - i(\Delta_s + \bar{\delta})\hat{S}\,. \tag{5.4}$$

Here, we have used the short notation $\hat{\mathcal{O}}(z,t) = \hat{\mathcal{O}}$ for all operators. Furthermore, we have introduced the two-photon detuning $\bar{\delta}$, which is considered to be the same for the two ground- to metastable state transitions, and the detuning $\Delta_s$ of the Rydberg coupling field. $G = g\sqrt{\rho}$ with the single-atom coupling strength $g$ and one-dimensional atomic density $\rho$, $\bar{\gamma} = \gamma/2$ and $c$ is the speed of light. One can cast the equations of motion, Eqs. (5.1)-(5.4), into the form

$$i\partial_t \Upsilon = \mathcal{H}_{\text{eff}}\Upsilon \tag{5.5}$$

with the column vector $\Upsilon = \left(\hat{\mathcal{E}}_+, \hat{\mathcal{E}}_-, \hat{D}, \hat{S}, \hat{P}_+, \hat{P}_-\right)^T$. The coefficient matrix $\mathcal{H}_{\text{eff}}$ can be readily obtained from Eqs. (5.1)-(5.4).

In the following, we assume a resonant coupling to the Rydberg state ($\Delta_s = 0$). We observe that diagonalizing the subsystem $\{\hat{D}, \hat{S}\}$ yields two eigenstates with eigenenergies $-\hbar\bar{\delta} \pm \hbar\Omega_s$, respectively. Under the condition $\bar{\delta} = \pm\Omega_s$ one of them is on two-photon resonance with the ground state, while the other one is shifted in energy by $|2\hbar\Omega_s|$. Due to the resulting similarity with the dual-V scheme without the Rydberg state, which has been studied in detail in ref. [34], we expect that the system can support a stationary polariton similar to the SLP in the dual-V scheme.

In order to confirm this expectation, we follow the ideas of ref. [34] and investi-

gate $\mathcal{H}_{\text{eff}}$ in momentum space. Considering the case[30] $\bar{\delta} = \Omega_s$, we diagonalize $\mathcal{H}_{\text{eff}}$ and find a unique dark-state of the form

$$\hat{\Psi} = \frac{1}{\mathcal{N}} \left[ \Omega \left( \hat{\mathcal{E}}_+ + \hat{\mathcal{E}}_- \right) - G \left( \hat{D} + \hat{S} \right) \right] , \tag{5.6}$$

with $\mathcal{N} = \left[ G^2 + 2\Omega^2 \right]^{1/2}$. It has exactly the same form as the stationary light polariton in the dual-V scheme [34] with the replacement $\hat{D} \to \hat{D} + \hat{S}$.

In order to obtain the dispersion relation associated to this dark state, we follow the calculation in ref. [34]. For small photon momenta and up to second order, we obtain the dispersion relation

$$\omega(k) \approx -\frac{ic^2 \bar{\gamma} \Omega^2}{G^2 (G^2 + \Omega^2)} k^2 . \tag{5.7}$$

In the inset of Fig. 5.2(a) we compare this result with a numeric calculation (black solid line) and find good agreement. We emphasize that with the replacement $\Omega \to \Omega/\sqrt{2}$ Eq. (5.7) is identical to the dispersion relation that has been found for the dual-V scheme without a Rydberg component [34]. The associated effective mass of the stationary polariton can be obtained from Eq. (5.7). Interestingly, it can be controlled with a particular choice of $\Omega$, but does not depend on $\Omega_s$. From the above discussion we conclude that our proposed scheme supports a stationary light polariton with a strong Rydberg component, which we call a stationary Rydberg polariton.

A stationary photonic excitation is characterized by no contribution from the intermediate states, equal contributions of the two probe field modes, and a quadratic dispersion relation. We want to underline that these characteristics can be used to investigate under which conditions the stationary Rydberg polariton is supported in the medium.

In the previous discussion we have focused on the particular situation where $\bar{\delta} = \Omega_s$. In Fig. 5.2(a), we also show the dispersion relation of the same eigenstate of $\mathcal{H}_{\text{eff}}$ for $\bar{\delta} = 0$. Also in this case, it displays a quadratic behavior for small photon momenta. Nevertheless, the state possesses a non-zero probability to be in one of the intermediate states, as shown in Fig. 5.2(b). Thus, the conditions for a stationary Rydberg polariton in the medium are not satisfied. Indeed, we find that this is also true for all other ratios $\bar{\delta}/\Omega_s \neq 1$, as shown in Fig. 5.2(b). Thus, already a small deviation from the condition $\bar{\delta} = \Omega_s$, where one of the eigenstates of the subsystem $\{\hat{D}, \hat{S}\}$ is resonantly coupled, breaks the condition for the stationary Rydberg polariton. This observation is in accordance with the requirement to obey the EIT resonance.

Finally, we want to point out that in our level scheme the Rydberg state can also be coupled under Rydberg dressing conditions [154, 198–200], meaning $|\Delta_s| \gg \Omega_s$ and $\bar{\delta} = 0$. In this case, the dark-state has the form

$$\hat{\Psi}' = \frac{1}{\mathcal{N}'} \left[ \Omega \left( \hat{\mathcal{E}}_+ + \hat{\mathcal{E}}_- \right) - G \left( \hat{D} + \frac{\Omega_s}{\Delta_s} \hat{S} \right) \right] \tag{5.8}$$

[30] The case $\bar{\delta} = -\Omega_s$ can be treated analogously and also leads to one stationary Rydberg polariton in the system.

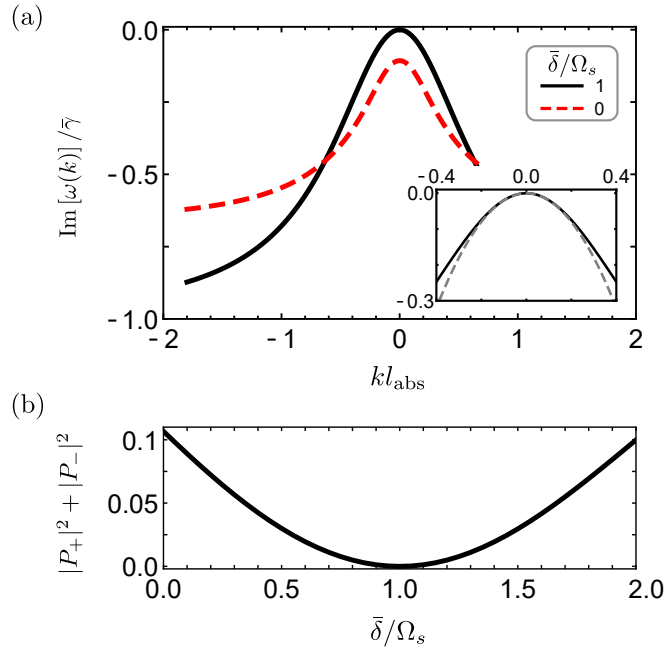


**Figure 5.2: Analysis of the level scheme for a stationary Rydberg polariton.** (a) Imaginary part of the dispersion relation $\mathrm{Im}\,[\omega(k)]\,/\bar{\gamma}$ as a function of the photon momentum $k$ scaled by the absorption length $l_{\mathrm{abs}} = c\bar{\gamma}/G^2$ [117]. The inset shows an enlargement of the plot for small photon momenta together with the approximate dispersion relation (gray dashed line) given by Eq. (5.7). (b) Probability $|P_+|^2 + |P_-|^2$ to be in one of the intermediate states as a function of $\bar{\delta}/\Omega_s$ for $k = 0$. Parameters for both plots are $\Omega_s/\gamma = \Omega/\gamma = G/\gamma = 1$. Figure and caption taken with permission from [98].

with normalization $\mathcal{N}' = \left[G^2(1 + \Omega_s^2/|\Delta_s|^2) + 2\Omega^2\right]^{1/2}$. Using the same analysis as above, we can show that also under Rydberg dressing conditions our scheme supports a stationary Rydberg polariton. Here, we obtain the same dispersion relation as for the genuine ground-state dual-V SLP [34, 117]. In contrast to the scheme above, the Rydberg component of the polariton is inherently small as $\Omega_s/|\Delta_s| \ll 1$ and can be tuned by this ratio.

In order to simplify the following discussion, we focus on the case of a resonant coupling to the Rydberg state. However, an analogous analysis can be performed under Rydberg dressing conditions.

## 5.2 Influence of a Rydberg impurity on the scheme

We now investigate how the interaction with a Rydberg impurity affects the system. In the simplest case, the interaction with the impurity can be modeled as a level shift $\hbar V$ of the Rydberg level. This shift can be taken into account by adding the term $iV\hat{S}$ into Eq. (5.4) [117]. In the previous section we have found that only for $|\bar{\delta}| = \Omega_s$, the conditions for a stationary Rydberg polariton are met.

Therefore, based on this simple picture, we expect that the conditions for the stationary Rydberg polariton are altered or even not fulfilled in the presence of the impurity.

In the following, we consider a specific situation where a Rydberg impurity is positioned at $z_0 = L/2$ in a medium of length $L$. This Rydberg impurity is assumed to be decoupled from the applied fields and interacts with the state $|r\rangle$ via van der Waals interactions $V_{\mathrm{vdW}} = V(z - z_0) = C_6/(z - z_0)^6$. Furthermore, we assume that the probe field is incident from the left onto the medium under continuous wave (cw) conditions. This allows us to treat the equation of motion, Eq. (5.5), in the stationary limit. It is known that if the conditions for a stationary Rydberg polariton in the medium are met, the probe field gets reflected from the medium with a certain probability [32, 151]. However, in the presence of the Rydberg impurity, we expect a finite probability to populate the intermediate states and thus partial absorption of the probe field. Therefore, the transmission and reflection properties of the medium can serve as a probe for the presence of an impurity in the medium[31].

In order to calculate these quantities, we first derive the propagation equations for the probe fields in the presence of the Rydberg impurity in Sec. 5.2.1. Afterwards, we investigate the transmission and reflection properties of the medium as a function of the interaction strength and relevant field parameters in Sec. 5.2.2.

### 5.2.1 Propagation equation for the probe fields[32]

In order to derive the propagation equation for the two probe fields $\hat{\mathcal{E}}_\pm$ for the situation described above, we start with the equations of motion, Eqs. (5.1) - (5.4). We account for the Rydberg impurity by extending these equations with a term that includes the interaction-induced shift $V_{\mathrm{vdW}}$. Moreover, we define the one-body wave function [24]

$$|\psi\rangle = \mathcal{E}_+\hat{\mathcal{E}}_+^\dagger|0\rangle + \mathcal{E}_-\hat{\mathcal{E}}_-^\dagger|0\rangle + P_+\hat{P}_+^\dagger|0\rangle + P_-\hat{P}_-^\dagger|0\rangle + D\hat{D}^\dagger|0\rangle + S\hat{S}^\dagger|0\rangle \tag{5.9}$$

inside the medium in the short-hand notation used above. Here, $\mathcal{E}_\pm = \langle 0|\hat{\mathcal{E}}_\pm|\psi\rangle$ are the probe field amplitudes with similar definitions for the other fields. Following the derivation in ref. [117] we can rewrite the equations of motion, Eqs. (5.1)-(5.4), in steady state as

$$0 = \mp c\partial_z\mathcal{E}_\pm - iGP_\pm\,, \tag{5.10}$$
$$0 = -iG\mathcal{E}_\pm - i\Omega D - \bar{\gamma}P_\pm\,, \tag{5.11}$$
$$0 = -i\Omega(P_+ + P_-) - i\Omega_s S - i\bar{\delta}D\,, \tag{5.12}$$
$$0 = -i\Omega_s D - i(\Delta_s + \bar{\delta} - V_{\mathrm{vdW}})S\,. \tag{5.13}$$

The last three equations, Eqs. (5.11)-(5.13) can be solved for the amplitudes $P_\pm$ of the polarization coherences. In this way, we can recast Eq. (5.10) in the form

[31] The two preceding paragraphs are taken verbatim from Tebben *et al.* [98] with minor adaptions for the ease of readability.

[32] Adapted from Tebben *et al.* [98].

of a propagation equation [98]

$$i\partial_z \mathbf{E}(z) = \mathbf{M}(z)\mathbf{E}(z) \tag{5.14}$$

with $\mathbf{E}(z) = \{\mathcal{E}_+(z), \mathcal{E}_-(z)\}$ and the propagation matrix [98]

$$\mathbf{M}(z) = \begin{pmatrix} \chi_{++}(z) & \chi_{+-}(z) \\ -\chi_{+-}(z) & -\chi_{++}(z) \end{pmatrix}. \tag{5.15}$$

Here, we have defined the susceptibilities [98]

$$\chi_{++}(z) = \frac{-iG^2}{c\bar{\gamma}} \frac{(V_{\mathrm{vdW}} - \delta_r)(\bar{\gamma}\bar{\delta} - i\Omega^2) + \bar{\gamma}\Omega_s^2}{(V_{\mathrm{vdW}} - \delta_r)(\bar{\gamma}\bar{\delta} - 2i\Omega^2) + \bar{\gamma}\Omega_s^2}, \tag{5.16}$$

$$\chi_{+-}(z) = \frac{G^2}{c\bar{\gamma}} \frac{(V_{\mathrm{vdW}} - \delta_r)\Omega^2}{(V_{\mathrm{vdW}} - \delta_r)(\bar{\gamma}\bar{\delta} - 2i\Omega^2) + \bar{\gamma}\Omega_s^2}, \tag{5.17}$$

where $\delta_r = \bar{\delta} + \Delta_s$. In the absence of the Rydberg coupling field $\Omega_s = 0$ and on two-photon resonance $\bar{\delta} = 0$, the propagation matrix reduces to

$$\mathbf{M}_{\mathrm{SLP}}(z) = \begin{pmatrix} \chi_0 & -\chi_0 \\ \chi_0 & -\chi_0 \end{pmatrix} \tag{5.18}$$

with $\chi_0 = \chi_{++}(z) = -\chi_{+-}(z) = -iG^2/(2c\bar{\gamma})$. Here, the balanced coupling between the counter-propagating probe field modes leads to the ordinary dual-V SLP [34, 117]. In the presence of the Rydberg impurity, the susceptibilities describe effective potentials for and the coupling between the two probe field modes [98].

### 5.2.2 Transmission and reflection properties in the presence of a Rydberg impurity

In this section we investigate the transmission and reflection properties of the medium hosting a Rydberg impurity. We first, derive and examine the solution of the propagation equation, Eq. (5.14). Afterwards, we discuss the resulting transmission and reflection probabilities as a function of the interaction strength and relevant field parameters.

#### Solution of the propagation equation

The propagation equation for the probe fields, Eq. (5.14), in the presence of the Rydberg impurity has the formal solution

$$\mathbf{E}(z) = \exp\left[\int_0^z -i\mathbf{M}(z')\mathrm{d}z'\right] \begin{pmatrix} C_1 \\ C_2 \end{pmatrix}, \tag{5.19}$$

where $C_{1,2}$ are integration constants and $z_0$ is the position of the stored Rydberg excitation. We assume that the probe field is incident from the left onto the medium. Thus, using the boundary conditions [98]

$$\mathcal{E}_+(z = 0) = \mathcal{E}_0, \tag{5.20}$$

$$\mathcal{E}_-(z = L) = 0, \tag{5.21}$$

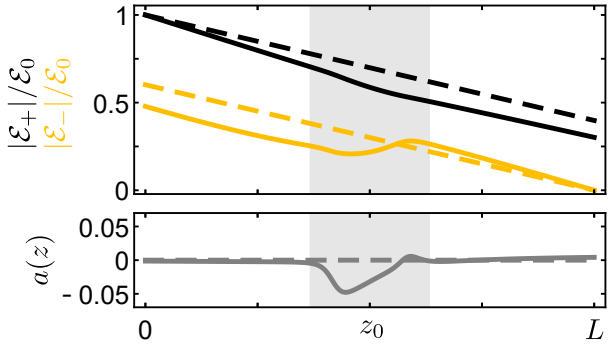


**Figure 5.3: Solution of the propagation equation for the probe fields.** In the upper graph, the two probe field amplitudes $|\mathcal{E}_\pm|/\mathcal{E}_0$ are plotted as a function of position in a medium of length $L$ in the absence (dashed lines) and presence (solid lines) of a Rydberg excitation at position $z_0$. The lower graph shows the quantity $a(z)$ as explained in the main text. The gray shaded area highlights the spatial region, where the solutions for the probe fields modes are affected by the Rydberg impurity. Parameters are $\bar{\delta} = -\Omega_s = \gamma$, $\Omega/\Omega_s = 0.5$, $\Delta_s = 0$ and $C_6/2\pi = 138.9\,\mathrm{GHz}\mu\mathrm{m}^6$ of the $^{87}$Rb $60S$ Rydberg state in a medium with an optical depth of 3.

where $L$ is the medium length, yields the integration constants

$$\begin{pmatrix} C_1 \\ C_2 \end{pmatrix} = \begin{pmatrix} \mathcal{E}_0 \\ \dfrac{-(1-m)\,\mathcal{E}_0 m_{+-}}{(1-m)\,m_{++} + (1+m)\left(m_{++}^2 + m_{+-}^2\right)^{1/2}} \end{pmatrix} \tag{5.22}$$

with

$$m_{++} = -i\int_0^L \chi_{++}(z')\mathrm{d}z'\,, \tag{5.23}$$

$$m_{+-} = -i\int_0^L \chi_{+-}(z')\mathrm{d}z'\,, \tag{5.24}$$

$$m = \exp\left[2\left(m_{++}^2 + m_{+-}^2\right)^{1/2}\right]. \tag{5.25}$$

Fig. 5.3 shows exemplarily the solution of the propagation Eq. (5.19) for the two probe field amplitudes $\mathcal{E}_\pm(z)$ in the absence (dashed lines) and presence (solid lines) of the Rydberg impurity. Hereby, we assume a resonant coupling to the Rydberg state and $|\bar{\delta}| = \Omega_s$. In the absence of the impurity, stationary light conditions imply that the right-moving field $\mathcal{E}_+(z)$ gets depopulated to the benefit of the left-moving field $\mathcal{E}_-(z)$. In the continuous wave limit, this means that the two amplitudes are linear functions of $z$ with respect to the imposed boundary conditions, Eqs. (5.20) and (5.21), as shown in the upper graph of Fig. 5.3. The sum of transmission $T$ and reflection $R$ coefficients defined as [98, 117]

$$T = \frac{|\mathcal{E}_+(z=L)|}{|\mathcal{E}_0|} \quad \text{and} \quad R = \frac{|\mathcal{E}_-(z=0)|}{|\mathcal{E}_0|} \tag{5.26}$$

equals unity, reflecting energy conservation. We note that a longer propagation length $L$ or a larger atomic density $\rho_0$ result in a larger reflection coefficient, as the left-moving field gets increasingly populated. Consequently, the slopes of the linear curves in the upper graph of Fig. 5.3 are determined by the optical depth of the medium.

In the presence of the Rydberg impurity, a deviation of the field amplitudes from the previous situation is apparent and $T + R$ no longer equals unity. In order to quantify the emerging losses and the difference compared to the situation without the impurity, we define and plot the quantity

$$a(z) = \frac{\partial_z |\mathcal{E}_+(z)|}{|\mathcal{E}_0|} + \frac{\partial_z |\mathcal{E}_-(L-z)|}{|\mathcal{E}_0|} \tag{5.27}$$

in the lower panel of Fig. 5.3. In the absence of the impurity this quantity equals zero, as shown by the gray dashed line. In the presence of the impurity (solid gray line), it vanishes in the regions far apart from the impurity. However, $a(z)$ is strongly altered in the vicinity of the excitation. The total absorption induced by the Rydberg impurity is given by the absorption coefficient

$$A = 1 - T - R = \left| \int_0^L \mathrm{d}z' a(z') \right| , \tag{5.28}$$

which could be observed experimentally.

### Dependence of transmission properties on the interaction and coupling strengths[33]

Next, we investigate how the transmission, reflection, and absorption coefficients change, when interactions are gradually increased. For this purpose, we vary the quantum number $n$ of the Rydberg state in which the Rydberg impurity resides. The result is shown in Fig. 5.4(a). For increasing interaction strength, absorption of the probe field increases at the cost of both transmission and reflection probabilities. This is due to the fact that stronger interactions imply a larger level shift. As a consequence, the probability to populate the intermediate states and thus absorption of the probe field is increased.

In Fig. 5.4(b) we explore for $n = 60$ how the amount of interaction-induced absorption depends on system parameters such as the Rabi frequency of the control field and the Rydberg coupling strength. For vanishing ratios $\Omega/\Omega_s = 0$, the system reduces to a two-level system with transmission and absorption coefficients given by the optical depth of the medium. For ratios $\Omega/\Omega_s \gg 1$, absorption goes to zero, while the transmission and reflection coefficients approach the values of the corresponding non-interacting system under stationary Rydberg polariton conditions. This is due to the fact that the EIT linewidth $\Omega/\gamma$ is large compared to the interaction strength, such that the system becomes insensitive to interactions. For small ratios $\Omega/\Omega_s$ the situation is reversed. Here, the EIT linewidth is small such the system is very sensitive to interactions and displays strong absorption

[33] Taken verbatim from Tebben *et al.* [98] with minor adaptions for the ease of readability.

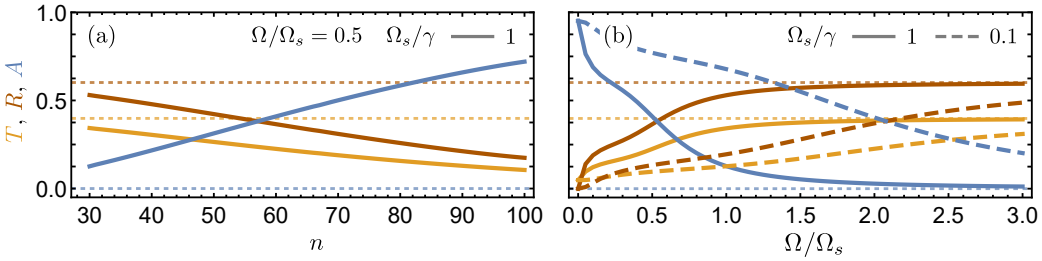


**Figure 5.4: Transmission properties in the presence of a Rydberg impurity.** Transmission $T$, reflection $R$, and absorption $A$ of the probe field as a function of (a) the Rydberg quantum number $n$ and (b) the ratio $\Omega/\Omega_s$ for $n = 60$ for the parameters as indicated in the figure. Other parameters are $\bar{\delta}/\Omega_s = 1$, $\Delta_s = 0$, $L = 40\,\mu$m and an optical depth of 3. Moreover, we consider coupling and interaction strengths for $^{87}$Rb atoms as discussed in Sec. 5.3. Horizontal dotted lines show the expected reflection, transmission and absorption probabilities (from top to bottom) in the absence of the impurity, respectively. Figure and caption taken and adapted with permission from [98].

.

of the probe field. Finally, for a given ratio $\Omega/\Omega_s$ we observe that the effect of an interaction-induced energy shift is increased for smaller ratios of $\Omega_s/\gamma$. This is a consequence of an increased atomic part of the polariton and thus a larger probability to populate the Rydberg state.

## 5.3 Considerations for an experimental implementation

In this section we discuss considerations for an experimental implementation of stationary Rydberg polaritons. First, we present suitable levels in $^{87}$Rb atoms for the realization of the scheme presented in Fig. 5.1. Afterwards, we discuss possible experimental sequences for creating the polaritons. Finally, we briefly comment on the lifetime of the polaritons as it sets a limitation on the available interaction time between the stationary Rydberg polaritons.

### Level scheme for $^{87}$Rb atoms[34]

The level scheme presented in Fig. 5.1(b) can for example be realized in a gas of $^{87}$Rb atoms, similar to ref. [117]. Here, the two ground states

$$|g\rangle = |5S_{1/2}, F = 1, m_F = 0\rangle \tag{5.29}$$

$$|d\rangle = |5S_{1/2}, F = 2, m_F = 0\rangle \tag{5.30}$$

as well as the intermediate states $|e_\pm\rangle = |5P_{3/2}, F = 1, m_F = \pm 1\rangle$, with decay rate $\gamma/2\pi \sim 6\,$MHz, are suitable. The circular polarizations of the probe field and the counter-propagating control fields, have to be chosen accordingly. The coupling to

[34] Taken verbatim from Tebben *et al.* [98] with minor adaptions for the ease of readability.

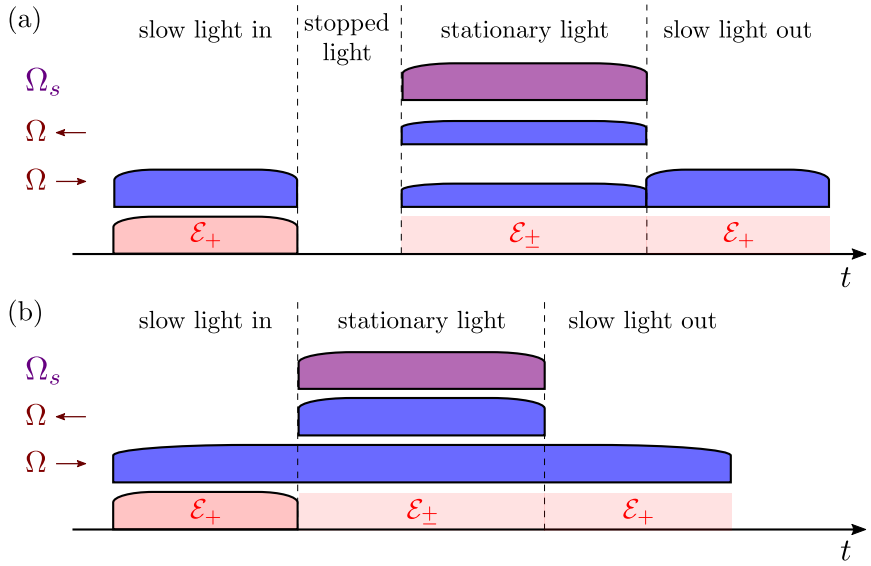


**Figure 5.5: Sequences for the creation of stationary Rydberg polaritons.** Stationary Rydberg polaritons can either be created from (a) a stored spin wave, termed as "stopped light" in the figure, or (b) directly from propagating slow-light polaritons. In both schemes, the Rydberg character of the polaritons is imposed by turning on the Rydberg coupling laser with Rabi frequency $\Omega_s$. Framed bars indicate applied pulses while light shaded areas illustrate probe field modes present in the medium. For details see the main text.

.

a Rydberg state $|r\rangle = |nS_{1/2}, J = 1/2, m_J = 1/2\rangle$ is possible with the help of a far detuned, two-photon transition, e.g. via an intermediate state in the $5P_{3/2}, F = 3$ hyperfine manifold. Coupling strengths used for the control and Rydberg coupling fields in Fig. 5.4, especially for small ratios of $\Omega_s/\gamma$, are experimentally accessible.

### Experimental sequence

In Sec. 5.2 we have discussed that a Rydberg impurity in the medium leads to a sizable absorption of the involved probe field [98]. An experimental realization of such a scenario involves two steps: First, Rydberg excitations need to be excited in the medium, e.g. via an off-resonant two-photon excitation. Second, the two control field pulses and the probe field pulse have to be turned on at the same time. Transmission and reflection of the probe field could then be recorded and would provide information on the absence and presence of Rydberg impurities in the medium. This procedure could offer a complementary approach [98] to the method of interaction enhanced imaging [67].

Detached from this impurity scenario and the previous discussion in the steady-state limit, we now consider how stationary Rydberg polaritons could be created inside the medium. This involves time-dependent control and Rydberg coupling fields. After creation of the polaritons inside the medium, interactions between

the polaritons themselves could be studied.

Experimental sequences for this purpose can build on known sequences for the creation of stationary light polaritons. There, two different sequences have been used so far: Historically, in the first experimental demonstration of stationary light the idea to retrieve a stored spin wave not only with one control field, but with two counter-propagating control fields was used [32]. While the first scenario gives rise to slow light, the second creates stationary light. Therefore, the first possible sequence starts by letting photons propagate into the medium as slow-light polaritons, where they are stored as a spin wave (stopped light), as illustrated in Fig. 5.5(a). Subsequent retrieval of the spin wave by turning on both control fields simultaneously allows to generate stationary light polaritons. After a variable hold time they can be released from the medium by turning off one of the control fields. This sequence is most frequently used in stationary light experiments [32, 35, 36, 43, 92, 201–203].

The second possible sequence creates stationary light polaritons directly from propagating slow-light polaritons [202], as schematically depicted in Fig. 5.5(b). Here, a probe field pulse of finite duration is sent into the medium in the presence of the co-propagating control field. When turning on the second control field, the slow-light polaritons are converted into stationary polaritons. Again, the stationary light polaritons can be released from the medium as slow-light polaritons by turning off one of the control fields. Both sequences could be extended by a Rydberg coupling pulse during the stationary light phase for creating stationary Rydberg polaritons, as indicated in Fig. 5.5.

### Lifetime of the polariton

For stationary light polaritons it is known that a limited optical depth of the medium leads to diffusion and thus to an effective lifetime of the SLP [42, 92, 114, 119]. Resulting from the propagation equation of the stationary light polariton one obtains the diffusion constant $D = v_g l_{\mathrm{abs}}$ [42, 119] (see also Sec. 2.2.3), where $v_g = 2c\Omega^2/(G^2 + 2\Omega^2)$. Moreover, $l_{\mathrm{abs}} = c\bar{\gamma}/G^2 = L/\mathrm{OD}$ denotes the absorption length of the medium with optical depth OD and length $L$. As the considered stationary Rydberg polariton obeys formally the same dispersion relation as the SLP [98], this diffusive process is expected to be likewise present for the stationary Rydberg polariton and thus limits the available interaction time. The most obvious approach to reduce diffusion and thus to extend the lifetime of the polariton is to increase the optical depth OD. The optical depth does not only depend on the atomic density, but also on the coupling strength of the probe field transitions and the decay rate of the intermediate states. Therefore, a proper choice of the atomic species, i.e. with a short intermediate state lifetime such as available in Strontium atoms, and of the atomic states, i.e. with a large coupling strength of the probe transition, is beneficial. Nevertheless, the available optical depth is typically limited[35] in experimental setups. Therefore, we briefly discuss a possible

[35] A rather large optical depth can be obtained in atomic clouds confined in a MOT due to the long propagation distance. This is the reason, why previous experimental investigations of stationary light have mainly been performed in such a setting [35, 36, 43, 92, 202, 203].

approach [42, 119] to extend the lifetime of the polaritons under the condition of a limited optical depth. In this regard, we recall that the polaritons first propagate as slow-light polaritons into the medium before they are converted to stationary light polaritons, as discussed in the previous section.

In order to keep the diffusion constant small for a finite OD, $v_g$ could be reduced. As outlined in Sec. 2.1.4 this reduction can be achieved by a smaller Rabi frequency of the control field. However, then the EIT transparency window, which is proportional to $\Omega^2$, is also reduced. As the initial width of the probe pulse needs to fit into the transparency window in order to avoid absorption, a reduction of the Rabi frequency $\Omega$ immediately leads to strong constraints on the spectral width of the probe pulse. This predicament can be relaxed by using different Rabi frequencies of the control field for the slow-light and stationary-light phases, respectively, as it has been used in refs. [42, 119]. Fig. 5.5(a) schematically illustrates this idea. Starting with a large value of $\Omega$ results in a large transparency window for the slow-light polaritons, while a smaller Rabi frequency reduces the diffusion process for the stationary light polariton. Nevertheless, a smaller value of $\Omega$ also reduces the photonic component of the stationary Rydberg polariton, which is evident from Eq. (5.6). Therefore, a trade-off for the Rabi frequency $\Omega$ of the control fields needs to be found. Investigating the parameter space in this regard and developing other ideas for increasing the lifetime of the polariton would certainly be beneficial for future experimental investigations.

## 5.4 Summary and discussion

In this chapter we have proposed a novel scheme for coupling a Rydberg state to a stationary light polariton [98]. A dual-V level scheme for stationary light polaritons constitutes the basis for our proposal [34, 44] for the following two reasons: First, it supports stationary photonic excitations in cold atom experiments [34, 37] as compared, for example, to a $\Lambda$-level scheme (see Sec. 2.1.5). Second, it simplifies phase matching in an experimental realization. This is important as a phase mismatch could lead to a decay of the polariton [92] and therefore limit the available interaction time [98]. Our scheme involves to couple the second ground state of the dual-V scheme to a Rydberg state. Depending on the particular choice of the strengths and detunings of the involved light fields, this coupling can either be realized under Rydberg dressing conditions or with a resonant coupling to the Rydberg state [98]. As both coupling schemes can be analyzed in a similar manner, we have focused on the case of a resonant coupling to the Rydberg state in the present chapter.

The stationary nature of the polariton in the dual-V scheme might not be maintained once a Rydberg state is added to the system. Indeed, we have found that our scheme only supports a stationary excitation if the detuning of the control field compensates the light shift induced by the Rydberg coupling field [98]. Under this condition we have shown that the polariton possesses a quadratic dispersion relation and a form, which both directly relate to that of the underlying dual-V SLP [34]. Therefore, our proposed scheme supports what we call a stationary Rydberg

polariton [98].

In order to investigate the influence of interactions in this scheme, we have considered the effect of a Rydberg impurity on the system [98]. Already for small interaction-induced level shifts, we have found imperfect conditions for the creation of the stationary Rydberg polariton. Here, we have investigated how experimental observables, such as the transmission of the probe field, are affected by the presence of the impurity. For this purpose, we have derived the propagation equation for the two counter-propagating probe field modes. By solving this equation, we have shown that the presence of the impurity results in an observable change of the transmission, reflection and absorption properties of the probe field [98]. This effect could be exploited for probing the presence of a Rydberg impurity in the medium [98], which could provide a complementary approach to interaction enhanced imaging [67].

Finally, we have considered an experimental realization of the stationary Rydberg polariton. Here, we have suggested a possible level scheme in Rubidium atoms together with experimental sequences for the creation of the polariton. Moreover, we have discussed the lifetime of the polariton.

Our investigation has been driven by the quest for enhanced photon-photon interactions. On the one hand, increasing the interaction strength between polaritons is one approach towards this goal. On the other hand, the polaritons could be realized as stationary excitations in the atomic medium. In this way, the interaction time could be increased compared to the propagating case and thus lead to enhanced photon-photon interactions. It was this idea that has motivated us to develop a novel scheme to enable interactions between stationary light polaritons. Nevertheless, our studies on the stationary Rydberg polariton only mark the starting point for further investigations.

First, the possible extension of the interaction time compared to the propagating case needs to be quantified. We have provided first qualitative thoughts in this direction. Here, the effective lifetime of the stationary Rydberg polariton could be obtained by solving the time-dependent equations of motion numerically [42].

Second, we have studied the effect of interactions on our scheme only in their simplest manifestation, meaning in terms of a level shift originating from the interaction with a Rydberg impurity [98]. Extending our work to interactions between stationary Rydberg polaritons themselves, would open the possibility for investigating systems of interacting polaritons with an increased interaction time [98]. We suspect that two stationary Rydberg polaritons with a resonant coupling to the Rydberg state would yield interactions in the order of the Rydberg coupling strength $\Omega_s$ [98]. On the contrary, under Rydberg dressing conditions, we expect the interactions to scale as $\Omega_s^4/\Delta_s^3$, in accordance with the scaling found for Rydberg-dressed ground state atoms [154, 198]. Here, $\Delta_s$ is the detuning of the light field that provides the coupling to the Rydberg state. Since Rydberg dressing requires $\Omega_s/\Delta_s \ll 1$, these interactions between the polaritons would be perturbative to the system [98].

Both experimentally and theoretically it might be interesting to first study the perturbative regime in order to develop an understanding of the interactions between the stationary Rydberg polaritons. Afterwards, one could proceed by

exploring the system under a resonant coupling to the Rydberg state. A theoretical model for the interaction between two stationary Rydberg polaritons could build on existing theories that consider the interaction between two propagating polaritons, as e.g. presented in refs. [6, 24, 115].

Finally, we want to discuss three possible applications of our scheme. Recently, the thermalization of Rydberg polaritons in two dimensions has been observed experimentally in the weakly interacting regime [197]. Here, Rydberg interactions allowed for thermalizing collisions between the polaritons. However, a Bose-Einstein condensate (BEC) was not achieved, as the Rydberg polaritons were still traveling with a reduced group velocity through the atomic medium. As a consequence, thermalization was only possible in the two dimensions transversal to the propagation direction of the involved fields [197]. As suggested by the authors of that work, using Rydberg polaritons that are stationary in the medium would allow for the creation of a polariton BEC in three dimensions. Our scheme could provide such a possibility. A condensate of stationary Rydberg polaritons would differ from previously observed photon BECs [204, 205] in dimensionality. Moreover, collisions induced by a Kerr-type nonlinearity have been proposed to enable a BEC of stationary light polaritons [44]. For the case of stationary Rydberg polaritons, the collisions would be caused by Rydberg interactions, as also discussed in ref. [197].

Stationary Rydberg polaritons as proposed here, could also be utilized to investigate correlated photon dynamics in two dimensions. Here, a two-dimensional medium would accommodate many polaritons in the transversal plane with respect to the propagation direction of the probe field. Slow-light polaritons propagating into the medium could subsequently be converted into stationary light polaritons with the procedures discussed in Sec. 5.3. Interactions could then be imposed with the help of our scheme, whereby the emergence of spatial correlations is expected. The system could be probed after a variable interaction time, which is limited by the lifetime of the stationary Rydberg polariton in the medium. Afterwards, the photons could be retrieved as slow-light polaritons. In such a system a signature of interactions between the polaritons could be observed in the emergence of a blockade effect in the transverse direction.

Finally, the crystallization of single photons has been proposed in a system of propagating Rydberg polaritons [6]. Here, true long-range order could be achieved by either applying an external lattice potential for the polaritons or based on a storage technique. Furthermore, the authors of that work suggested that utilizing stationary light polaritons could enable long-range order without an external potential. Therefore, it would be interesting to apply a similar analysis as the one in ref. [6] to our scheme and explore if stationary Rydberg polaritons could exhibit crystalline order.

CHAPTER 6

# Conclusion

Central to the field of Rydberg EIT, we have raised three questions in the introduction of this thesis: (i) *How to model the strongly interacting and thus strongly correlated light-matter system under Rydberg EIT conditions?*, (ii) *How to experimentally test these models?* and (iii) *How to enhance photon-photon interactions?* This thesis provides first answers to these questions, which we summarize in the following.

Regarding the first question (i) it is of particular importance which assumptions are made in order to reduce the complexity of the driven many-body system under Rydberg EIT conditions. On the one hand, this concerns the treatment of interaction-induced correlations in the system. On the other hand, assumptions, such as an adiabatic elimination of the intermediate state in a three-level system [58, 154], typically restrict the parameter space in which the resulting model is applicable.

In this thesis, we have investigated the nonlinear optical response of a Rydberg EIT medium on two-photon resonance. Thereby, we have considered atomic correlations exactly up to the second order and have dropped an adiabatic elimination of the intermediate state. As a result, we have demonstrated that an enhanced nonlinear response of a Rydberg gas under EIT conditions emerges from a two-body, two-photon resonance [96]. Indeed, this resonance is only revealed if the dynamics of the intermediate state is explicitly taken into account. Associated to the resonantly enhanced response is a nonlinear susceptibility that can be tuned by experimental parameters, such as the Rabi frequency of the control field and the atomic density [96]. We have developed an intuitive picture that explains the resonance based on laser-dressed atomic pair-states, and that is capable of explaining spatial features of the nonlinear susceptibility [96].

The intuitive picture and the resonance feature immediately relate to other resonance effects that have been predicted for atomic properties of the Rydberg EIT medium in the semiclassical regime [79, 126, 127]. Interestingly, also on the single-photon level, a similar resonance effect has been reported [144]. Our work complements this finding in the quantum regime with a semiclassical analysis of the resonance effect [96].

We have found an answer to the second question (ii) by discovering a novel and rigorous way to experimentally test theoretical models in the semiclassical regime [97]. For this purpose, we have extended the experimental study of Rydberg EIT with classical light fields into the regime on two-photon resonance. Here, the linear response of the Rydberg EIT medium vanishes in the non-interacting case, allowing us to probe only nonlinear effects [97]. In particular, we have compared our experimental results with the predictions based on a mean-field model [60, 64, 65, 80], a Monte-Carlo rate equation (MCRE) model [78, 81–83], and our theory based on a pairwise treatment of interactions [96, 121]. Our measurements with the control beam on resonance are comparable to previous experimental studies [23, 62, 64, 65]. However, following our new approach, we have observed qualitative discrepancies between theoretical predictions and a measured absorption feature on two-photon resonance [97]. Therefore, the development of improved models beyond those mentioned above and complementary measurements are required to obtain a complete understanding of the driven many-body dynamics under Rydberg EIT conditions [97].

This brings us back to the question of how to model the Rydberg EIT system. Considering the assumptions entering into the different theories, it is of central importance how atomic correlation are included in these models. In particular, neglecting them, only taking them into account approximately, or treating them exactly on a pairwise basis seems not to be sufficient for describing our experimental results. Therefore, improved theories that include atomic correlations up to a higher order would be very beneficial [97]. For example, our low-intensity theory, which models the two-body, two-photon resonance, could be extended to larger atomic clusters.

Further experimental investigations will complement these theoretical efforts. Here, we emphasize that our work constitutes the first experimental investigation of Rydberg EIT with classical light fields on two-photon resonance. Therefore, it will be an interesting task for future studies to thoroughly characterize the observed absorption feature. Moreover, measurements on two-photon resonance will certainly serve as a benchmark for improved theories, which underlines the importance of our new method to test semiclassical models of Rydberg EIT.

Objective of the last question (iii) is the enhancement of photon-photon interactions. In Rydberg EIT systems these interactions are enabled by interacting Rydberg polaritons. One limitation for the interaction between two Rydberg polaritons is the available interaction time, which is given by the time the polaritons travel along each other through the Rydberg EIT medium [85, 197]. We have addressed this point with the idea of introducing interactions between stationary photonic excitations. In this regard, we have proposed a novel scheme that endows a stationary light polariton with a Rydberg character, leading to what we call a stationary Rydberg polariton [98].

We have analyzed this scheme in detail in the non-interacting regime. Here, we have identified two different parameter regimes that permit the creation of a stationary Rydberg polariton. While one regime exploits Rydberg dressing conditions, the other one involves a resonant coupling to the Rydberg state [98]. Furthermore, we have studied the effect of interactions on our scheme. We have

found that in the presence of a Rydberg impurity the involved probe field gets strongly absorbed.

It remains an interesting task for future investigations to extend our study to the interaction between stationary Rydberg polaritons themselves, and to quantify to which extend the interaction time between the stationary Rydberg polaritons could be increased compared to the propagating case. Finally, our scheme might find applications for the creation of exotic states of light, such as a photonic Bose-Einstein condensate [197] and crystalline states of light [6].

In summary, this thesis has theoretically and experimentally extended the field of Rydberg EIT with classical light fields on two-photon resonance. Here, the linear response of the atomic medium vanishes and resonance effects emerge. Moreover, a novel scheme for a stationary Rydberg polariton has been proposed. This opens the perspective for realizing interactions between stationary photonic excitations. Exploring the field of Rydberg EIT in these two directions will provide new insights into the nonlinear optical response of a strongly interacting many-body system. Furthermore, it will deepen our understanding on what we encounter in our everyday life and what has fascinated mankind ever since – light.

APPENDIX A

# Experimental details

This appendix complements the experimental investigations reported in Chap. 4. A determination of the detection and quantum efficiency as well as of the gain of the CCD camera are presented in App. A.1. A characterization of the focused probe beam in terms of its beam profile and positional stability follows in App. A.2.

## A.1 Detection efficiency of the CCD camera

We use an Andor iXon Ultra 897 EM-CCD camera [206] for transmission measurements, and for the determination of the Rabi frequency of the probe beam [121] as outlined in Sec. 4.1.3. For this purpose, knowledge of the detection efficiency $q$ of the CCD camera is necessary. It relates [102] the measured mean number of counts $\langle n_c \rangle$ per pixel to the mean number of incident photons $\langle n_{ph} \rangle$ via

$$\langle n_c \rangle = q \langle n_{ph} \rangle = \eta g \langle n_{ph} \rangle \,. \tag{A.1}$$

The detection efficiency is composed of the quantum efficiency $\eta$ and the gain $g = \langle n_c \rangle / \langle n_e \rangle$ of the CCD camera. Here, $\langle n_e \rangle$ is the mean number of generated electrons. In order to determine the detection efficiency $q$, we illuminate the CCD camera with a focused laser beam for an exposure time of $t_{\mathrm{exp}} = 5\,\mu\mathrm{s}$, and measure the mean number of total counts on the CCD camera. For this purpose, we use a beam with a power of $P = (97 \pm 4)\,\mathrm{nW}$, a waist of $15\,\mu\mathrm{m}$, and a frequency of $\nu = c/780\,\mathrm{nm}$. Using Eq. (A.1) with $\langle n_{ph} \rangle = P/(h\nu) t_{\mathrm{exp}}$, we obtain $q = 0.47 \pm 0.02$. Here, the error results from the uncertainty in the measured beam power.

In the following, for completeness, we determine[36] the gain $g$ by measuring a photon transfer curve [207]. Based on this quantity and on Eq. (A.1), the quantum efficiency $\eta$ of the CCD camera can be calculated.

The detection of photons on a CCD camera is prone to several noise sources. Typical sources for noise include read noise, shot-noise, which follows a Poisson

[36] Ref. [207] provides a very detailed review of how to characterize CCD cameras with uniform illumination. The procedures described therein could be used for a precise and complete characterization of the CCD camera.

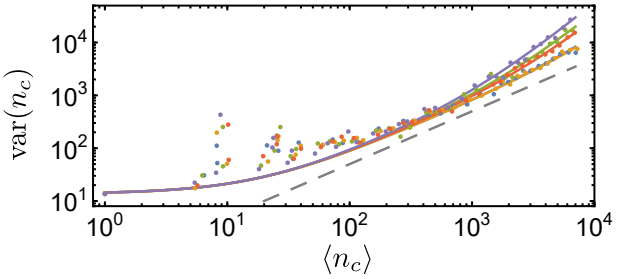


**Figure A.1: Gain determination.** Variance $\mathrm{var}(n_c)$ of the camera counts against the mean counts $\langle n_c \rangle$. A simultaneous fit of Eq. (A.3) to the data (solid lines) allows us to extract the gain setting of our CCD camera as outlined in the main text. The gray dashed line has a slope of one and indicates the shot noise dominated regime.

distribution, intensity noise, which is proportional to the beam intensity, and fixed pattern noise (see for instance refs. [102, 121, 208] for details on the different noise sources)[37]. A photon transfer curve relates the measured signal to its variance. For the measured electron signal this yields

$$\mathrm{var}(n_e) = r^2 + \sigma^2_{\mathrm{shot}} + a^2 \langle n_e \rangle^2 \,, \tag{A.2}$$

where $r$ is the read noise in electrons and $\sigma^2_{\mathrm{shot}} = \langle n_e \rangle$ the shot noise. The last term proportional to $\langle n_e \rangle^2$ combines noise sources such as intensity and fixed pattern noise. The variance of the electron signal can be related to the variance of counts $\mathrm{var}(n_c) = g^2 \mathrm{var}(n_e)$ on the CCD camera. As a result,

$$\mathrm{var}(n_c) = g^2 r^2 + g \langle n_c \rangle + a^2 \langle n_c \rangle^2 \tag{A.3}$$

follows from Eq. (A.2)[38].

Fig. A.1 shows a measurement of the variance $\mathrm{var}(n_c)$ against the mean number of counts $\langle n_c \rangle$ evaluated for five individual pixels in the center of the focused probe beam. For each data point, 100 images have been taken and averaged. The data point on the very left is obtained from images without the probe beam. Therefore, it provides the offset $g^2 r^2 = 13.73 \pm 0.06$. For convenience, we plotted this data point at $\langle n_c \rangle = 1$. At a low number of counts the variance sill fluctuates. This could have been avoided by taking more averages. For intermediate $\langle n_c \rangle$, the curves follow a slope of unity (indicated by the gray dashed line in Fig. A.1), which marks the shot noise dominated region. For high $\langle n_c \rangle$, noise sources quadratic in the mean number of counts dominate.

We fit Eq. (A.3) simultaneously to all curves. Hereby, we fix $g^2 r^2$ to the measured values stated above, impose $g$ to be the same for all curves, but leave $a$ as an individual fit parameter for each curve. The resulting best fitting curves are

[37] In the following, we assume that other noise sources, such as the analog-to-digital conversion of the signal, are negligible.

[38] Eq. (A.2) and (A.3) are adapted from ref. [207–209] in order to obtain the simplified model presented in this section.

shown as solid lines in Fig. A.1. We obtain a gain of $g = 0.75 \pm 0.05$ and values for $a$ that vary between $(0.75 \pm 0.07) \times 10^{-2}$ and $(2.24 \pm 0.03) \times 10^{-2}$. The result for the term proportional to $\langle n_c \rangle^2$ is comparable to the intensity noise of $(0.96 \pm 0.02) \times 10^{-2}$, obtained from the images. Moreover, using the extracted gain $g$, we calculate a read noise in electrons of $r = 4.9 \pm 0.3$. This value is in agreement with the specifications of the camera supplier, which amounts to 5.3 electrons at a readout rate of 1 MHz [206]. Finally, from the gain $g$ and the detection efficiency $q$, the quantum efficiency $\eta$ of the CCD camera can be calculated using Eq.(A.1), yielding $0.62 \pm 0.06$. This value is in agreement with the specified value of about 70% [206].

## A.2 Characterization of the focused probe beam

In Sec. 4.2.2 we presented the implementation of a focused probe beam into the experimental setup in order to ensure a geometry where dispersion is minimized. In terms of the beam profile, a ring structure is apparent around the beam. In this appendix, we characterize this ring structure in App. A.2.1. Thereby, we confirm that the measurement on two-photon resonance at a ratio $\Omega_p/\Omega_c \approx 0.05$ of the Rabi frequencies, presented in Fig. 4.15, is not affected by its presence. Furthermore, we examine the positional stability of the focused probe beam in App. A.2.2.

### A.2.1 Beam profile

In Fig. 4.8 (a) faint ring structure around the focused probe beam is apparent, which becomes more visible for higher intensities of the probe beam. Possible origins of the ring might be aberrations of the optical setup or a non-paraxial propagation of the beam [210, 211]. Experimentally we were not able to suppress this structure, e.g. by using lenses of different materials, focal lengths and diameters, or by exchanging other optical components such as the fiber out-coupler.

On the one hand, the ring could possibly affect the transmission determined from the intensity in the center of the probe beam if dispersive effects focus it inwards. On the other hand, atoms illuminated by the ring could induce a nonlinear behavior if the intensity in the ring is too high. In the following, we therefore characterize the ring structure in detail against the background of a possible influence on our measurements of nonlinear absorption in Rydberg EIT.

First, we determine the radius of the ring and investigate whether it is prone to any dispersive effects. For this purpose, we consider the Autler-Townes measurements presented in Fig. 4.14. We have confirmed that the measurements on two-photon resonance possess the same features. In Fig. A.2 the radial profile of the Rabi frequency of the probe beam is shown in the absence and presence of atoms for $\Delta_p = 0$. The profile is determined from the counts on the CCD camera using Eqs. (4.4) and (2.5). At a distance $d$ of about $28\,\mu$m a local maximum indicates the ring. We extract the radius of the ring with a polynomial fit to the radial profile. The results for the exemplary shown profiles are depicted in the

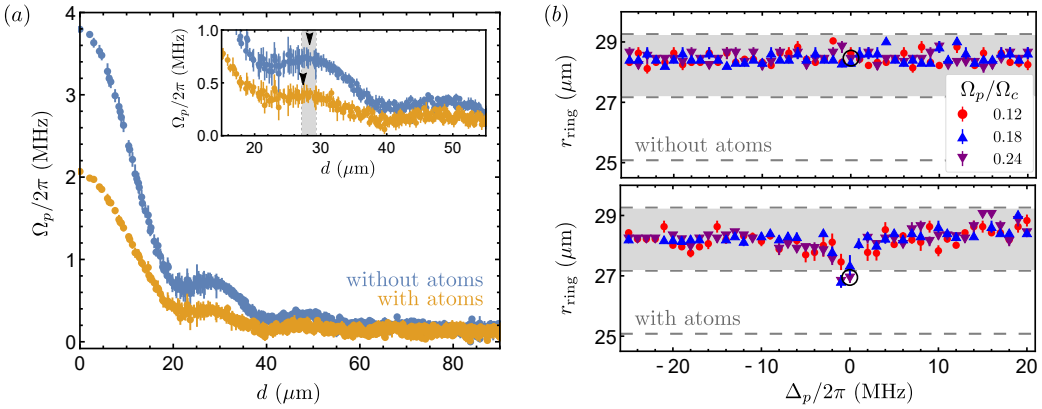


**Figure A.2: Radial profile of the Rabi frequency $\Omega_p$ and radius of the ring.** (a) Radial profile of the Rabi frequency $\Omega_p$ of the probe beam in the absence (blue) and presence (orange) of the atoms. The inset shows an enlargement to illustrate the radius of the ring (marked with black triangles) and the size of one pixel, as indicated by the gray shaded area. (b) Radius of the ring $r_{\mathrm{ring}}$ against the probe beam detuning $\Delta_p$ for different peak Rabi frequency ratios $\Omega_p/\Omega_c$ in the absence (top) and presence (bottom) of atoms. Circled data points belong to the profiles shown in (a) and the gray dashed lines indicate effective pixel boundaries.

inset of Fig. A.2(a) as black triangles. Illustrating the effective pixel size in the imaging plane (gray shaded area), shows that the two radii are almost the same.

We extract the ring radius for different peak Rabi frequency ratios $\Omega_p/\Omega_c$ as a function of the probe beam detuning $\Delta_p$. Fig. A.2(b) displays the result in the absence and presence of the atoms. Without the atoms, the radius of the ring is as expected insensitive to the detuning of the probe beam. Moreover, it does not change when increasing the intensity of the probe beam. Averaging over all data points gives a mean ring radius of $(28.46 \pm 0.02)\,\mu$m. In the presence of the atoms, the situation does not change significantly. Almost all extracted ring radii fluctuate around the mean radius and lie within one pixel. Consequently, we conclude that no dispersive effects are present, which focus the ring inwards. Thus, the intensity in the center of the beam is not influenced by the ring structure.

Next, we estimate whether atoms that are illuminated by the ring could undergo nonlinear dynamics. For this purpose, we compare the Rabi frequency of the probe beam to the one of the control beam at the ring position. We extract both Rabi frequencies from the transmission images as explained in Sec. 4.1.3. Fig. A.3 shows that the ratio $\tilde{\Omega}_p/\tilde{\Omega}_c$ of the two Rabi frequencies at the ring position against the ratio $\Omega_p/\Omega_c$ in the beam center. Shown are the results for the Autler-Townes (blue points) and two-photon resonance (orange squares) measurements, presented in Sec. 4.4. As expected the ratio $\tilde{\Omega}_p/\tilde{\Omega}_c$ of the Rabi frequencies at the ring position increases linearly with the peak Rabi frequency ratio $\Omega_p/\Omega_c$. The green dashed line has a slope of one. For ratios below this line, we expect similar dynamics in the ring structure compared to the dynamics in the beam center. In particular, this means that e.g. the creation of spurious Rydberg excitations (see App. C) is

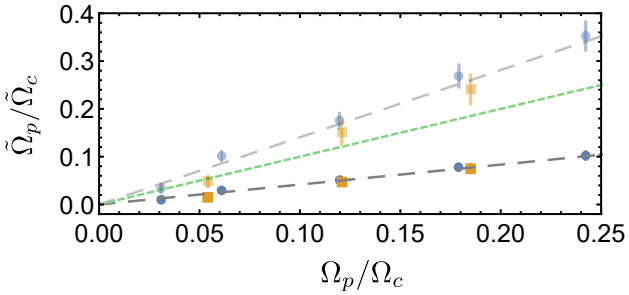


**Figure A.3: Ratio $\tilde{\Omega}_p/\tilde{\Omega}_c$ of the Rabi frequencies at the ring position.** Plotted against the ratio $\Omega_p/\Omega_c$ of the peak Rabi frequencies in the center of the probe beam. Blue points correspond to the Autler-Townes measurements presented in Fig. 4.14, while orange squares relate to the measurements on two-photon resonance of Fig. 4.15. Fully colored (opaque) data is calculated based on a control beam waist of 32.5 $\mu$m (20 $\mu$m). Gray dashed lines are guides for the eye, and the green dotted line has a slope of one.

not enhanced in the region of the ring. Most importantly this argument holds for the measurement on two-photon resonance with the lowest probe Rabi frequency, for which we observed enhanced absorption, since $\tilde{\Omega}_p/\tilde{\Omega}_c \leq \Omega_p/\Omega_c$.

For higher ratios $\Omega_p/\Omega_c$ and depending on the size of the control beam, the ratio $\tilde{\Omega}_p/\tilde{\Omega}_c$ of the Rabi frequencies at the ring position might exceed the ratio in the center of the beam. In these cases, the nonlinear behavior or the creation of spurious Rydberg excitations might be enhanced compared to the beam center. As we already excluded dispersive effects involving the ring structure, an enhanced nonlinear absorption in the ring does not influence the transmission measured in the center of the probe beam. Moreover, the distance between the ring and the beam center is too large for direct interactions between Rydberg excitations in these two regions. However, spurious Rydberg excitations could affect the measured transmission in the center of the probe beam if they undergo excitation transport dynamics [67, 181, 182] towards the probe beam center. This might especially be the case for high intensities of the probe beam where the density of photons in the medium and thus also the number of polaritons as possible hopping partners is high. Here, the time needed to reach the center of the probe beam might be smaller than the excitation time. However, for quantitative estimations, e.g. of the hopping frequencies, knowledge of the distribution of the spurious Rydberg excitations is missing. We address the topic of spurious Rydberg excitation and their possible sources in more detail in App. C.

In summary, we conclude that the main measurement for $\Omega_p/\Omega_c \approx 0.05$ on two-photon resonance is not affected by the presence of the ring structure. However, for high intensities of the probe beam, spurious Rydberg excitations might be created in the region of the ring. Further investigations would be need to clarify if they could undergo excitation transport towards the beam center and thus affect a transmission measurement at high ratios $\Omega_p/\Omega_c$ of the Rabi frequencies.

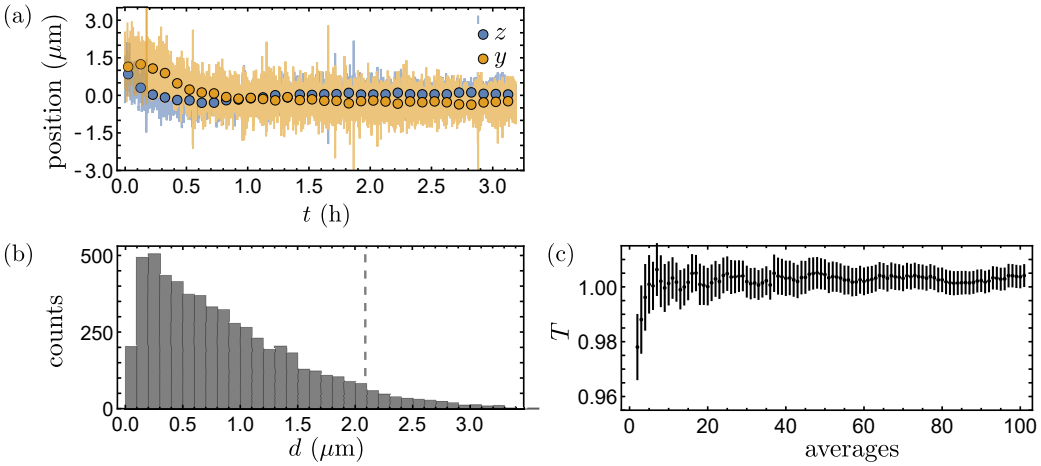


**Figure A.4: Long- and short-term stability of the focused probe beam.** (a) Position of the beam on the CCD camera as a function of time $t$. The position is given relative to the overall mean of all measurement points in $z$- and $y$-direction, respectively. (for the coordinate system see Fig. 4.2). Circles indicate the running mean of the data shown in the background. (b) Histogram of the distance $d$ between the beam centers on two different images, which are taken with a delay of about 70 $\mu$s. The gray dashed line indicates the effective pixel size. (c) Calculated transmission $T$ of the probe beam in the absence of the atomic cloud against the number of averaged images. For details see the main text.

### A.2.2 Positional stability

We measure the long- and short-term stability of the focused probe beam by taking every 2 s two images of the beam with a delay time of about 70 $\mu$s over a period of about three hours. The first time corresponds to the cycling time of our experiment. The second is the delay between the absorption and reference images needed for the determination of the probe beam transmission (see. Sec. 4.1.3). The third time corresponds to a typical time needed to acquire a sufficient amount of data for averaging. No atoms were present in this measurement.

For evaluating the long-term stability of the beam, we extract the beam position in $z$- and $y$-direction on the reference image and subtract the overall mean over all measurements in both directions, respectively. The result as a function of the time $t$ is shown in Fig. A.4(a). We find that the beam position drifts by no more than $\pm 1.5\,\mu$m in about 3 hours.

For an analysis of the short-term stability, we obtain the beam position from the absorption and reference image and calculate the distance $d$ of the two beam centers for each pair of images. It is important that the two beam centers overlap since the ratio of the two images determines the probe beam transmission. The resulting histogram is shown in Fig. A.4(b) and indicates some fluctuation of the beam centers. However, there is a 96% probability to find the two beam centers in the same effective pixel, the size of which is indicated as a gray dashed line in Fig. A.4(b). Therefore, the beam position is sufficiently stable on the timescale

over which the absorption and reference beam are recorded.

In order to investigate if the fluctuations in the beam position between the two images affect our analysis of the transmission $T$ of the probe beam, we calculate $T$ from the individual absorption and reference images and average them afterwards. The transmission should equal unity in the absence of atoms. Fig. A.4(c) shows the obtained transmission against the averages taken. We find that the fluctuations of the beam centers between the absorption and reference image average out for more than 10 averages. This is small compared to the number of averages we typically take in order to obtain a sufficient signal-to-noise ratio. We conclude that the long- and short-term stability of the focused probe beam is sufficient for the measurements presented in Chap. 4.

APPENDIX B

# Numerical simulation of the probe beam propagation

For the purpose of investigating dispersive effects in Sec. 4.2, the propagation equation, Eq. (3.13), of the probe field needs to be solved numerically. The split-step Fourier method [155, 156, 212] is a reliable and widely used tool for such a task. It relies on separating diffraction from refraction while numerically propagating the probe beam through the system. Specifically, the probe field is first discretized in position in the input plane and afterwards step by step refracted in Fourier space and diffracted in position space until the final plane is reached. A challenge for the discretization of the system is to take care of vastly different length scales. In our experimental setup this includes for example the waists of the probe and control beams compared to the extent of the imaging system with a distance of about 760 mm [173] from the atoms to the CCD camera. In fact, it would require to change the simulation grid size several times during the propagation process to account e.g. for the size of the imaging system while having a control beam waist, and thus the structure of interest, on the $\mu$m scale.

Here, we simplify the simulation in two aspects: First, we reduce the overall imaging system to a single $4f$-setup. This allows us to simulate the transmission images of the focused probe beam, as presented in Sec. 4.2.3. Second, we show that the propagation through the atomic cloud and a subsequent imaging system can be approximated by the propagation until the center of the cloud if the atomic density is doubled. This is possible since absorption is approximately a linear function of the atomic density for a medium of low optical depth, as used in the experiment under consideration. With this approximation we are able to compare our measurement results for the collimated probe beam with simulated transmission images, as presented in Sec. 4.2.1.

In the following, we first describe the applied numerical methods for the beam propagation in App. B.1. Afterwards, we introduce in App. B.2 the reduced imaging setup, which we exploit in Sec. 4.2.3 for simulating the transmission images of the focused probe beam after propagating through the atomic cloud. Finally, we argue in App. B.3 that for our purposes the full propagation through the system

can be simplified in good approximation by a propagation only until the center of the atomic cloud, if of the atomic density is simultaneously adjusted. This approximation has been used for the simulations in Sec. 4.2.1.

## B.1 Numerical methods

The propagation of the probe beam inside the atomic cloud is determined by the linear susceptibility of the medium, leading to absorption and dispersion. On the contrary, outside the atomic cloud the probe beam propagates through free space. Therefore, we separate the propagation of the beam into two parts[39]: First, we propagate the beam through the atomic cloud using the split-step Fourier method. Afterwards, a propagation through the imaging system follows. Here, we utilize large propagation steps in free space and multiply the field with phase factors for the lenses contained in the imaging system. In the following, we give some details about the used numerical methods.

### Split-step Fourier method

The split-step Fourier method is based on splitting diffraction, which contains spatial derivatives in transversal direction, from refraction, given by an external potential [155, 156, 212]. Here, we make use of the so-called symmetric Strang splitting [155]. It reduces the error made in the splitting process itself, which arises due to the non-commutativity of the operators for the diffractive and refractive part. Moreover, the diffractive part is most easily accounted for in Fourier space [156]. Applying this to the propagation equation, Eq. (3.13) of the probe field $\mathcal{E}(\mathbf{r}_\perp, z)$ yields the propagation formula [121]

$$\mathcal{E}(\mathbf{r}_\perp, z+\Delta z) = \mathcal{F}^{-1}\left[\mathcal{F}\left[\mathrm{e}^{-i\frac{1}{2}\chi^{(1)}(\mathbf{r})\Delta z}\mathcal{E}(\mathbf{r}_\perp, z)\right]\mathrm{e}^{-i(k_x^2+k_y^2)/(2k_p)\Delta z}\right]\mathrm{e}^{-i\frac{1}{2}\chi^{(1)}(\mathbf{r})\Delta z}. \tag{B.1}$$

Here, $\chi^{(1)}(\mathbf{r})$ is the linear susceptibility and determines the refractive part. $k_p$ is the wave vector of the probe beam, $k_{x,y}$ are the coordinates in Fourier space and $\Delta z$ denotes the step size in propagation direction. More details on the split-step Fourier method and its implementation can be found in my Master thesis [121].

### Free space propagation and lens phase factor

For the propagation in free space, $\chi^{(1)}(\mathbf{r}) = 0$. Therefore, the split-step Fourier method reduces to a multiplication of

$$h_{\mathrm{free}} = \exp\left[-i\Delta z\frac{k_x^2+k_y^2}{2k_p}\right] \tag{B.2}$$

[39] The split-step Fourier method in its basic form was implemented in Python during my Master thesis [121]. In the course of this dissertation, the code was improved and transferred to Matlab in order to increase the calculation speed. Moreover, the code was extended by the propagation through the imaging system as explained in this appendix.

with the probe field in Fourier space such that

$$\mathcal{E}(\mathbf{r}_\perp, z + \Delta z) = \mathcal{F}^{-1}\left[h_{\text{free}}\mathcal{F}\left[\mathcal{E}(\mathbf{r}_\perp, z)\right]\right] . \tag{B.3}$$

Since the Nyquist theorem for sampling the quadratic phase factor in Eqs. (B.1) and (B.2) needs to be obeyed, the split-step Fourier method and the propagation in free space are only applicable in the near field, meaning until a critical propagation distance $z_{\text{crit}} = N\mathrm{d}x^2/\lambda_p$ [213, 214]. Here, $N$ denotes the number of points in the grid with a resolution $\mathrm{d}x$, and $\lambda_p$ is the wavelength of the probe beam.

Finally, a lens imprints a phase on the probe field, which within the paraxial and thin-lens approximation reads [102, 215]

$$H_{\text{lens}} = \exp\left[-i\frac{k_p}{2f}(x^2 + y^2)\right] . \tag{B.4}$$

It is multiplied with the field in real space. Here, $f$ is the focal length of the lens.

## B.2 Optical setup for the simulation

In the following, we describe a reduced imaging setup for the simulations involving the focused probe beam. Thereby, we have two purposes in mind: First, we want to compare the prediction of such a simulation with our experimental results presented in Sec. 4.2.3. Second, we want to exploit this scheme in App. B.3 for justifying the approximation made for the simulations involving the collimated probe beam.

The imaging system of our experimental setup consists of a $4f$-system with lenses of focal length 145 mm and a magnifying telescope composed of two lenses with focal lengths 10 mm and 80 mm [173]. It images the object plane in the center of the atomic cloud onto the CCD camera in the imaging plane. Here, we aim at comparing the observed structure of transmission images in Sec. 4.2 on a very fundamental level with a numerical simulation. In particular, this means that we want to compare structures originating from dispersion, and not from aberrations or other imperfections of the imaging system. Therefore, we can reduce the system to a single $4f$-system in our simulations for the focused probe beam, as schematically shown in Fig. B.1. This is particularly advantageous since a reduced system size circumvents the problem of changing the grid size several times. Indeed, we find that changing the grid size ones is sufficient in our case for obeying the sampling requirement discussed in the previous section. For a comparison with the experimental results, the probe beam images obtained numerically only need to be scaled in size accordingly.

The particular geometry of the whole system and its discretization have to meet the following conditions: First, the critical propagation distance needs to be obeyed. This constrains the grid size, the resolution as well as the focal length. Second, we aim in App. B.3 at comparing the structure of the transmission images, obtained by numerically propagating the probe beam through the atomic cloud and the imaging system, with the ones obtained by propagating only through half of the cloud with the atomic density doubled. The second situation constitutes the

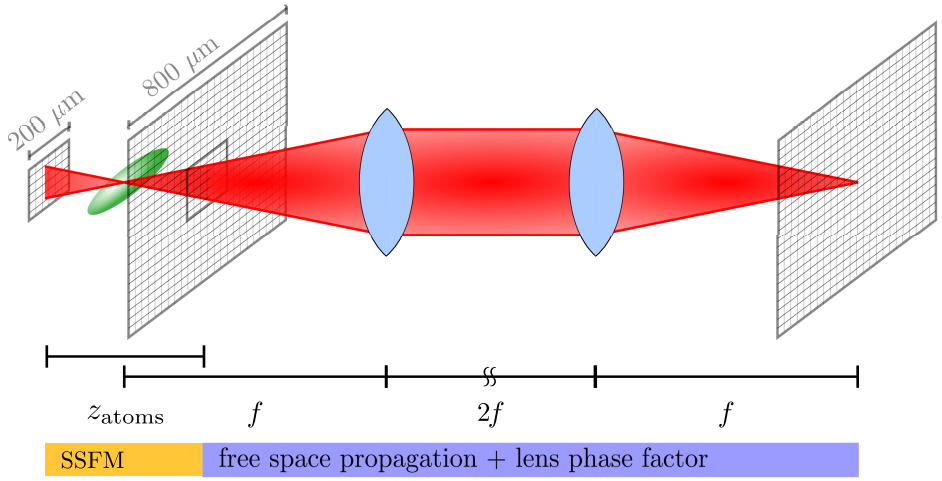


**Figure B.1: Schematic illustration of the optical setup for the numerical simulation of the probe beam propagation.** First, the probe beam (red) is propagated through the atomic cloud (green ellipsoid) over a distance of $z_{\text{atoms}} = 200\,\mu\text{m}$ on a transversal grid of $200 \times 200\,\mu\text{m}^2$ using the split-step Fourier method (SSFM). After increasing the grid to a size of $800 \times 800\,\mu\text{m}^2$ with the same resolution, the beam is propagated to the imaging plane through a $4f$-imaging system with focal length $f = +200\,\mu\text{m}$ using a propagation in free space and phase factors for the lenses (light blue objects). For details see the main text. The drawing is not to scale.

case of a perfect image, as the structure in the object plane is directly considered. Therefore, the imaging system should have a reasonably good resolution, given by a large numerical aperture[40] $\text{NA} = \sin\theta \approx N\mathrm{d}x/(2f)$ [102].

For the propagation through the atomic cloud we chose a transversal grid of $200 \times 200\,\mu\text{m}^2$ with a resolution of $\mathrm{d}x = 0.78\,\mu\text{m}$, meaning $N = 2^8$. In this case $z_{\text{crit}} \approx 200\,\mu\text{m}$. As the effective Gaussian width of the atomic cloud in propagation direction is $\sigma_{\text{eff}} \approx 28\,\mu\text{m}$, we use $7\sigma_{\text{eff}} \approx z_{\text{crit}}$ as the propagation distance through the cloud, as indicated in Fig. B.1.

For the propagation through the imaging system, we keep the same resolution, but enlarge the size of the grid to $800 \times 800\,\mu\text{m}^2$ with $N = 2^{10}$. As a consequence, $z_{\text{crit}}$ is increased to approximately $800\,\mu\text{m}$. This distance can accommodate a $4f$-setup with focal length[41] $f = 200\,\mu\text{m}$. The resulting numerical aperture of $\text{NA} = 2$ is large enough to compare the imaged transmission profile with the one obtained when only propagating until the center of the atomic cloud.

Based on the previous discussion, the simulation results for the focused probe beam presented in Fig. 4.9(b) are obtained as follows and as indicated in Fig. B.1: First, we use the split-step Fourier method to propagate the probe beam numerically through the atomic cloud over a distance of $z_{\text{atoms}} = 200\,\mu\text{m}$. Thereby,

[40] As we do not restrict the lens in size, the numerical aperture is defined by half the grid size in transversal direction.

[41] Using a focal length of $100\,\mu\text{m}$ gives with a relative error below $10^{-5}$ the same simulation results.

we use the grid as described above and a step size in propagation direction of $0.39\,\mu$m. Afterwards, we pad the grid with zeros to obtain a size of $800 \times 800\,\mu\text{m}^2$ and propagate the probe beam in one step over a distance of $f - z_{\text{atoms}}/2$ to the first lens. After multiplication with the lens phase factor, Eq. (B.4) another propagation step with distance $2f$ follows. The imaging system is completed with the multiplication of the second lens phase factor and a propagation step of length $f$ to the imaging plane. We have confirmed that in the absence of the atomic cloud a 1:1 image of the focused probe beam is correctly obtained with our simulation.

## B.3 Simplification of the simulation

As outlined in the introduction of this appendix, we approximate in Sec. 4.2.1 the propagation of the collimated probe beam in the following way: We double the experimentally applied atomic density and evaluate the transmission images in the center of the atomic cloud. In this section, we argue that this approximation is justified for the specific case of our experimental system. First, we test the approximation using the reduced imaging setup for the focused probe beam, which has been described in the previous section. Afterwards, we compare the structure of simulated transmission images for the collimated probe beam with and without doubling the atomic density.

For the first case, we consider the following situations:

(i) A propagation of the focused probe beam through the combined system of the atomic cloud with the experimental parameters of Fig. 4.9 and the reduced imaging system introduced in Sec. B.2.

(ii) A propagation stopped in the center of the atomic cloud but with the atomic density increased by a factor of two compared to the experimental parameters.

(iii) The same situation as in (ii) but with an infinitely large control beam waist and an atomic density distribution that is constant in transversal, and Gaussian in propagation direction.

The aim is to show that situations (i) and (ii) give approximately the same simulation results. For this purpose, we simulate the transmission evaluated in the center of the control beam, and the relative change of the probe beam waist, which is prone to dispersion. For both situations we consider the experimental geometry of the atomic cloud, which follows a Gaussian distribution in all three dimensions. Situation (iii) is effectively a dispersion free realization of situation (ii) and gives additional insights for the discussion.

Fig. B.2 shows the simulated transmission $T$ of the probe beam, and the change in the beam waist $\Delta w_p$ for the three situations as a function of the probe beam detuning $\Delta_p$. For the transmission, depicted in Fig. B.2(a), all three situations give very similar results. A slight asymmetry of the Autler-Townes spectrum is apparent when propagating only until the center of the atomic cloud with twice

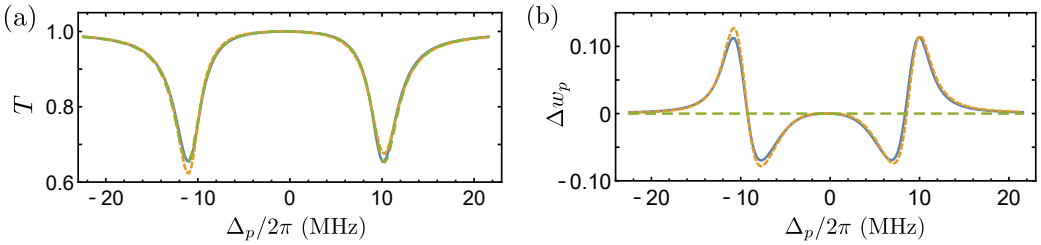


**Figure B.2: Results of the numerical simulation for the propagation of the focused probe beam.** Numerically obtained (a) transmission $T$ and (b) relative difference $\Delta w_p$ of the beam waist with respect to the waist in the absence of the atoms as a function of the probe beam detuning $\Delta_p$. The numerical results for the situations (i)-(iii), as introduced in the main text, are shown as blue solid, dashed orange and green dashed lines, respectively. Simulation parameters are the same as for Fig. 4.9.

the atomic density. This asymmetry is not apparent when imaging the probe beam with the telescope (i) or when the control beam waist is infinitely large (iii).

For the simulated probe beam waists shown in Fig. B.2(b) the situation is analogous. While the curve is symmetric for the situation (i) a small asymmetry is apparent for (ii). For an infinitely large control beam waist in situation (iii), the system is effectively dispersion free, and thus the probe beam waist remains unchanged as a function of the probe beam detuning.

That the situations (i) and (ii) give similar results for the change in the beam waist does not come at a great surprise, as the telescope produces an image of the probe beam structure in the center of the cloud. In the absence of dispersion, as in situation (iii), an increase of the atomic density by a factor of two mimics the omitted absorption in the second half of the cloud, since absorption of the atomic medium is approximately a linear function of the density. Therefore, it is also expected to obtain a similar result for the probe beam transmission for the situations (i) and (iii). Only dispersive effects, which depend on the atomic density, are slightly exaggerated when doubling the atomic density. They artificially add an asymmetry to the transmission and beam waist spectra for the situation (ii). However, these discrepancies are small compared to the overall shape of the spectra, which we want to simulate.

The above discussion suggests, that in good approximation situations (i) and (ii) give similar results for the transmission of the probe beam and the change in waist due to dispersion.

Being able to replace the propagation through the full system of atomic cloud and imaging telescope by a propagation until the center of the cloud with twice the experimentally used density, becomes particularly advantageous when aiming at simulating the propagation of the collimated probe beam in Sec. 4.2.1. In order to confirm that this replacement preserves the structure of the transmission images for the collimated probe beam, we show in Fig. B.3 numerically obtained transmission images at a probe beam detuning of $\Delta_p/2\pi = 4\,\mathrm{MHz}$ and cross sections thereof. Both situations, i.e. when propagating the probe beam until

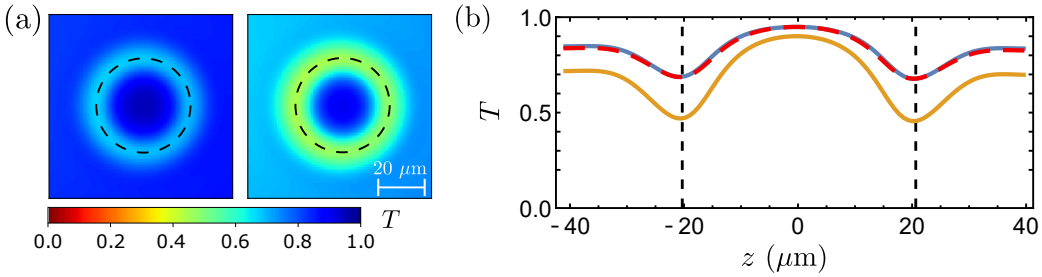


**Figure B.3: Results of the numerical simulation for the propagation of the collimated probe beam.** Numerically obtained (a) transmission images and (b) cross section thereof through the image center for a propagation until the center of the atomic cloud with the experimental atomic density [left image in (a) and blue solid line in (b)], and with twice the density [right image in (a) and orange solid line in (b)]. The red dashed line is the orange one scaled as described in the main text. The black circles in (a) have the same radius of 20.3 $\mu$m, which is also indicated in (b) by the black dashed lines. Other simulation parameters are the same as for Fig. 4.6.

the center of the atomic cloud with the experimental value for the atomic density (den) and with the density doubled (2den), are shown. The transmission images in Fig. B.3(a) exhibit the same structure and only the level of transmission is different. This can also be seen in Fig. B.3(b), which displays cross-sections of the images. Therefore, we find that doubling the atomic density does not result in a significant change of the image structure. In order to make this point even clearer, we rescale one of the curves. For this purpose, the cross section $T_{\mathrm{2den}}$ is multiplied by a factor $[\max(T_{\mathrm{den}}) - \min(T_{\mathrm{den}})]/[\max(T_{\mathrm{2den}}) - \min(T_{\mathrm{2den}})]$ and with an additional offset of $\min(T_{\mathrm{den}})$ results in the red dashed line in Fig. B.3. Indeed, this scaled curve agrees well with the cross section $T_{\mathrm{den}}$. This in combination with the results obtained with the focused probe beam suggests that the approximation made in Sec. 4.2.1 for the numerical investigation of the transmission images of the collimated probe beam is reasonable. We emphasize that this only holds for our particular situation, which consists of a medium of low optical depth and of Gaussian beams.

APPENDIX C

# Rydberg pollutants

*Parts of this appendix are based on the following publication, from which parts of the text have been taken verbatim*:

> **Nonlinear absorption in interacting Rydberg electromagnetically-induced-transparency spectra on two-photon resonance**
> A. Tebben, C. Hainaut, A. Salzinger, S. Geier, T. Franz, T. Pohl, M. Gärttner, G. Zürn and M. Weidemüller, Phys. Rev. A **103**, 063710 (2021)

In Rydberg EIT experiments care has to be taken to not create stationary Rydberg excitations in the medium as they could lead to absorption that conceals the nonlinear absorption effects stemming from Rydberg EIT nonlinearities. Being created at high Rabi frequencies of the probe beam these excitations have been termed "Rydberg pollutants" [143]. They have been observed in photon propagation experiments with large input rates [143] and in investigations of radiation trapping at large optical depth [216].

We have also observed stationary Rydberg excitations in our experiment at large Rabi frequencies of the probe beam. Therefore, this appendix serves two purposes: First, we show in App. C.1 that the measured features on two-photon resonance for a ratio of $\Omega_p/\Omega_c = 0.05$ of the Rabi frequencies cannot be explained by the presence of Rydberg pollutants. Second, we discuss in App. C.2 possible creation mechanisms for Rydberg pollutants in our experiment. This can serve as a starting point for further investigations and successive elimination of Rydberg pollutants in Rydberg EIT experiments.

## C.1 Rydberg excitation measurement on two-photon resonance[42]

For the measurement on two-photon resonance presented in Fig. 4.15 we have simultaneously recorded the ion counts on the MCP, as shown in Fig. C.1. Thereby,

[42] Taken verbatim from Tebben *et al.* [96] with minor adaptions for the ease of readability.

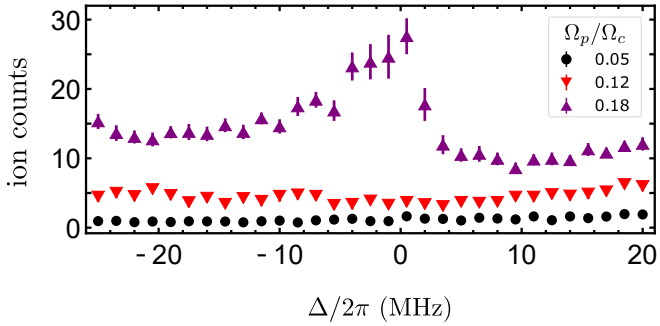


**Figure C.1: Rydberg excitation measurement on two-photon resonance.** Measurements of ion counts as a function of the single-photon detuning $\Delta$ on two-photon resonance $\delta = 0$ for different ratios $\Omega_p/\Omega_c$. The ions have been detected simultaneously with the measurement of Fig. 4.15. Figure and caption taken with permission from [98].

the detection efficiency is about 0.10 ions per Rydberg atom [179]. For the ratio of $\Omega_p/\Omega_c = 0.05$, where the nonlinear absorption in the transmission measurements appears, the number of detected ions is about 1 for all detunings, as shown by the black circles in Fig. C.1. When increasing the ratio of the two Rabi frequencies further, the ion count increases to about 4 counts, but stays approximately constant over the whole range of single photon detunings. For the highest measured ratio, the number of detected ions increases significantly with a maximum around zero single-photon detuning.

In the case of a coherent evolution in the EIT system we would expect to detect no ions after the EIT sequence. The reason is that photons entering the medium are adiabatically converted into polaritons, which are transformed back into photons when leaving the medium. Therefore, we attribute the observed ions at high ratios of the two Rabi frequencies to stationary Rydberg excitations in the medium. As these excitations do not get depumped by the control beam into the decaying intermediate state, it is to be presumed that these are excitations in other than the Rydberg state $|48S_{1/2}, m_j = 1/2\rangle$.

For the measurement on two-photon resonance[43] at a ratio $\Omega_p/\Omega_c \approx 0.05$, we measure approximately one ion count at the position of the transmission dip at $\Delta_{\text{min}} = -8\,\text{MHz}$. According to the detection efficiency, this sets an upper bound of 10 on the number of Rydberg excitations $N_{\text{Ryd}}$ in the medium.

We now consider a worst-case scenario in order to estimate the maximal influence of these excitations on the probe beam propagation. For this purpose, we assume that all these excitations are located in the integrated region of $4 \times 4$ pixels, where the probe beam transmission is evaluated. Furthermore, we can assume in an upper bound estimation that these excitations are atoms in the nearby Ryd-

[43] Regarding the measurement of the interacting Autler-Townes spectrum presented in Fig. 4.14: The atomic density and the ratio of the two Rabi frequencies of that measurement connect to the red curve in Fig. C.1. Therefore, the ion measurement suggests the presence of a large number of Rydberg excitations that could lead to the observed slightly lower transmission around resonance.

berg state $|48P\rangle$. This state process strong dipolar interactions with the Rydberg state $|48S\rangle$ with a coefficient $c_3$ of about $1.7\,\mathrm{GHz}\mu\mathrm{m}^3$.

We estimate the resulting absorption from theses excitations as follows: Each Rydberg excitation renders the medium absorptive in a spherical volume given by the blockade radius $R_b$, which is approximately $3.1\,\mu$m at $\Delta_{\mathrm{min}}$. Assuming that all excitations are placed in a chain behind each other, the resulting optical depth $\mathrm{OD}_{\mathrm{Ryd}} = \mathrm{OD}_{\mathrm{off}} 2R_b N_{\mathrm{Ryd}}/L$ can be calculated from the propagation distance $L$ through the whole atomic cloud, the peak atomic density $\rho_0$, which is given in the caption of Fig. 4.15, and the off-resonant optical depth $\mathrm{OD}_{\mathrm{off}} = \sigma_{\mathrm{off}}\rho_0 L$ of two-level atoms. Here, the off-resonant cross section $\sigma_{\mathrm{off}} = a\sigma_0$ is the resonant cross section $\sigma_0$ multiplied by a factor $a = 0.126$. It takes into account the Lorentzian lineshape of the two-level absorption with decay rate $\Gamma_e$. In the last step, we have to account for the fact that the transversal size $A_{\mathrm{Ryd}} = \pi R_b^2$ of one blockaded volume is smaller than the evaluated pixel area $A = (4 \times 2.1\,\mu\mathrm{m})^2$ on the CCD camera. Therefore, we use the scale $s = A_{\mathrm{Ryd}}/A$ to finally obtain the transmission $T_{\mathrm{Ryd}} = (1-s)+s\exp(-\mathrm{OD}_{\mathrm{Ryd}}) \approx 0.87$ in the presence of ten Rydberg excitations.

Overall, this estimation in a worst-case scenario results in an upper bound of 13% for the probe beam absorption solely due to these Rydberg excitations. Therefore, for the ratio of $\Omega_p/\Omega_c = 0.05$, unwanted Rydberg excitations cannot explain the observed strong absorption feature of about 76%.

## C.2 Possible creation mechanisms of Rydberg pollutants

In this section, we discuss various mechanisms that could lead to the creation of Rydberg pollutants, and check their plausibility for our measurements on two-photon resonance. In general, we can exclude that Rydberg pollutants are excitations in the state $|r\rangle = |48S_{1/2}, m_j = 1/2\rangle$. The reason is that these excitations are coupled to the control beam. As a consequence, they get depumped at the end of the EIT sequence before the cloud is ionized for Rydberg ion detection on the MCP.

Rydberg pollutants in Rydberg states other than the state $|r\rangle$ could, for example, populate the energetically close states $|47P\rangle$, $|48P\rangle$ and $|49P\rangle$. Excitations in these states most dominantly affect the probe beam propagation as they possess strong dipolar interactions with the state $|48S\rangle$. Concerning the creation process itself, we suppose that the number of pollutants created is connected to the number of photons, respectively polaritons, inside the medium.

In the following, we consider two different situations for estimating the number of Rydberg pollutants in the medium. Both connect to the measurements on two-photon resonance presented in Sec. 4.15. In fact, we consider the two situations with the ratios $\Omega_p/\Omega_c = 0.05$ (low intensity of the probe beam) and 0.18 (high intensity of the probe beam) of the Rabi frequencies both on single-photon resonance[44]. For estimating the number of Rydberg pollutants in the medium, one

[44] We note that off single-photon resonance the group velocity of the photons is considerably increased. The reason is that the atomic cross section is replaced by the much smaller off-resonant cross section in Eq. (2.17) for the group velocity. As a consequence, we expect even

needs to know

- the mean number of photons $\langle n_{ph} \rangle$ traversing the medium during the excitation time of $t_{\mathrm{exc}} = 5\,\mu\mathrm{s}$,
- the time $\tau_m$ that it takes for the photons to propagate through the atomic cloud, and the time $\tau_{\mathrm{bl}}$ in which the photons propagate through the distance of one blockade radius,
- the mean number of photons that are inside the medium at the same time. Assuming, that each photon gets converted into a polariton, this equals the mean number of polaritons $\langle n_{\mathrm{DSP}} \rangle$ inside the medium in a steady-state situation.

We obtain the mean number of photons $\langle n_{ph} \rangle$ in the probe beam from its images measured with the CCD camera in the absence of the atoms. This yields approximately 6560 and 55.150 photons in the low- and high-intensity case, respectively. The propagation times $\tau_m$ and $\tau_{\mathrm{bl}}$ can be calculated from the group velocity $v_g$ given in Eq. (2.17). Hereby, we assume that the atomic cloud has a Gaussian-shaped density distribution along the propagation axis with a peak atomic density $\rho_0 = 0.16\,\mu\mathrm{m}^{-3}$ and a width of $\sqrt{2}\sigma_z = \sqrt{2} \times 22\,\mu\mathrm{m}$. The factor $\sqrt{2}$ accounts for the 45° angle between the main axis of the cloud and the propagation direction of the probe beam (see Fig. 4.2 for an illustration). With this geometry of the atomic cloud and with a blockade radius of $2.4\,\mu\mathrm{m}$, which is given by the parameters of the measurement, we obtain $\tau_m \sim 6.1\,\mathrm{ns}$ and $\tau_{\mathrm{bl}} \sim 0.2\,\mathrm{ns}$. Finally, in a steady-state situation we estimate the number of polaritons that are inside the medium at the same time by using the equation $\langle n_{\mathrm{DSP}} \rangle = \langle n_{ph} \rangle \tau_m / t_{\mathrm{exc}}$. This yields about 8 and 68 polaritons for the low- and high- intensity case, respectively.

Based on these preparatory estimations, we now discuss four possible mechanisms for the creation of Rydberg pollutants.

### (i) Population in a different Zeeman sublevel

Within our three-level scheme in ladder configuration the control beam couples the intermediate state to the Rydberg state $|48S_{1/2}, m_j = 1/2\rangle$. In principle, also the other Zeeman sublevel ($m_j = -1/2$) could get populated [217] if, for example, the polarization of the control beam was wrong or if the splitting between the levels was too small. However, we apply a magnetic offset field of 30 G, which leads to a splitting of the two Zeeman sublevels by $\Delta_{-1/2} = 84\,\mathrm{MHz}$. In combination with a careful preparation of the ground state as well as appropriate laser beam polarizations, as described in Sec. 4.1.2 and Sec. 4.1.3, we isolate the desired the three-level system.

In a worst-case scenario, we estimate from a polarization measurement that 5% of the power of the control beam could lead to a coupling to the other

less photons/polaritons to reside inside the medium at the same time in the off-resonant case compared to the situation on resonance. This also reduces the number of possible pollutants in the medium. For an estimation of an upper bound for the number of pollutants, we consider the resonant case in the following.

Zeeman sublevel with $m_j = -1/2$. This corresponds to a Rabi frequency of $\Omega_{c,-1/2}/2\pi = \sqrt{0.05} \times 24\,\mathrm{MHz} \approx 5.4\,\mathrm{MHz}$ and would yield a negligible population [179] of $\Omega^2_{c,-1/2}/(\Omega^2_{c,-1/2} + \Delta^2_{-1/2}) < 0.4\%$ in the other Zeeman sublevel.

### (ii) Black-body decay

The state $|48S\rangle$ decays to surrounding Rydberg P-states with a black-body decay rate of $\tau_{bb} = 117.8\,\mu\mathrm{s}$ [130]. As discussed above, we expect about 8 (68) polaritons to be in the medium in steady-state in the low- (high-) intensity case, respectively. Due to their Rydberg component these polaritons could potentially decay. We obtain the average number of excitations in the P-sates resulting from black-body decay with the equation $\langle n_{\mathrm{DSP}}\rangle t_{\mathrm{exc}}/\tau_{bb}$, yielding 0.3 and 2.9 excitations, respectively. These numbers are much smaller than the observed number of Rydberg excitations in the medium, as presented in Fig. C.1. As a consequence, black-body decay to other Rydberg states is not the dominant mechanism for the formation of Rydberg pollutants.

### (iii) Pair-state resonances at the entrance of the medium

Mirgorodskiy [194] has discussed another mechanism that could lead to the creation of Rydberg pollutants: When the first photon enters the medium it propagates as a polariton with a reduced group velocity. Therefore, it blockades the entrance of the medium for the time $\tau_{bl}$. If a second photon arrives during this time a pair-state involving the $|48S\rangle$ state might be resonantly excited. This process depends on whether there exists a pair-state resonance for the particular distance between the photon and the polariton. Furthermore, this process is independent of the probe beam detuning [194].

In Fig. C.1 we see that the number of ion counts is approximately independent of the detuning for the two smallest ratios $\Omega_p/\Omega_c$ of the two Rabi frequencies. However, a strong dependence on the detuning $\Delta$ for the highest ratio has been measured. This observation contradicts, at least in the regime of high probe intensities, the mechanism of creating Rydberg pollutants via pair-state resonances. Nevertheless, we would like to give an order of magnitude estimation of how many Rydberg pollutants could be produced with this process.

The probability $p_{2\mathrm{phot}}$ of two-photons to arrive at the medium simultaneously within $\tau_{bl}$ is given by $p_{2\mathrm{phot}} = R_{in}\tau_{bl}\exp(-R_{in}\tau_{bl})$ [194] due to Poisson statistics. Here, $R_{in}$ is the incoming photon rate. We evaluate this probability for an area corresponding to a pixel in the image of the probe beam. Thus, $R_{in} = \langle n_{ph}\rangle_{\mathrm{px}}/t_{\mathrm{exc}}$ is given by the mean number $\langle n_{ph}\rangle_{\mathrm{px}}$ of photons per pixel. In the beam center we obtain a probability of 0.2% and 2% for the low- and high-intensity case, respectively. We multiply the probability calculated in each pixel with the number of photons detected in each pixel. Summing over all pixel, gives about 4 and 468 occurrences where two photons are simultaneously at the entrance of the medium for the two cases, respectively. However, not each occurrence necessarily results in the excitation of a pair-state and thus a Rydberg pollutant [194]. Instead, the excitation probability should also depend on the dipole coupling strength

of the pair resonance [194]. Including this dependence in the above calculation would yield a better estimate for the number of created Rydberg pollutants. For example, this could be done via a Monte Carlo sampling. Such a simulation could on the one hand take into account the Poisson statistics of photons arriving at the entrance of the medium, and on the other hand the probability to excite a pair-state [194]. Nevertheless, our estimation yields upper bounds for the amount of pollutants created in the two considered cases. They are within an order of magnitude comparable to our measurement (see Fig. C.1). Still, the discrepancy concerning the dependence of this creation mechanism on the detuning of the probe beam remains.

#### (iv) Radiation trapping and subsequent excitation transfer

Bienias *et al.* [143] have explained an initial creation of Rydberg excitations with radiation trapping [184, 216] of scattered probe photons due to a large transverse optical depth. Moreover, they suggested that anti-blockade excitation or state-changing collisions transfer the excitations to a Rydberg state different from the one used for EIT [143]. This would explain why the Rydberg pollutants are not coupled to the control beam and thus why they have been found to remain in the atomic medium after the EIT sequence.

For an estimation of the expected amount of Rydberg pollutants from these processes, we first consider the rate $R_{\text{scat}}$ of scattered photons within the excitation time. This rate is given by the percentage $p_{abs}$ of absorbed light, which can be inferred from the transmission measurement shown in Fig. 4.15. In the low- and high-intensity situation we find that maximally 24% and 60% of the incoming light is absorbed, respectively. In an upper bound estimation, we assume that these photons are not scattered in all spatial dimensions, but only in a single direction transverse to the propagation axis. This allows us to exploit the same estimation as for the idea of exciting pair-resonances at the entrance of the medium. Replacing $R_{in}$ with $R_{\text{scat}} = p_{abs} R_{in}$ we obtain from an analogous calculation 0.26 and 170 Rydberg pollutants for the low- and high-intensity case, respectively. These numbers are far too small in order to explain the detected number of pollutants.

The presented estimation completely ignores the spatial distribution of scattered photons and thus overestimates the number of pollutants created from pair-resonances. On the contrary, it falls short in accounting for multiple scattering events in the medium, which would enhance the effective time a photon/polariton spends in the medium [143, 216]. This in turn could lead to a larger probability for e.g. state-changing collisions and thus potentially to an increased number of Rydberg pollutants.

In order to consider multiple scattering events, we can estimate how many photons/polaritons are in the medium at the same time in a steady state situation including multiple scattering events. From this estimation a mean distance between the photons/polaritons can be obtained and compared to the blockade radius. This comparison could give some insight on whether state-changing collisions or anti-blockade excitation could contribute to the production of Rydberg pollutants. For such an analysis, knowledge of the transversal optical depth is re-

quired as it provides an approximation of how many times photons are scattered before they leave the medium [143]. When scattered probe photons escape the region of the control beam, they cannot be excited to the Rydberg state anymore. Therefore, we estimate $\mathrm{OD}_{\mathrm{trans}} = \sigma_0 \rho_0 w_c \approx 1.4$ in our situation, where $\sigma_0$ is the atomic cross section. $\rho_0$ denotes the peak atomic density and $w_c$ is the waist of the control beam. Furthermore, we assume that the lifetime of scattered photons is given approximately by $\tau_{\mathrm{scat}} \approx \mathrm{OD}_{\mathrm{trans}}/\Gamma_e$ in accordance with refs. [184, 216]. It follows that there are $(1 - p_{abs})\langle n_{ph}\rangle \tau_m / t_{\mathrm{exc}}$ photons in the medium, which are not scattered, and $p_{abs}\langle n_{ph}\rangle \tau_{\mathrm{scat}}/t_{\mathrm{exc}}$ photons, which are scattered multiple times. The sum of both gives the total number of photons that are in the medium simultaneously. Here, $p_{abs}$ is again the percentage of absorbed photons. Finally, we assume a rod like geometry for the overlap region of the control beam and atomic cloud. This geometry in combination with the number of photons, which are scattered multiple times, yields mean distances of about 7.6 $\mu$m and 2.8 $\mu$m between the photons/polaritons in the low- and high-intensity situation, respectively. Comparing this to a blockade radius of about 2.4 $\mu$m in becomes clear that rescattering of photons and subsequent excitation transfer to other Rydberg states could affect the number of Rydberg pollutants for high, but presumably not for low intensities of the probe beam.

#### Summary of the different creation mechanisms of Rydberg pollutants

Rydberg pollutants are stationary excitations in the medium, which do not couple to the control beam, but at the same time strongly interact with atoms populating the Rydberg state used for EIT experiments. We discussed (i) the population of a different Zeeman sublevel, (ii) black-body decay, (iii) pair-state resonances excited at the beginning of the medium, as well as (iv) radiation trapping in combination with excitation transfer as possible mechanisms for the creation of Rydberg pollutants. We find that only the mechanisms (iii) and (iv) yield within an order of magnitude an estimated number of Rydberg pollutants, which is comparable with our measurement. However, from the model (iii) we would expect no dependence of the amount of Rydberg pollutants on the probe detuning. This strongly contradicts our measurement at high intensities of the probe beam. One could envision that both mechanisms (iii) and (iv) occur in our system and that they together constitute the source of the Rydberg pollutants, which we observe.

It has been discussed that Rydberg atoms are predominantly excited at the beginning of the medium where the probe intensity is highest [78]. As such, an accumulation of excitations at the entrance of the medium could increase the probability for pair-resonances and state-changing collisions. Nevertheless, we conclude that the precise origin of these Rydberg pollutants and a corresponding quantitative model remain to be found. Further experimental investigations, as discussed in Sec. 4.6, would be needed to shed light on this aspect.

APPENDIX D

# Comparison between mean-field and MCRE model

*This appendix is based on the publication*

> **Nonlinear absorption in interacting Rydberg electromagnetically-induced-transparency spectra on two-photon resonance**
> A. Tebben, C. Hainaut, A. Salzinger, S. Geier, T. Franz, T. Pohl, M. Gärttner, G. Zürn and M. Weidemüller, Phys. Rev. A **103**, 063710 (2021)

*from which the following text has been taken verbatim with minor adaptions for the ease of readability.*

In the spectra on two-photon resonance, presented in Sec. 4.5, a stronger absorption is predicted by the mean-field model than by the result of the Monte-Carlo rate equation model, as shown in Fig. 4.17. In the following, we explain that this results from the assumption of how the interaction-induced level shift is included in the two models.

On one hand, in the MCRE model the total interaction-induced level shift $\Delta_{\mathrm{int}}^{(i)}$ experienced by an atom $i$ is determined by the sum $\sum_{j\neq i}\Delta_{ij} = \sum_{j\neq i} C_6/r_{ij}^6$ over all shifts induced by the surrounding Rydberg atoms [78]. As the MCRE simulation is seeded with a distribution of atoms according to the geometry of the experiment, the inter-atomic distances $r_{ij}$ vary. This immediately leads to a certain variation of the level shifts $\Delta_{ij}$.

On the other hand, the considered mean-field model is based on the non-interacting single-body susceptibility and includes an interaction-induced level shift therein [64]. This means that nothing like an atomic distribution, and therefore no variance of the level shift is considered *a priori*. For distances smaller than the blockade radius, the level shift is completely determined by an integration over the radius $r$ and the resulting susceptibility $\chi_B$ inside the blockade radius is therefore unambiguously defined. However, for the susceptibility $\chi_E$ outside the blockaded sphere assumptions about the average level shift $\Delta_R$ and its variance $\theta_R$

have to be made. Han *et al.* [64] calculate both based on a mean-field assumption as well as on an assumption for the Rydberg excitation fraction. Explicitly, the formula for the variance reads [64]

$$\theta_R \approx \int_{R_b}^{\infty} f_R \rho_0 \frac{C_6^2}{r^{12}} 4\pi r^2 dr = \frac{4\pi C_6^2 f_R \rho_0}{9 R_b^9}\,, \tag{D.1}$$

where $f_R = \frac{f_0}{1-f_0+f_0\rho_0 V_B}$ [64] is the Rydberg excitation fraction in the interacting regime, and $f_0$ the one in the non-interacting regime. Here, $V_B$ is the spherical volume spanned by one blockade radius $R_B$. The variance is then included as an effective dephasing $\gamma_{gr} = \sqrt{\theta_R}$ of the Rydberg coherence in the single-body susceptibility [64]. Finally, the Rydberg excitation fraction determines the weight between the two parts of the overall model susceptibility $\bar{\chi} = \alpha\chi_B + (1-\alpha)\chi_E$, as $\alpha \propto f_R$ [64]. This implies, that the more one enters the blockaded regime (large $\alpha$), the less weight is put on the assumption made for the variance of the level-shift entering $\chi_E$.

For the Autler-Townes measurement in the interacting regime, presented in Fig. 4.16, $\alpha$ is larger than 0.6 around the Autler-Townes transmission minima. Hence, the contribution of $\chi_B$ and $\chi_E$ are quite similar, such that the relative importance of including a variance of the level shift is small. As a result, the mean-field and MCRE models give similar predictions for the transmission spectrum. Only around resonance, where $\alpha$ is about 0.2, deviations between the two models start to appear.

For the measurement on two-photon resonance $\alpha < 0.12$ for all single-photon detunings $\Delta$ and is especially only about 0.025 at $\Delta/2\pi = -2\,\mathrm{MHz}$, as shown in Fig. D.1(c). At the same the effective dephasing on the Rydberg coherence $\sqrt{\theta_R}/2\pi$ is as large as 5 MHz, putting a great deal of weight on the assumptions made in the mean-field model.

In order to show, that the transmission curve on two-photon resonance predicted by the mean-field model is dominated by the variance $\theta_R$, we show in Fig. D.1(a) the Autler-Townes transmission spectra for three different detunings $\Delta_c/2\pi = \{9, 0, -9\}$ MHz. These spectra correspond to the points marked on the curves on two-photon resonance depicted in Fig. D.1(b). The mean-field model with (without, $\theta_R = 0$) the variance $\theta_R$ is shown in blue (purple) and the result of the MCRE simulation is shown in orange for comparison.

For positive single-photon detunings $\Delta > 0$, where $\alpha$ is larger, the mean-field model and the MCRE model almost agree for the Autler-Townes spectrum with $\Delta_c/2\pi = -9\,\mathrm{MHz}$. Setting $\theta_R = 0$ makes them almost identical. For zero and negative single-photon detunings, $\alpha$ is smaller and a deviation between the mean-field model and the MCRE model is apparent. Completely excluding the variance of the interaction-induced level shift ($\theta_R = 0$) makes the result of the two models similar, but seems to underestimate the absorption compared to the MCRE model. This highlights the importance of including a spatial variation of the level shift in an appropriate manner.

Overall, the considered mean-field model is dominated by the variance $\theta_R$ of the average interaction-induced level shift, whenever $\alpha$ is small. This is the case

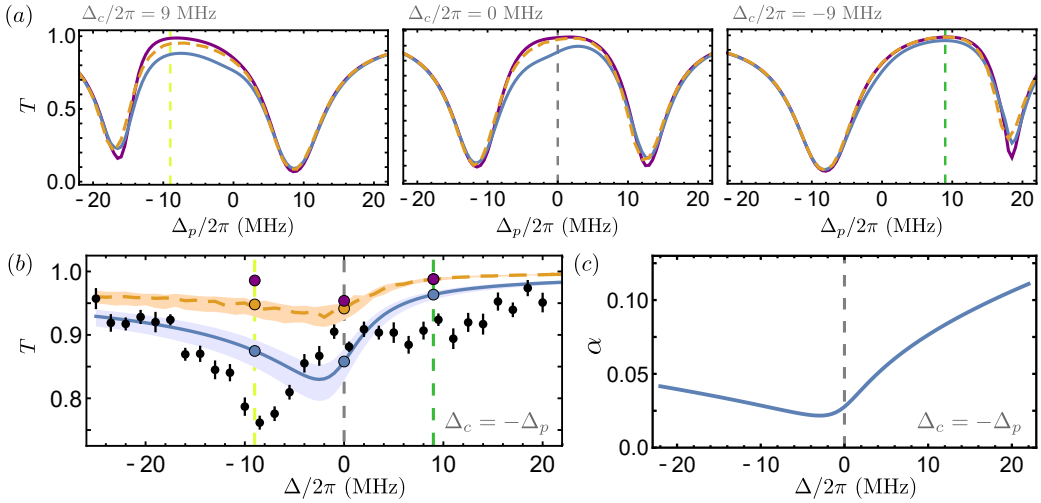


**Figure D.1: Comparison of the mean-field model [for $\theta_R \neq 0$ (blue solid lines) and $\theta_R = 0$ (purple solid lines)] and the MCRE simulation (orange dashed lines) for the parameters of Fig. 4.17.** (a) Autler-Townes transmission spectra as a function of the probe beam detuning $\Delta_p$ for different control beam detunings $\Delta_c/2\pi = \{9, 0, -9\}$ MHz. (b) Transmission $T$ against the single-photon detuning $\Delta$ on two-photon resonance ($\Delta_c = -\Delta_p$), as in Fig. 4.17. Black points depict the measured spectrum and the result of the two theoretical models are shown. Colored circles indicate the transmission values of the corresponding Autler-Townes spectrum in (a). (c) Plot of $\alpha$ of the mean-field model against the single-photon detuning $\Delta$. For all theoretical curves the parameters are the same as in Fig. 4.17. For a discussion of the curves see the main text. Figure and caption with permission taken from [97].

when the fraction of blockaded atoms excluding Rydberg excitations is small. In this regime, in which our two-photon measurement mainly have been performed, deviations between the mean-field model and the MCRE simulation become apparent.

# List of figures

# Bibliography


[1] A. L. Schawlow and C. H. Townes, *Infrared and Optical Masers*, Phys. Rev. **112**, 1940 (1958).

[2] T. H. Maiman, *Stimulated Optical Radiation in Ruby*, Nature **187**, 493 (1960).

[3] W. D. Phillips, *Nobel Lecture: Laser cooling and trapping of neutral atoms*, Rev. Mod. Phys. **70**, 721 (1998).

[4] D. E. Chang, V. Vuletić, and M. D. Lukin, *Quantum nonlinear optics — photon by photon*, Nat. Photon. **8**, 685 (2014).

[5] I. Carusotto and C. Ciuti, *Quantum fluids of light*, Rev. Mod. Phys. **85**, 299 (2013).

[6] J. Otterbach, M. Moos, D. Muth, and M. Fleischhauer, *Wigner Crystallization of Single Photons in Cold Rydberg Ensembles*, Phys. Rev. Lett. **111**, 113001 (2013).

[7] D. Paredes-Barato and C. S. Adams, *All-Optical Quantum Information Processing Using Rydberg Gates*, Phys. Rev. Lett. **112**, 040501 (2014).

[8] D. Tiarks, S. Schmidt, G. Rempe, and S. Dürr, *Optical $\pi$ phase shift created with a single-photon pulse*, Sci. Adv. **2**, e1600036 (2016).

[9] H. Gorniaczyk, C. Tresp, P. Bienias, A. Paris-Mandoki, W. Li, I. Mirgorodskiy, H. Büchler, I. Lesanovsky, and S. Hofferberth, *Enhancement of Rydberg-mediated single-photon nonlinearities by electrically tuned Förster resonances*, Nat. Commun. **7**, 12480 (2016).

[10] D. Tiarks, S. Schmidt-Eberle, T. Stolz, G. Rempe, and S. Dürr, *A photon–photon quantum gate based on Rydberg interactions*, Nat. Phys. **15**, 124 (2019).

[11] R. Y. Chiao, E. Garmire, and C. H. Townes, *Self-Trapping of Optical Beams*, Phys. Rev. Lett. **13**, 479 (1964).

[12] P. A. Franken, A. E. Hill, C. W. Peters, and G. Weinreich, *Generation of Optical Harmonics*, Phys. Rev. Lett. **7**, 118 (1961).

[13] A. McPherson, G. Gibson, H. Jara, U. Johann, T. S. Luk, I. A. McIntyre, K. Boyer, and C. K. Rhodes, *Studies of multiphoton production of vacuum-ultraviolet radiation in the rare gases*, J. Opt. Soc. Am. B **4**, 595 (1987).

[14] M. Ferray, A. L'Huillier, X. F. Li, L. A. Lompre, G. Mainfray, and C. Manus, *Multiple-harmonic conversion of 1064 nm radiation in rare gases*, J. Phys. B **21**, L31 (1988).

[15] K. M. Birnbaum, A. Boca, R. Miller, A. D. Boozer, T. E. Northup, and H. J. Kimble, *Photon blockade in an optical cavity with one trapped atom*, Nature **436**, 87 (2005).

[16] W. Chen, K. M. Beck, R. Bücker, M. Gullans, M. D. Lukin, H. Tanji-Suzuki, and V. Vuletić, *All-Optical Switch and Transistor Gated by One Stored Photon*, Science **341**, 768 (2013).

[17] I. Fushman, D. Englund, A. Faraon, N. Stoltz, P. Petroff, and J. Vučković, *Controlled Phase Shifts with a Single Quantum Dot*, Science **320**, 769 (2008).

[18] L. Wells, S. Kalliakos, B. Villa, D. Ellis, R. Stevenson, A. Bennett, I. Farrer, D. Ritchie, and A. Shields, *Photon Phase Shift at the Few-Photon Level and Optical Switching by a Quantum Dot in a Microcavity*, Phys. Rev. Applied **11**, 061001 (2019).

[19] S. E. Harris, J. E. Field, and A. Imamoğlu, *Nonlinear optical processes using electromagnetically induced transparency*, Phys. Rev. Lett. **64**, 1107 (1990).

[20] K.-J. Boller, A. Imamoğlu, and S. E. Harris, *Observation of electromagnetically induced transparency*, Phys. Rev. Lett. **66**, 2593 (1991).

[21] I. Friedler, D. Petrosyan, M. Fleischhauer, and G. Kurizki, *Long-range interactions and entanglement of slow single-photon pulses*, Phys. Rev. A **72**, 043803 (2005).

[22] A. K. Mohapatra, T. R. Jackson, and C. S. Adams, *Coherent Optical Detection of Highly Excited Rydberg States Using Electromagnetically Induced Transparency*, Phys. Rev. Lett. **98**, 113003 (2007).

[23] J. D. Pritchard, D. Maxwell, A. Gauguet, K. J. Weatherill, M. P. A. Jones, and C. S. Adams, *Cooperative Atom-Light Interaction in a Blockaded Rydberg Ensemble*, Phys. Rev. Lett. **105**, 193603 (2010).

[24] T. Peyronel, O. Firstenberg, Q.-Y. Liang, S. Hofferberth, A. V. Gorshkov, T. Pohl, M. D. Lukin, and V. Vuletić, *Quantum nonlinear optics with single photons enabled by strongly interacting atoms*, Nature **488**, 57 (2012).

[25] L. V. Hau, S. E. Harris, Z. Dutton, and C. H. Behroozi, *Light speed reduction to 17 metres per second in an ultracold atomic gas*, Nature **397**, 594 (1999).

[26] M. Fleischhauer and M. D. Lukin, *Dark-State Polaritons in Electromagnetically Induced Transparency*, Phys. Rev. Lett. **84**, 5094 (2000).

[27] C. Liu, Z. Dutton, C. H. Behroozi, and L. V. Hau, *Observation of coherent optical information storage in an atomic medium using halted light pulses*, Nature **409**, 490 (2001).

[28] D. F. Phillips, A. Fleischhauer, A. Mair, R. L. Walsworth, and M. D. Lukin, *Storage of Light in Atomic Vapor*, Phys. Rev. Lett. **86**, 783 (2001).

[29] M. D. Eisaman, A. André, F. Massou, M. Fleischhauer, A. S. Zibrov, and M. D. Lukin, *Electromagnetically induced transparency with tunable single-photon pulses*, Nature **438**, 837 (2005).

[30] M. Fleischhauer and M. D. Lukin, *Quantum memory for photons: Dark-state polaritons*, Phys. Rev. A **65**, 022314 (2002).

[31] A. André and M. D. Lukin, *Manipulating Light Pulses via Dynamically Controlled Photonic Band gap*, Phys. Rev. Lett. **89**, 143602 (2002).

[32] M. Bajcsy, A. S. Zibrov, and M. D. Lukin, *Stationary pulses of light in an atomic medium*, Nature **426**, 638 (2003).

[33] A. André, M. Bajcsy, A. S. Zibrov, and M. D. Lukin, *Nonlinear Optics with Stationary Pulses of Light*, Phys. Rev. Lett. **94**, 063902 (2005).

[34] F. E. Zimmer, J. Otterbach, R. G. Unanyan, B. W. Shore, and M. Fleischhauer, *Dark-state polaritons for multicomponent and stationary light fields*, Phys. Rev. A **77**, 063823 (2008).

[35] Y.-W. Lin, W.-T. Liao, T. Peters, H.-C. Chou, J.-S. Wang, H.-W. Cho, P.-C. Kuan, and I. A. Yu, *Stationary Light Pulses in Cold Atomic Media and without Bragg Gratings*, Phys. Rev. Lett. **102**, 213601 (2009).

[36] K.-K. Park, Y.-W. Cho, Y.-T. Chough, and Y.-H. Kim, *Experimental Demonstration of Quantum Stationary Light Pulses in an Atomic Ensemble*, Phys. Rev. X **8**, 021016 (2018).

[37] J. L. Everett, D. B. Higginbottom, G. T. Campbell, P. K. Lam, and B. C. Buchler, *Stationary Light in Atomic Media*, Adv. Quantum Technol. **2**, 1800100 (2019).

[38] S. A. Moiseev and B. S. Ham, *Generation of entangled lights with temporally reversed photon wave packets*, Phys. Rev. A **71**, 053802 (2005).

[39] K. R. Hansen and K. Mølmer, *Trapping of light pulses in ensembles of stationary Λ atoms*, Phys. Rev. A **75**, 053802 (2007).

[40] K. R. Hansen and K. Mølmer, *Stationary light pulses in ultracold atomic gases*, Phys. Rev. A **75**, 065804 (2007).

[41] G. Nikoghosyan and M. Fleischhauer, *Stationary light in cold-atomic gases*, Phys. Rev. A **80**, 013818 (2009).

[42] F. Zimmer, A. André, M. Lukin, and M. Fleischhauer, *Coherent control of stationary light pulses*, Opt. Commun. **264**, 441 (2006).

[43] T. Peters, S.-W. Su, Y.-H. Chen, J.-S. Wang, S.-C. Gou, and I. A. Yu, *Formation of stationary light in a medium of nonstationary atoms*, Phys. Rev. A **85**, 023838 (2012).

[44] M. Fleischhauer, J. Otterbach, and R. G. Unanyan, *Bose-Einstein Condensation of Stationary-Light Polaritons*, Phys. Rev. Lett. **101**, 163601 (2008).

[45] D. Chang, V. Gritsev, G. Morigi, V. Vuletić, M. Lukin, and E. Demler, *Crystallization of strongly interacting photons in a nonlinear optical fibre*, Nat. Phys. **4**, 884 (2008).

[46] T. F. Gallagher, *Rydberg atoms*, Cambridge Monographs on Atomic, Molecular and Chemical Physics (Cambridge University Press, 2005).

[47] T. F. Gallagher and P. Pillet, *Dipole–Dipole Interactions of Rydberg Atoms*, in *Adv. At. Mol. Opt. Phys.*, Vol. 56 (Academic Press, 2008) pp. 161–218.

[48] D. Comparat and P. Pillet, *Dipole blockade in a cold Rydberg atomic sample*, J. Opt. Soc. Am. B **27**, A208 (2010).

[49] R. Löw, H. Weimer, J. Nipper, J. B. Balewski, B. Butscher, H. P. Büchler, and T. Pfau, *An experimental and theoretical guide to strongly interacting Rydberg gases*, J. Phys. B **45**, 113001 (2012).

[50] H. Weimer, M. Müller, I. Lesanovsky, P. Zoller, and H. P. Büchler, *A Rydberg quantum simulator*, Nat. Phys. **6**, 382 (2010).

[51] A. Browaeys and T. Lahaye, *Many-body physics with individually controlled Rydberg atoms*, Nat. Phys. **16**, 132 (2020).

[52] C. S. Adams, J. D. Pritchard, and J. P. Shaffer, *Rydberg atom quantum technologies*, J. Phys. B **53**, 012002 (2019).

[53] M. Saffman, T. G. Walker, and K. Mølmer, *Quantum information with Rydberg atoms*, Rev. Mod. Phys. **82**, 2313 (2010).

[54] M. D. Lukin, M. Fleischhauer, R. Cote, L. M. Duan, D. Jaksch, J. I. Cirac, and P. Zoller, *Dipole Blockade and Quantum Information Processing in Mesoscopic Atomic Ensembles*, Phys. Rev. Lett. **87**, 037901 (2001).

[55] K. Singer, M. Reetz-Lamour, T. Amthor, L. G. Marcassa, and M. Weidemüller, *Suppression of Excitation and Spectral Broadening Induced by Interactions in a Cold Gas of Rydberg Atoms*, Phys. Rev. Lett. **93**, 163001 (2004).

[56] D. Tong, S. M. Farooqi, J. Stanojevic, S. Krishnan, Y. P. Zhang, R. Côté, E. E. Eyler, and P. L. Gould, *Local Blockade of Rydberg Excitation in an Ultracold Gas*, Phys. Rev. Lett. **93**, 063001 (2004).

[57] O. Firstenberg, T. Peyronel, Q.-Y. Liang, A. V. Gorshkov, M. D. Lukin, and V. Vuletić, *Attractive photons in a quantum nonlinear medium*, Nature **502**, 71 (2013).

[58] S. Sevinçli, N. Henkel, C. Ates, and T. Pohl, *Nonlocal Nonlinear Optics in Cold Rydberg Gases*, Phys. Rev. Lett. **107**, 153001 (2011).

[59] H. Busche, P. Huillery, S. W. Ball, T. Ilieva, M. P. Jones, and C. S. Adams, *Contactless nonlinear optics mediated by long-range Rydberg interactions*, Nat. Phys. **13**, 655 (2017).

[60] K. J. Weatherill, J. D. Pritchard, R. P. Abel, M. G. Bason, A. K. Mohapatra, and C. S. Adams, *Electromagnetically induced transparency of an interacting cold Rydberg ensemble*, J. Phys. B **41**, 201002 (2008).

[61] J. D. Pritchard, A. Gauguet, K. J. Weatherill, and C. S. Adams, *Optical non-linearity in a dynamical Rydberg gas*, J. Phys. B **44**, 184019 (2011).

[62] S. Sevinçli, C. Ates, T. Pohl, H. Schempp, C. S. Hofmann, G. Günter, T. Amthor, M. Weidemüller, J. D. Pritchard, D. Maxwell, A. Gauguet, K. J. Weatherill, M. P. A. Jones, and C. S. Adams, *Quantum interference in interacting three-level Rydberg gases: coherent population trapping and electromagnetically induced transparency*, J. Phys. B **44**, 184018 (2011).

[63] J. D. Pritchard, K. J. Weatherill, and C. S. Adams, *Nonlinear optics using cold Rydberg atom*, in *Annu. Rev. Cold At. Mol.* (2013) pp. 301–350.

[64] J. Han, T. Vogt, and W. Li, *Spectral shift and dephasing of electromagnetically induced transparency in an interacting Rydberg gas*, Phys. Rev. A **94**, 043806 (2016).

[65] B. J. DeSalvo, J. A. Aman, C. Gaul, T. Pohl, S. Yoshida, J. Burgdörfer, K. R. A. Hazzard, F. B. Dunning, and T. C. Killian, *Rydberg-blockade effects in Autler-Townes spectra of ultracold strontium*, Phys. Rev. A **93**, 022709 (2016).

[66] G. Günter, M. Robert-de Saint-Vincent, H. Schempp, C. S. Hofmann, S. Whitlock, and M. Weidemüller, *Interaction Enhanced Imaging of Individual Rydberg Atoms in Dense Gases*, Phys. Rev. Lett. **108**, 013002 (2012).

[67] G. Günter, H. Schempp, M. Robert-de Saint-Vincent, V. Gavryusev, S. Helmrich, C. S. Hofmann, S. Whitlock, and M. Weidemüller, *Observing the Dynamics of Dipole-Mediated Energy Transport by Interaction-Enhanced Imaging*, Science **342**, 954 (2013).

[68] J. A. Sedlacek, A. Schwettmann, H. Kübler, R. Löw, T. Pfau, and J. P. Shaffer, *Microwave electrometry with Rydberg atoms in a vapour cell using bright atomic resonances*, Nat. Phys. **8**, 819 (2012).

[69] H. Fan, S. Kumar, J. Sedlacek, H. Kübler, S. Karimkashi, and J. P. Shaffer, *Atom based RF electric field sensing*, J. Phys. B **48**, 202001 (2015).

[70] J. D. Thompson, T. L. Nicholson, Q.-Y. Liang, S. H. Cantu, A. V. Venkatramani, S. Choi, I. A. Fedorov, D. Viscor, T. Pohl, M. D. Lukin, and V. Vuletić, *Symmetry-protected collisions between strongly interacting photons*, Nature **542**, 206 (2017).

[71] Q.-Y. Liang, A. V. Venkatramani, S. H. Cantu, T. L. Nicholson, M. J. Gullans, A. V. Gorshkov, J. D. Thompson, C. Chin, M. D. Lukin, and V. Vuletić, *Observation of three-photon bound states in a quantum nonlinear medium*, Science **359**, 783 (2018).

[72] N. Stiesdal, J. Kumlin, K. Kleinbeck, P. Lunt, C. Braun, A. Paris-Mandoki, C. Tresp, H. P. Büchler, and S. Hofferberth, *Observation of Three-Body Correlations for Photons Coupled to a Rydberg Superatom*, Phys. Rev. Lett. **121**, 103601 (2018).

[73] S. H. Cantu, A. V. Venkatramani, W. Xu, L. Zhou, B. Jelenković, M. D. Lukin, and V. Vuletić, *Repulsive photons in a quantum nonlinear medium*, Nat. Phys. **16**, 921 (2020).

[74] S. Baur, D. Tiarks, G. Rempe, and S. Dürr, *Single-Photon Switch Based on Rydberg Blockade*, Phys. Rev. Lett. **112**, 073901 (2014).

[75] H. Gorniaczyk, C. Tresp, J. Schmidt, H. Fedder, and S. Hofferberth, *Single-Photon Transistor Mediated by Interstate Rydberg Interactions*, Phys. Rev. Lett. **113**, 053601 (2014).

[76] D. Tiarks, S. Baur, K. Schneider, S. Dürr, and G. Rempe, *Single-Photon Transistor Using a Förster Resonance*, Phys. Rev. Lett. **113**, 053602 (2014).

[77] C. Murray and T. Pohl, *Chapter Seven - Quantum and Nonlinear Optics in Strongly Interacting Atomic Ensembles*, in *Adv. At. Mol. Opt. Phys.*, Vol. 65, edited by E. Arimondo, C. C. Lin, and S. F. Yelin (Academic Press, 2016) pp. 321–372.

[78] M. Gärttner and J. Evers, *Nonlinear absorption and density-dependent dephasing in Rydberg electromagnetically-induced-transparency media*, Phys. Rev. A **88**, 033417 (2013).

[79] M. Gärttner, S. Whitlock, D. W. Schönleber, and J. Evers, *Collective Excitation of Rydberg-Atom Ensembles beyond the Superatom Model*, Phys. Rev. Lett. **113**, 233002 (2014).

[80] S.-S. Hsiao, K.-T. Chen, and I. A. Yu, *Mean field theory of weakly-interacting Rydberg polaritons in the EIT system based on the nearest-neighbor distribution*, Opt. Express **28**, 28414 (2020).

[81] C. Ates, T. Pohl, T. Pattard, and J. M. Rost, *Many-body theory of excitation dynamics in an ultracold Rydberg gas*, Phys. Rev. A **76**, 013413 (2007).

[82] C. Ates, S. Sevinçli, and T. Pohl, *Electromagnetically induced transparency in strongly interacting Rydberg gases*, Phys. Rev. A **83**, 041802 (2011).

[83] K. P. Heeg, M. Gärttner, and J. Evers, *Hybrid model for Rydberg gases including exact two-body correlations*, Phys. Rev. A **86**, 063421 (2012).

[84] H. Schempp, G. Günter, C. S. Hofmann, C. Giese, S. D. Saliba, B. D. DePaola, T. Amthor, M. Weidemüller, S. Sevinçli, and T. Pohl, *Coherent Population Trapping with Controlled Interparticle Interactions*, Phys. Rev. Lett. **104**, 173602 (2010).

[85] O. Firstenberg, C. S. Adams, and S. Hofferberth, *Nonlinear quantum optics mediated by Rydberg interactions*, J. Phys. B **49**, 152003 (2016).

[86] O. Lahad and O. Firstenberg, *Induced Cavities for Photonic Quantum Gates*, Phys. Rev. Lett. **119**, 113601 (2017).

[87] V. Parigi, E. Bimbard, J. Stanojevic, A. J. Hilliard, F. Nogrette, R. Tualle-Brouri, A. Ourjoumtsev, and P. Grangier, *Observation and Measurement of Interaction-Induced Dispersive Optical Nonlinearities in an Ensemble of Cold Rydberg Atoms*, Phys. Rev. Lett. **109**, 233602 (2012).

[88] J. Ningyuan, A. Georgakopoulos, A. Ryou, N. Schine, A. Sommer, and J. Simon, *Observation and characterization of cavity Rydberg polaritons*, Phys. Rev. A **93**, 041802(R) (2016).

[89] R. Boddeda, I. Usmani, E. Bimbard, A. Grankin, A. Ourjoumtsev, E. Brion, and P. Grangier, *Rydberg-induced optical nonlinearities from a cold atomic ensemble trapped inside a cavity*, J. Phys. B **49**, 084005 (2016).

[90] N. Jia, N. Schine, A. Georgakopoulos, A. Ryou, L. W. Clark, A. Sommer, and J. Simon, *A strongly interacting polaritonic quantum dot*, Nat. Phys. **14**, 550 (2018).

[91] L. W. Clark, N. Schine, C. Baum, N. Jia, and J. Simon, *Observation of Laughlin states made of light*, Nature **582**, 41 (2020).

[92] Y.-H. Chen, M.-J. Lee, W. Hung, Y.-C. Chen, Y.-F. Chen, and I. A. Yu, *Demonstration of the Interaction between Two Stopped Light Pulses*, Phys. Rev. Lett. **108**, 173603 (2012).

[93] E. Distante, A. Padrón-Brito, M. Cristiani, D. Paredes-Barato, and H. de Riedmatten, *Storage Enhanced Nonlinearities in a Cold Atomic Rydberg Ensemble*, Phys. Rev. Lett. **117**, 113001 (2016).

[94] G. Nikoghosyan, F. E. Zimmer, and M. B. Plenio, *Dipolar Bose-Einstein condensate of dark-state polaritons*, Phys. Rev. A **86**, 023854 (2012).

[95] H. Pimenta, A. Z. Goldberg, J. Sinclair, and K. Bonsma-Fisher, *Simulating one-dimensional systems with stationary Rydberg dark polaritons* (2018), arXiv:1803.07565 [quant-ph] .

[96] A. Tebben, C. Hainaut, V. Walther, Y.-C. Zhang, G. Zürn, T. Pohl, and M. Weidemüller, *Blockade-induced resonant enhancement of the optical nonlinearity in a Rydberg medium*, Phys. Rev. A **100**, 063812 (2019).

[97] A. Tebben, C. Hainaut, A. Salzinger, S. Geier, T. Franz, T. Pohl, M. Gärttner, G. Zürn, and M. Weidemüller, *Nonlinear absorption in interacting Rydberg electromagnetically-induced-transparency spectra on two-photon resonance*, Phys. Rev. A **103**, 063710 (2021).

[98] A. Tebben, C. Hainaut, A. Salzinger, T. Franz, S. Geier, G. Zürn, and M. Weidemüller, *A stationary Rydberg polariton* (2021), arXiv:2108.00657 [quant-ph] .

[99] M. Fleischhauer, A. Imamoglu, and J. P. Marangos, *Electromagnetically induced transparency: Optics in coherent media*, Rev. Mod. Phys. **77**, 633 (2005).

[100] S. E. Harris, J. E. Field, and A. Kasapi, *Dispersive properties of electromagnetically induced transparency*, Phys. Rev. A **46**, R29(R) (1992).

[101] T. Chanelière, D. Matsukevich, S. Jenkins, S.-Y. Lan, T. Kennedy, and A. Kuzmich, *Storage and retrieval of single photons transmitted between remote quantum memories*, Nature **438**, 833 (2005).

[102] B. E. Saleh and M. C. Teich, *Fundamentals of Photonics*, 2nd ed., Wiley Series in Pure and Applied Optics Ser., Vol. 81 (John Wiley & Sons, Incorporated, 2013).

[103] G. G. Günter, *Interfacing Rydberg atoms with light and observing their interaction driven dynamics*, Ph.D. thesis, Heidelberg University (2014).

[104] M. Gärttner, *Many-Body Effects in Rydberg Gases : Coherent Dynamics of Strongly Interacting Two-Level Atoms and Nonlinear Optical Response of a Rydberg Gas in EIT Configuration*, Ph.D. thesis, Heidelberg University (2013).

[105] M. O. Scully and M. S. Zubairy, *Quantum Optics* (Cambridge University Press, Cambridge, 1997).

[106] H. Schempp, *Formation of Aggregates and Energy Transport in Ultracold Rydberg Interacting Gases*, Ph.D. thesis, Heidelberg University (2014).

[107] S. Sultana and M. S. Zubairy, *Effect of finite bandwidth on refractive-index enhancement and lasing without inversion*, Phys. Rev. A **49**, 438 (1994).

[108] H.-P. Breuer and F. Petruccione, *The Theory of Open Quantum Systems* (Oxford University Press, New York, 2002).

[109] D. A. Steck, *Quantum and Atom Optics*, available online at http://steck.us/teaching (revision 0.13.4, 24 September 2020).

[110] V. Gavryusev, A. Signoles, M. Ferreira-Cao, G. Zürn, C. S. Hofmann, G. Günter, H. Schempp, M. R. de Saint-Vincent, S. Whitlock, and M. Weidemüller, *Density matrix reconstruction of three-level atoms via Rydberg electromagnetically induced transparency*, J. Phys. B **49**, 164002 (2016).

[111] J. E. Field, K. H. Hahn, and S. E. Harris, *Observation of electromagnetically induced transparency in collisionally broadened lead vapor*, Phys. Rev. Lett. **67**, 3062 (1991).

[112] A. V. Turukhin, V. S. Sudarshanam, M. S. Shahriar, J. A. Musser, B. S. Ham, and P. R. Hemmer, *Observation of Ultraslow and Stored Light Pulses in a Solid*, Phys. Rev. Lett. **88**, 023602 (2001).

[113] A. V. Gorshkov, A. André, M. D. Lukin, and A. S. Sørensen, *Photon storage in Λ-type optically dense atomic media. II. Free-space model*, Phys. Rev. A **76**, 033805 (2007).

[114] J. S. Otterbach, *Single- and Many-Body Phenomena of Dark-State Polaritons*, Ph.D. thesis, Technische Universität Kaiserslautern (2011).

[115] A. V. Gorshkov, J. Otterbach, M. Fleischhauer, T. Pohl, and M. D. Lukin, *Photon-Photon Interactions via Rydberg Blockade*, Phys. Rev. Lett. **107**, 133602 (2011).

[116] A. V. Gorshkov, R. Nath, and T. Pohl, *Dissipative Many-Body Quantum Optics in Rydberg Media*, Phys. Rev. Lett. **110**, 153601 (2013).

[117] C. R. Murray and T. Pohl, *Coherent Photon Manipulation in Interacting Atomic Ensembles*, Phys. Rev. X **7**, 031007 (2017).

[118] P. Bienias and H. P. Büchler, *Quantum theory of Kerr nonlinearity with Rydberg slow light polaritons*, New J. Phys. **18**, 123026 (2016).

[119] F. Zimmer, *Matter-wave Optics of Dark-state Polaritons: Applications to Interferometry and Quantum Information*, Ph.D. thesis, Technische Universität Kaiserslautern (2006).

[120] T. Peters, T.-P. Wang, A. Neumann, L. S. Simeonov, and T. Halfmann, *Single-photon-level narrowband memory in a hollow-core photonic bandgap fiber*, Opt. Express **28**, 5340 (2020).

[121] A. Tebben, *Resonant Enhancement of the Optical Nonlinearity in a Rydberg Gas*, Master's thesis, Heidelberg University (2018).

[122] R. W. Boyd, *Nonlinear optics*, 2nd ed. (Academic Press, Elsevier Inc., 2003).

[123] P. A. Franken and J. F. Ward, *Optical Harmonics and Nonlinear Phenomena*, Rev. Mod. Phys. **35**, 23 (1963).

[124] D. Petrosyan, J. Otterbach, and M. Fleischhauer, *Electromagnetically Induced Transparency with Rydberg Atoms*, Phys. Rev. Lett. **107**, 213601 (2011).

[125] M. Gärttner, S. Whitlock, D. W. Schönleber, and J. Evers, *Semianalytical model for nonlinear absorption in strongly interacting Rydberg gases*, Phys. Rev. A **89**, 063407 (2014).

[126] C. Gaul, B. J. DeSalvo, J. A. Aman, F. B. Dunning, T. C. Killian, and T. Pohl, *Resonant Rydberg Dressing of Alkaline-Earth Atoms via Electromagnetically Induced Transparency*, Phys. Rev. Lett. **116**, 243001 (2016).

[127] S. Helmrich, A. Arias, N. Pehoviak, and S. Whitlock, *Two-body interactions and decay of three-level Rydberg-dressed atoms*, J. Phys. B **49**, 03LT02 (2016).

[128] J. R. Rydberg Ph.D., *XXXIV. On the structure of the line-spectra of the chemical elements*, Philos. Mag. **29**, 331 (1890).

[129] C. S. Hofmann, G. Günter, H. Schempp, N. L. M. Müller, A. Faber, H. Busche, M. Robert-de Saint-Vincent, S. Whitlock, and M. Weidemüller, *An experimental approach for investigating many-body phenomena in Rydberg-interacting quantum systems*, Front. Phys. **9**, 571 (2014).

[130] N. Šibalić, J. Pritchard, C. Adams, and K. Weatherill, *ARC: An open-source library for calculating properties of alkali Rydberg atoms*, Comput. Phys. Commun. **220**, 319 (2017).

[131] R. J. Le Roy, *Long-Range Potential Coefficients From RKR Turning Points: $C_6$ and $C_8$ for $B(^3\Pi_{Ou}{}^+)$-State $Cl_2$, $Br_2$, and $I_2$* , Can. J. Phys. **52**, 246 (1974).

[132] T. G. Walker and M. Saffman, *Consequences of Zeeman degeneracy for the van der Waals blockade between Rydberg atoms*, Phys. Rev. A **77**, 032723 (2008).

[133] C. S. Hofmann, *Emergence of correlations in strongly interacting ultracold Rydberg gases*, Ph.D. thesis, Heidelberg University (2013).

[134] W. Li, P. J. Tanner, and T. F. Gallagher, *Dipole-Dipole Excitation and Ionization in an Ultracold Gas of Rydberg Atoms*, Phys. Rev. Lett. **94**, 173001 (2005).

[135] A. Chotia, M. Viteau, T. Vogt, D. Comparat, and P. Pillet, *Kinetic Monte Carlo modeling of dipole blockade in Rydberg excitation experiment*, New J. Phys. **10**, 045031 (2008).

[136] H. Weimer, R. Löw, T. Pfau, and H. P. Büchler, *Quantum Critical Behavior in Strongly Interacting Rydberg Gases*, Phys. Rev. Lett. **101**, 250601 (2008).

[137] Y. O. Dudin and A. Kuzmich, *Strongly Interacting Rydberg Excitations of a Cold Atomic Gas*, Science **336**, 887 (2012).

[138] F. Ripka, H. Kübler, R. Löw, and T. Pfau, *A room-temperature single-photon source based on strongly interacting Rydberg atoms*, Science **362**, 446 (2018).

[139] D. P. Ornelas-Huerta, A. N. Craddock, E. A. Goldschmidt, A. J. Hachtel, Y. Wang, P. Bienias, A. V. Gorshkov, S. L. Rolston, and J. V. Porto, *On-demand indistinguishable single photons from an efficient and pure source based on a Rydberg ensemble*, Optica **7**, 813 (2020).

[140] C. Tresp, C. Zimmer, I. Mirgorodskiy, H. Gorniaczyk, A. Paris-Mandoki, and S. Hofferberth, *Single-Photon Absorber Based on Strongly Interacting Rydberg Atoms*, Phys. Rev. Lett. **117**, 223001 (2016).

[141] D. Maxwell, D. J. Szwer, D. Paredes-Barato, H. Busche, J. D. Pritchard, A. Gauguet, K. J. Weatherill, M. P. A. Jones, and C. S. Adams, *Storage and Control of Optical Photons Using Rydberg Polaritons*, Phys. Rev. Lett. **110**, 103001 (2013).

[142] D. Maxwell, D. J. Szwer, D. Paredes-Barato, H. Busche, J. D. Pritchard, A. Gauguet, M. P. A. Jones, and C. S. Adams, *Microwave control of the interaction between two optical photons*, Phys. Rev. A **89**, 043827 (2014).

[143] P. Bienias, J. Douglas, A. Paris-Mandoki, P. Titum, I. Mirgorodskiy, C. Tresp, E. Zeuthen, M. J. Gullans, M. Manzoni, S. Hofferberth, D. Chang, and A. V. Gorshkov, *Photon propagation through dissipative Rydberg media at large input rates*, Phys. Rev. Research **2**, 033049 (2020).

[144] P. Bienias, S. Choi, O. Firstenberg, M. F. Maghrebi, M. Gullans, M. D. Lukin, A. V. Gorshkov, and H. P. Büchler, *Scattering resonances and bound states for strongly interacting Rydberg polaritons*, Phys. Rev. A **90**, 053804 (2014).

[145] M. J. Gullans, J. D. Thompson, Y. Wang, Q.-Y. Liang, V. Vuletić, M. D. Lukin, and A. V. Gorshkov, *Effective Field Theory for Rydberg Polaritons*, Phys. Rev. Lett. **117**, 113601 (2016).

[146] E. Zeuthen, M. J. Gullans, M. F. Maghrebi, and A. V. Gorshkov, *Correlated Photon Dynamics in Dissipative Rydberg Media*, Phys. Rev. Lett. **119**, 043602 (2017).

[147] M. T. Manzoni, D. E. Chang, and J. S. Douglas, *Simulating quantum light propagation through atomic ensembles using matrix product states*, Nat. Commun. **8**, 1743 (2017).

[148] T. Pistorius, J. Kazemi, and H. Weimer, *Quantum Many-Body Dynamics of Driven-Dissipative Rydberg Polaritons*, Phys. Rev. Lett. **125**, 263604 (2020).

[149] M. Moos, M. Höning, R. Unanyan, and M. Fleischhauer, *Many-body physics of Rydberg dark-state polaritons in the strongly interacting regime*, Phys. Rev. A **92**, 053846 (2015).

[150] T. Caneva, M. T. Manzoni, T. Shi, J. S. Douglas, J. I. Cirac, and D. E. Chang, *Quantum dynamics of propagating photons with strong interactions: a generalized input–output formalism*, New J. Phys. **17**, 113001 (2015).

[151] C. R. Murray, I. Mirgorodskiy, C. Tresp, C. Braun, A. Paris-Mandoki, A. V. Gorshkov, S. Hofferberth, and T. Pohl, *Photon Subtraction by Many-Body Decoherence*, Phys. Rev. Lett. **120**, 113601 (2018).

[152] F. Yang, Y.-C. Liu, and L. You, *Atom-Photon Spin-Exchange Collisions Mediated by Rydberg Dressing*, Phys. Rev. Lett. **125**, 143601 (2020).

[153] M. Khazali, C. R. Murray, and T. Pohl, *Polariton Exchange Interactions in Multichannel Optical Networks*, Phys. Rev. Lett. **123**, 113605 (2019).

[154] J. E. Johnson and S. L. Rolston, *Interactions between Rydberg-dressed atoms*, Phys. Rev. A **82**, 033412 (2010).

[155] S. MacNamara and G. Strang, *Operator splitting*, in *Splitting Methods in Communication, Imaging, Science, and Engineering*, edited by R. Glowinski, S. J. Osher, and W. Yin (Springer, Cham, 2016) pp. 95–114.

[156] G. Agrawal, *Nonlinear Fiber Optics*, 6th ed. (Academic Press, Elsevier, 2019) pp. 46–50.

[157] I. V. Hertel and C.-P. Schulz, *Atoms, Molecules and Optical Physics 1* (Springer-Verlag Berlin Heidelberg, 2015).

[158] M. S. O'Sullivan and B. P. Stoicheff, *Scalar polarizabilities and avoided crossings of high Rydberg states in Rb*, Phys. Rev. A **31**, 2718 (1985).

[159] W. Happer, *Optical Pumping*, Rev. Mod. Phys. **44**, 169 (1972).

[160] C. Zener and R. H. Fowler, *Non-adiabatic crossing of energy levels*, Proc. R. Soc. Lond. A **137**, 696 (1932).

[161] H. J. Metcalf and P. van der Straten, *Laser Cooling and Trapping of Neutral Atoms*, in *The Optics Encyclopedia*, edited by T. Brown, K. Creath, H. Kogelnik, M. Kriss, J. Schmit, and M. Weber (American Cancer Society, 2007).

[162] K. Dieckmann, R. J. C. Spreeuw, M. Weidemüller, and J. T. M. Walraven, *Two-dimensional magneto-optical trap as a source of slow atoms*, Phys. Rev. A **58**, 3891 (1998).

[163] B. Höltkemeier, *2D-MOT as a source of a cold atom target*, Diploma thesis, Heidelberg University (2011).

[164] H. Busche, *Effcient loading of a magneto-optical trap for experiments with dense ultracold Rydberg gases*, Diploma thesis, Heidelberg University (2011).

[165] W. Petrich, M. H. Anderson, J. R. Ensher, and E. A. Cornell, *Behavior of atoms in a compressed magneto-optical trap*, J. Opt. Soc. Am. B **11**, 1332 (1994).

[166] C. G. Townsend, N. H. Edwards, K. P. Zetie, C. J. Cooper, J. Rink, and C. J. Foot, *High-density trapping of cesium atoms in a dark magneto-optical trap*, Phys. Rev. A **53**, 1702 (1996).

[167] D. A. Steck, *Rubidium 87 D Line Data*, available online at http://steck.us/alkalidata (revision 2.2.1, 21 November 2019).

[168] R. Grimm, M. Weidemüller, and Y. B. Ovchinnikov, *Optical Dipole Traps for Neutral Atoms*, in *Adv. At. Mol. Opt. Phys.*, Vol. 42, edited by B. Bederson and H. Walther (Academic Press, 2000) pp. 95–170.

[169] C. S. Adams, H. J. Lee, N. Davidson, M. Kasevich, and S. Chu, *Evaporative Cooling in a Crossed Dipole Trap*, Phys. Rev. Lett. **74**, 3577 (1995).

[170] M. D. Barrett, J. A. Sauer, and M. S. Chapman, *All-Optical Formation of an Atomic Bose-Einstein Condensate*, Phys. Rev. Lett. **87**, 010404 (2001).

[171] S. Geier, *Engineering Rydberg-spin Hamiltonian using microwave pulse sequences*, Master's thesis, Heidelberg University (2019).

[172] J. R. Rubbmark, M. M. Kash, M. G. Littman, and D. Kleppner, *Dynamical effects at avoided level crossings: A study of the Landau-Zener effect using Rydberg atoms*, Phys. Rev. A **23**, 3107 (1981).

[173] S. Helmrich, *Improving optical resolution by noise correlation analysis*, Master's thesis, Heidelberg University (2013).

[174] A. Müller, *State Selective Field Ionization in an Apparatus for Large Optical Access*, Master's thesis, Heidelberg University (2019).

[175] E. D. Black, *An introduction to Pound–Drever–Hall laser frequency stabilization*, Am. J. Phys. **69**, 79 (2001).

[176] T. Kerst, *Laser Frequency Stabilization on a High-Finesse Fabry-Pérot Cavity*, Master's thesis, Heidelberg University (2014).

[177] M. Robert-de Saint-Vincent, C. S. Hofmann, H. Schempp, G. Günter, S. Whitlock, and M. Weidemüller, *Spontaneous Avalanche Ionization of a Strongly Blockaded Rydberg Gas*, Phys. Rev. Lett. **110**, 045004 (2013).

[178] M. Ferreira-Cao, V. Gavryusev, T. Franz, R. F. Alves, A. Signoles, G. Zürn, and M. Weidemüller, *Depletion imaging of Rydberg atoms in cold atomic gases*, J. Phys. B **53**, 084004 (2020).

[179] S. Geier, N. Thaicharoen, C. Hainaut, T. Franz, A. Salzinger, A. Tebben, D. Grimshandl, G. Zürn, and M. Weidemüller, *Floquet Hamiltonian Engineering of an Isolated Many-Body Spin System* (2021), arXiv:2105.01597 [cond-mat.quant-gas] .

[180] J. Han, T. Vogt, M. Manjappa, R. Guo, M. Kiffner, and W. Li, *Lensing effect of electromagnetically induced transparency involving a Rydberg state*, Phys. Rev. A **92**, 063824 (2015).

[181] H. Schempp, G. Günter, S. Wüster, M. Weidemüller, and S. Whitlock, *Correlated Exciton Transport in Rydberg-Dressed-Atom Spin Chains*, Phys. Rev. Lett. **115**, 093002 (2015).

[182] S. Whitlock, H. Wildhagen, H. Weimer, and M. Weidemüller, *Diffusive to Nonergodic Dipolar Transport in a Dissipative Atomic Medium*, Phys. Rev. Lett. **123**, 213606 (2019).

[183] C. Gardiner and P. Zoller, *Quantum noise: A Handbook of Markovian and Non-Markovian Quantum Stochastic Methods with Applications to Quantum Optics*, 3rd ed. (Springer-Verlag Berlin Heidelberg, 2004).

[184] G. Labeyrie, E. Vaujour, C. A. Müller, D. Delande, C. Miniatura, D. Wilkowski, and R. Kaiser, *Slow Diffusion of Light in a Cold Atomic Cloud*, Phys. Rev. Lett. **91**, 223904 (2003).

[185] G. Labeyrie, R. Kaiser, and D. Delande, *Radiation trapping in a cold atomic gas*, Appl. Phys. B **81**, 1001 (2005).

[186] J. Gallas, G. Leuchs, H. Walther, and H. Figger, *Rydberg Atoms: High-Resolution Spectroscopy and Radiation Interaction—Rydberg Molecules*, in *Adv. At. Mol. Opt. Phys.*, Vol. 20, edited by D. Bates and B. Bederson (Academic Press, 1985) pp. 413–466.

[187] K. Singer, M. Reetz-Lamour, T. Amthor, S. Fölling, M. Tscherneck, and M. Weidemüller, *Spectroscopy of an ultracold Rydberg gas and signatures of Rydberg–Rydberg interactions*, J. Phys. B **38**, S321 (2005).

[188] C.-A. Brandl, *Influence of Laser Noise on the spectra of Electromagnetically Induced Transparency in Rydberg Gases*, Master's thesis, Heidelberg University (2020).

[189] A. Browaeys, D. Barredo, and T. Lahaye, *Experimental investigations of dipole–dipole interactions between a few Rydberg atoms*, J. Phys. B **49**, 152001 (2016).

[190] J. R. Kuklinski, U. Gaubatz, F. T. Hioe, and K. Bergmann, *Adiabatic population transfer in a three-level system driven by delayed laser pulses*, Phys. Rev. A **40**, 6741(R) (1989).

[191] U. Gaubatz, P. Rudecki, S. Schiemann, and K. Bergmann, *Population transfer between molecular vibrational levels by stimulated Raman scattering with partially overlapping laser fields. A new concept and experimental results*, J. Chem. Phys. **92**, 5363 (1990).

[192] K. Bergmann, H. Theuer, and B. W. Shore, *Coherent population transfer among quantum states of atoms and molecules*, Rev. Mod. Phys. **70**, 1003 (1998).

[193] K. Mølmer, Y. Castin, and J. Dalibard, *Monte Carlo wave-function method in quantum optics*, J. Opt. Soc. Am. B **10**, 524 (1993).

[194] I. Mirgorodskiy, *Storage and propagation of Rydberg polaritons in a cold atomic medium*, Ph.D. thesis, University of Stuttgart (2017).

[195] T. F. Gallagher, L. M. Humphrey, R. M. Hill, and S. A. Edelstein, *Resolution of $|m_l|$ and $|m_j|$ Levels in the Electric Field Ionization of Highly Excited d States of Na*, Phys. Rev. Lett. **37**, 1465 (1976).

[196] J. Sheng, Y. Chao, S. Kumar, H. Fan, J. Sedlacek, and J. P. Shaffer, *Intracavity Rydberg-atom electromagnetically induced transparency using a high-finesse optical cavity*, Phys. Rev. A **96**, 033813 (2017).

[197] B. Kim, K.-T. Chen, S.-S. Hsiao, S.-Y. Wang, K.-B. Li, J. Ruseckas, G. Juzeliūnas, T. Kirova, M. Auzinsh, Y.-C. Chen, Y.-F. Chen, and I. A. Yu, *A weakly-interacting many-body system of Rydberg polaritons based on electromagnetically induced transparency*, Commun. Phys. **4**, 101 (2021).

[198] J. B. Balewski, A. T. Krupp, A. Gaj, S. Hofferberth, R. Löw, and T. Pfau, *Rydberg dressing: understanding of collective many-body effects and implications for experiments*, New J. Phys. **16**, 063012 (2014).

[199] Y.-Y. Jau, A. Hankin, T. Keating, I. Deutsch, and G. Biedermann, *Entangling atomic spins with a Rydberg-dressed spin-flip blockade*, Nat. Phys. **12**, 71 (2016).

[200] A. Arias, G. Lochead, T. M. Wintermantel, S. Helmrich, and S. Whitlock, *Realization of a Rydberg-Dressed Ramsey Interferometer and Electrometer*, Phys. Rev. Lett. **122**, 053601 (2019).

[201] T. Peters, Y.-H. Chen, J.-S. Wang, Y.-W. Lin, and I. A. Yu, *Observation of phase variation within stationary light pulses inside a cold atomic medium*, Opt. Lett. **35**, 151 (2010).

[202] G. T. Campbell, Y.-W. Cho, J. Su, J. Everett, N. Robins, P. K. Lam, and B. Buchler, *Direct imaging of slow, stored and stationary EIT polaritons*, Quantum Sci. Technol. **2**, 034010 (2017).

[203] J. L. Everett, G. T. Campbell, Y.-W. Cho, P. Vernaz-Gris, D. B. Higginbottom, O. Pinel, N. P. Robins, P. K. Lam, and B. C. Buchler, *Dynamical observations of self-stabilizing stationary light*, Nat. Phys. **13**, 68 (2017).

[204] J. Klaers, J. Schmitt, F. Vewinger, and M. Weitz, *Bose–Einstein condensation of photons in an optical microcavity*, Nature **468**, 545 (2010).

[205] R. Weill, A. Bekker, B. Levit, and B. Fischer, *Bose–Einstein condensation of photons in an erbium–ytterbium co-doped fiber cavity*, Nat. Commun. **10**, 747 (2019).

[206] Oxford Instruments plc, *iXon EMCCD Cameras*, available at http://www.andor.com/cameras/ixon-emccd-camera-series (accessed: 02 April 2021).

[207] L. Li, M. Li, Z. Zhang, and Z.-L. Huang, *Assessing low-light cameras with photon transfer curve method*, J. Innov. Opt. Health Sci. **09**, 1630008 (2016).

[208] V. Gavryusev, *Imaging of Rydberg Impurities in an Ultracold Atomic Gas*, Ph.D. thesis, Heidelberg University (2016).

[209] M. Newberry, *Tech Note: Pixel Response Effects on CCD Camera Gain Calibration*, available at https://www.mirametrics.com/tech_note_ccdgain.php (2020, accessed: 14 April 2021).

[210] M. Dehabe, *Creating an optical microtrap with tunable aspect ratio for ultracold Fermions*, Master's thesis, Heidelberg University (2016).

[211] D. Lu and W. Hu, *Physical picture, pattern-control, and detection approach for tightly focused beams: In the view of Fourier optics* (2010), arXiv:1003.2099 [physics.optics] .

[212] G. Strang, *On the Construction and Comparison of Difference Schemes*, SIAM J. Numer. Anal. **5**, 506 (1968).

[213] D. Mas, J. Garcia, C. Ferreira, L. M. Bernardo, and F. Marinho, *Fast algorithms for free-space diffraction patterns calculation*, Opt. Commun. **164**, 233 (1999).

[214] W. Zhang, H. Zhang, and G. Jin, *Adaptive-sampling angular spectrum method with full utilization of space-bandwidth product*, Opt. Lett. **45**, 4416 (2020).

[215] L. Novotny, *Lecture Notes on ELECTROMAGNETIC FIELDS AND WAVES*, available at https://www.photonics.ethz.ch/fileadmin/user_upload/Courses/EM_FieldsAndWaves/ (2013, accessed: 02 April 2021).

[216] D. P. Sadler, E. M. Bridge, D. Boddy, A. D. Bounds, N. C. Keegan, G. Lochead, M. P. A. Jones, and B. Olmos, *Radiation trapping in a dense cold Rydberg gas*, Phys. Rev. A **95**, 013839 (2017).

[217] C. S. Hofmann, G. Günter, H. Schempp, M. Robert-de Saint-Vincent, M. Gärttner, J. Evers, S. Whitlock, and M. Weidemüller, *Sub-Poissonian Statistics of Rydberg-Interacting Dark-State Polaritons*, Phys. Rev. Lett. **110**, 203601 (2013).

# Acknowledgments

*"Es sind die Begegnungen mit Menschen,*
*die das Leben lebenswert machen."*
— Guy de Maupassant

An dieser Stelle möchte ich mich bei all jenen bedanken, welche die Entstehung dieser Arbeit ermöglicht haben. Insbesondere gilt mein Dank

... Matthias Weidemüller, meinem Betreuer und Mentor in einer sehr spannenden Zeit meiner fachlichen und persönlichen Entwicklung. Vielen Dank, dass ich in den letzten Jahren EIT mit Rydbergatomen eingehend erforschen durfte. Insbesondere bin ich dir dankbar für die vielen Anregungen und Diskussionen, die diese Arbeit vorangebracht haben, sowie für ein sehr angenehme, gleichsam fordernde und unterstützende Arbeitsatmosphäre. Auch für den Auslandsaufenthalt, den du mir ermöglicht hast, danke ich dir sehr. Insgesamt war die Zeit in deiner Arbeitsgruppe und die Zusammenarbeit mit dir für mich fachlich und persönlich äußerst bereichernd!

... Jörg Evers für die Übernahme des Zweitgutachtens dieser Arbeit, sowie den Mitgliedern meines Prüfungskommitees Tilman Enss und Selim Jochim.

... the Rydberg team, for the great time we have spent together! Here, my deepest gratitude goes towards Clément Hainaut, Nithiwadee Thaicharoen and Gerhard Zürn for all your advice, and for sharing your in-depth understanding and intuition of physics with me. Moreover, I would like to express my cordial thanks to my fellow doctoral students Renato Ferracini Alves, Titus Franz, Sebastian Geier and Andre Salzinger. I have very much enjoyed working with you! Thanks for running the lab together, for exploring the world of Rydberg physics, and for enjoying life with and without physics. Moreover, I would like to thank the Bachelor and Master students Sebastian Bok, Carlos Brandl, Eduard Braun, Mathurin Choblet, Theresa Gier, David Grimshandl, Lorenz Luger, Charles Möhl, Maximilian Müllenbach, Alexander Müller, Philipp Schultzen, Julia Siegl, Karen Wadenpfuhl and Henrik Zahn for completing the Rydberg team, and for all their valuable contribution to what we have achieved in the last years. It has been a great pleasure to be part of the Rydberg team!

... Thomas Pohl, Martin Gärttner, Valentin Walther and Yong-Chang Zhang for collaborating with us on the topics of this thesis. I have learned a lot from our joint work and from our many insightful discussions, which shaped this work considerably.

... Vladan Vuletić, Sergio Cantu, Valentin Klüsener, Aditya Venkatramani and Wenchao Xu, as well as the RLE and CUA members for their great hospitality, a memorable stay abroad and for all the in-depth discussions about physics. Furthermore, I would like to thank Michael Fleischhauer, Shannon Whitlock, Johannes Otterbach and David Petrosyan for various insightful discussions about stationary light polaritons and different models of Rydberg EIT. Many thanks also go to Antoine Browaeys, Daniel Barredo, Guillaume Bornet, Loïc Henriet, Thierry Lahaye, Pascal Scholl, Adrien Signoles, Florian Wallner and Hannah Williams for collaborating with us on the topic of Hamiltonian engineering. Furthermore, I would like to thank the GiRyd community for a vivid exchange of knowledge on Rydberg physics and for the familiar atmosphere during all encounters.

... all members of the QD and Ultracold groups for sharing ideas and experimental techniques, and for the great atmosphere in the institute.

... Claudia Krämer für all die administrative Unterstützung, ohne welche wir uns längst nicht so gut auf die Forschung konzentrieren könnten. Auch den Mitgliedern der EDV-Abteilung sowie der Elektronikwerkstatt und der Mechanischen Werkstatt gilt mein Dank für ihre kompetente und unkomplizierte Hilfe bei allen anfallenden technischen Herausforderungen.

... dem DFG Schwerpunktprogramm GiRyd, dem Exzellenzcluster STRUCTURES, dem Heidelberg CQD, der HGSFP, der IMPRS-QD und dem SFB ISOQuant für die fachliche, finanzielle und ideelle Förderung während meiner Promotion. Insbesondere bin ich sehr dankbar dafür, dass ich an einem GiRyd International PhD Exchange teilnehmen durfte.

... Titus Franz, Martin Gärttner, Clément Hainaut, Matthias Zimmermann und Gerhard Zürn für das Korrekturlesen dieser Arbeit.

... der Deutschen Physikalischen Gesellschaft, für die unzählige Begegnungen mit so vielen interessanten und wunderbaren Menschen, die sie ermöglicht.

... meinen Freunden für ein Studium und eine Promotion in Heidelberg, die mir immer in Erinnerung bleiben werden.

Zu guter Letzt möchte ich mich bei den Menschen bedanken, die mich immer unterstützt haben und mein Leben auf eine ganz besondere Art und Weise lebenswert machen:

... MEINER FAMILIE. Danke, dass ihr mich auf meinem Weg begleitet und immer an meine Fähigkeiten glaubt.

...MATTHIAS ZIMMERMANN. Ich danke dir für deine Liebe, für all deine Unterstützung und für unsere wunderbare gemeinsame Zeit.